Toward Reconciliation of Quantum Fields and Relativity through Space Time Occupancy

Discrete closure and curved geometry in a common quantum and gravitational construction

Christopher Schiele

Alex Malyuta

Paul Schiele

Reconciled review draft • 26 October 2026 • Geometric clocks and executed circuit reconciliation

Abstract

Space Time Occupancy (STO) adopts geometric discrete time, continuous space, ubiquitous curvature and closed global energy conservation. Temporal bandwidth determines which spatial distinctions are resolved. We develop a common quantum and gravitational construction through ATCS, TTDL, TASL, curvonic reference maps and AxiomARC. The thermal Anglar fixes inverse temperature; explicit reference carriers preserve covariance under changes of units. The LT rotation-period quantity yields the HTF velocity 348.3165719654 in the declared chart. Equal allocation of binary information over three spatial degrees derives $\ln 2 / 3$ and a 66.5844417251 K gap coordinate without water, gravity or pressure inputs. Fresh execution of the supplied Bloch, AME and metaplectic paths verifies finite quantum control, replay and tensor properties. A continuous-space embedding, autonomous energy-conservation theorem and constrained occupancy action supply explicit proposed completions. A selected horizon capacity state and weighted entropy response support a conditional semiclassical Einstein-equation closure. Fixed galaxy and nuclear comparisons and source-grouped CERN replay are retained with their observable definitions; historical energy-labelled CERN results are reclassified as pseudorapidity diagnostics. Prospective NMR, resonator and material-response protocols provide discriminating tests. The result is a connected mathematical and computational framework. Section 10 consolidates the physical identifications and empirical validations needed for a validated EFE–QFT reconciliation.

Keywords: Space Time Occupancy; ATCS; TTDL; TASL; curved spacetime; AxiomARC; quantum dynamics.

1 The reconciliation problem and the proposed route

The STO proposal begins with a change in explanatory order. Instead of assuming a fixed spacetime container and subsequently placing information and matter inside it, it treats distinguishability, admissible transitions, and rotational closure as primitives. Physical length, duration, and thermal coordinates are realized through comparisons between these structures. The intended reconciliation is therefore a common construction of quantum and gravitational descriptions from an operational substrate, rather than a direct quantization of an already completed classical metric theory. This is the throughline of the dimensional-emergence working proof and the supplied reconciliation outline [S296, S297].

The new observational prologue emphasizes the origin of these constructions in thought experiments [N15]. Repeated cycle closure motivates the clock; a common pendulum and fall interval motivates a comparison of spatial spans; a thermal control motivates the distinction between a coordinate map and the

constitutive response of a reservoir. These observations are useful prototypes when each is translated into a defined observable, operator and test. Unit choices affect numerical coordinates, while the operational claim must survive a change of those choices. This is the role of the reference carriers in Appendix A. Appendix J records the translation of the additional thought experiments without making an analogy carry a proof of dynamics.

There is already a consistent theory of quantum fields on prescribed curved, globally hyperbolic backgrounds [R1]. Quantum field theory (QFT) does not require a fundamentally flat spacetime, nor is a discrete substrate part of its general definition. General relativity (GR) also does not require global flatness. A smooth Lorentzian metric has locally inertial tangent frames even when its curvature is nonzero. Consequently, dispensing with a preferred flat background is a useful starting choice, but cannot by itself complete reconciliation.

The harder questions concern the joint dynamics of geometry and quantum matter, the definition of physical observables and time, the ultraviolet behavior of gravity, the origin and normalization of horizon entropy, and the emergence of familiar particle dynamics. Low-energy quantum gravity can be treated as an effective field theory [R2]; the unresolved objective is a more complete microscopic account and its independently testable consequences. STO need not inherit every assumption of conventional quantization, but must specify which observable problems its alternative construction resolves.

We organize the argument in six steps. First, define the operational state and its geometric capacity without assigning SI units. Second, show how ATCS and TTDL produce exact relationships among span, boundary, and content. Third, introduce physical reference quantities through TASL and a dimensionally explicit curvonic ledger, and identify the thermal Anglar with the entropy slope in bits per energy. Fourth, construct finite quantum states and dynamics using the existing AxiomARC maps, with explicit thermal weights and phase-sector representations. Fifth, connect a horizon entropy response and thermal coordinate to the Einstein equation. Sixth, ask whether a refinement of the finite model produces a covariant field theory with the same stress tensor. The last two steps are a coupled construction: a quantum model must supply the thermodynamic inputs, and the gravitational equation must describe the geometry on which its low-energy observables propagate.

Reconciliation challenge	STO contribution	Construction location
No preferred background	Continuous curved spatial carrier and operational addresses	Sections 2 and 7; Appendix M1
Quantum evolution and thermal response	Executed unitary circuits and exact TASL–beta conversion	Sections 4–5 and 7.1
Gravity as a thermodynamic response	Selected horizon capacity and weighted response	Section 6; Appendix B
Field and gauge construction	Occupancy action, constrained fields and common generator	Section 7; Appendices D3 and M3
Mass and inertia	Curvonic and m-point reference maps	Section 8; Appendix G
Boundary state and recovery	MPS and AME realization with explicit readout	Section 5; Appendix C3
Observational comparison	Source-bound CERN, galaxy and transient audits	Section 9; Appendix E

Throughout, an **adopted premise** defines the model, an **exact consequence** follows mathematically from stated definitions, a **proposed completion** adds a construction for author confirmation, and an **open obligation** names an input or limit not established in the reviewed material. This distinction permits a serious development of STO on its own terms while keeping the manuscript's claims reproducible.

2 Operational premises and conventions

We adopt the following premises as the version of STO examined here [S028, S054, S292–S296, S302]. Mathematical consequences are developed within these premises; external comparisons specify a common observable rather than silently replacing the premises.

P0 — Geometric discrete time and continuous curved space. Time is realized through discrete closure and recurrence; space is continuous. Finite temporal bandwidth determines which distinctions in that continuous spatial carrier are operationally resolved. Spacetime curvature is ubiquitous, rather than a perturbation of an assumed globally flat physical substrate. The observer participates physically in the curvature and measurement account. A smooth metric is an effective description; local tangent coordinates do not remove global curvature. Finite address or circuit dimension describes a resolved sector and does not assert that physical space consists of finitely many points. Appendix M1 supplies an explicit continuous-carrier realization [N30].

P1 — Operational distinguishability. A resolved state is described by a sufficient set of position, phase, and closure labels. Forgetting a label can identify states that the full description distinguishes. The number of labels is an operational description length; a physical manifold dimension requires an additional geometry and local rank construction.

P2 — Admissible evolution. Transitions must satisfy the declared routing and boundary rules. A shortest admissible path can differ from a shortest path in an ambient metric. We retain both distances and their domains. A difference between them is a candidate source of persistence or delay, not automatically a spacetime curvature scalar [S041].

P3 — ATCS capacity. For a dimensionless edge or closure count $n>0$, define

$$C(n)=\frac{2}{3}n^2.$$

P4 — TTDL comparison and geometric clocks. A regular tetrahedron supplies vertical count $h(n)=n\sqrt{2/3}$ and horizontal count n, giving $\tau_h/\tau_v=\sqrt{3/2}$. The established clock charts use the m-point duration and the scale factors $1/\pi, 1/\pi^2, 1, \sqrt{2}, 2, 4$. Appendix A5 gives their typed maps. TTDL is this specified geometric comparison; its fixed ratio does not replace the velocity-dependent Lorentz factor.

P5 — TASL. The thermal Anglar invariant and temperature map are

$$\theta_k=\frac{c^2h}{k_B\ln 2}, T(\Theta)=\frac{\theta_k}{\Theta}.$$

Here h in the invariant is Planck's constant; the distinct symbol $h(n)$ denotes tetrahedral height count only. We use Θ for a physical Anglar, with dimensions L^2T^{-1}, and θ_k has dimensions $L^2T^{-1}K$. Temperature is written T, elapsed duration t, and dimensional time T. Thermodynamic inverse temperature is $\beta_T=1/(k_BT)$, distinct from the spinor amplitude β and the galaxy interpolation exponent.

The dimensionless theta-sector phase is χ; it is neither the Anglar Θ nor the null expansion ϑ. Hydraulic head is denoted h_v or H_{head}, preserving h for Planck's constant.

P6 — Imported physical priors. The constants c, h, k_B, N_A and $R = N_A k_B$ are imported. The two-way light speed defines the causal length–time conversion in a locally inertial vacuum frame. This stages the reference system without claiming to derive those constants. The Born rule, complex Hilbert space, and Hermitian quantum generators are also retained in the implemented quantum branch.

P7 — Closed global energy conservation. Total energy is conserved in the closed STO account, including the observer, controller, curvature and participating reservoirs. Subsystems may exchange energy. This is an adopted physical premise, not a deduction from a choice of SI units or from the existence of a local divergence identity. Appendix M2 supplies a discrete realization with an autonomous total generator and an explicit controller-inclusive balance. The helical charge $Q_\Omega = E - \Omega J$ is the appropriate symmetry charge on a helical branch [S021]; it is distinguished from the global STO energy. The continuum realization of the global account is recorded in Section 10.

For the gravitational construction we use metric signature $(-,+,+,+)$. Curvature is defined so that a hypersurface-orthogonal null congruence satisfies $d\vartheta/d\lambda = -\vartheta^2/2 - \sigma_{ab}\sigma^{ab} - R_{ab}k^a k^b$. The expansion ϑ is not an Anglar. Entropy S has units J/K, whereas $s = S/k_B$ is dimensionless and $S_{bits} = S/(k_B \ln 2)$ is measured in bits. The source symbol S_{STO} for a frequency multiplier is retained only for that ledger factor; it is not identified with thermodynamic entropy.

2.1 Proposed macroscopic metrology boundary

P8 — Reference-frame resolution proposal. The new addition assigns an Earth-reference ledger a characteristic resolution $\Delta L_* = 0.1$ mm [N15]. We adopt it here as a proposed coarse-graining scale for the specified macroscopic comparison, with its physical domain to be established. It is not assumed to forbid submillimeter measurements, fix a universal ultraviolet cutoff, or identify the microscopic horizon tile area a_* in Section 6.

Write thermal diffusivity as D_T to distinguish it from the fine-structure constant and the resonator response coefficient. For the declared diffusive-scale convention,

$$\ell_D = \sqrt{D_T t}, \chi_D = \frac{\ell_D}{\Delta L_*}, t_* = \frac{\Delta L_*^2}{D_T} = \frac{10^{-8} m^2}{D_T}.$$

Here t is an independently calibrated interaction duration. A root-mean-square displacement convention would include its dimension-dependent factor; that convention must remain fixed when comparing a measured length. The proposed STO regime boundary is $\chi_D = 1$: below it the addition uses a material description, and above it proposes an active frame response. This is a constitutive hypothesis, not a consequence of the common dimensions $[D_T] = [\Theta] = L^2 T^{-1}$. The quoted frame Anglar 3.435 requires a physical carrier and a response equation before it can replace a measured diffusivity.

A U.S.-gallon reference has $V = 3.785411784 \times 10^{-3}\ m^3$ and cube edge 0.155849128 m. It is retained as a volume calibration. The equation for ℓ_D contains no volume and does not uniquely select that gallon. A heat-capacity construction additionally requires density, specific heat, temperature change, geometry, boundary conditions and a duration; for a nearly uniform calorimetric step one may use $Q = \rho c_p V \Delta T$ in

its regime. Connecting that Q to the curvonic count requires the energy carrier already specified in Section 4. Appendix J separates the proposed boundary from the uncompleted uniqueness assertion.

2.2 Time manifold closure premises

The Time Manifold chapter [N27] makes explicit the proposed physical restriction behind the finite implementation: admissible histories must be jointly representable in the K9 route structure, the decorated 24-cell and a selected E8 representation, with a two-period spine, finite channel allocation and restricted geometric readout. We adopt these as additional closure premises for the branch developed in Appendix L. The global assertion that these structures exhaust all physical degrees of freedom is a stronger premise than the implemented finite model; it is not inferred from the number 248 alone. The constructions below specify how to test the restricted branch while preserving the existing G2 and PC10 results.

The chapter realizes duration through ordered closure events and curvature redistribution. The update index j, clock reading t_j, thermal interval τ_E and geometric-flow parameter have different domains. Appendix A5 fixes the operational chart maps; Appendix M connects the discrete update to continuous spatial functions and a closed energy account. This implements the stated explanatory order without requiring a globally flat background.

3 Exact geometric consequences

3.1 Capacity and volumetric lift

Proposition 1. In a regular tetrahedron with dimensionless edge count n, ATCS capacity is its squared height count. Its dimensionless volume is a fixed multiple of the capacity to the power $3/2$:

$$h(n)^2 = C(n), V_{count}(n) = \frac{n^3}{6\sqrt{2}} = \frac{\sqrt{3}}{8} C(n)^{3/2}.$$

Proof. The distance from a triangular face's center to a vertex is $n/\sqrt{3}$. Applying the Pythagorean relation to the remaining edge gives $h^2 = n^2 - n^2/3$. Substitution in the usual tetrahedral volume gives the second identity. Physical edge length $\ell_* n$ yields physical volume $\ell_*^3 V_{count}$. The coefficient is fixed by geometry; ℓ_* is a physical reference, not fixed by the exponent. ▫

Thus $C(24) = 384$ and $C(360) = 86400$ are exact geometric counts. Identifying the second number with seconds in a day is a subsequent clock calibration. The relation

$$\frac{h(12)}{h(48)} (2\pi)^2 = \pi^2$$

is also exact, but follows for any pair of similar tetrahedra with edge ratio $1:4$. Selection of the $12k$ gates is a separate STO admissibility premise; the numerical cancellation alone does not establish its physical necessity.

The boundary of a cube with eight subdivisions per edge contains $6 \cdot 8^2 = 384$ square cells. Radial projection of that boundary to a sphere preserves its topology and the number of cells. It does not preserve each cell's area. This supplies a concrete interpretation of a common 384-label boundary, while leaving the metric Jacobian explicit. Equating the count with thermodynamic entropy requires a state distribution or entropy functional.

For a regular d-simplex with edge ℓ, the height is $H_d = \ell\sqrt{(d+1)/(2d)}$. At a common edge scale, the ratio of squared heights in dimensions d and $d-1$ is $1 - 1/d^2$. These are legitimate cross-dimensional comparison operators. Equal numerical values of a perimeter, an area, and a volume are not invariant statements until the reference length used to normalize each measure is declared.

3.2 Closure and the role of pi

The source interpretation of π as the diameter-span count in one unrolled circle is mathematically useful: $C_{circle}/d = \pi$. It is a count per turn. A temporal frequency additionally requires a duration per turn. If a circle is traversed in t_{turn}, the diameter-span rate is π / t_{turn}. Neither quantity requires a meter or a second until a physical realization is chosen.

This gives a practical unit-agnostic implementation rule: represent a quantity by a dimensionless ratio to an explicit reference, transport the ratio through geometric maps, and restore units at the measurement interface. The identity is preserved when the quantity and its reference change units together. It is not preserved if a dimensionful numerical value changes units while the normalizer remains a bare, fixed number.

The hydraulic-head correspondence makes the shared-clock construction more explicit [S039, N7]. For steady, incompressible, inviscid flow along a streamline with no added work or loss, Bernoulli head is

$$H_{head} = \frac{p}{\rho g} + \frac{v^2}{2g} + z.$$

The specific weight is $\gamma = \rho g$; pressure head is p/γ. The velocity head $h_v = v^2/(2g)$ is a length, not Planck's constant [R28]. In a uniform field, a fall from rest through distance d has $v^2 = 2gd$, so $h_v = d$ and $v^2/(2gd) = 1$. A two-to-one energy distinction follows directly: the fall changes specific kinetic energy by $v^2/2 = gd$.

Let ℓ be the small-amplitude pendulum length and t the common pendulum period and fall duration. Then

$$t = 2\pi\sqrt{\ell/g} = \sqrt{2d/g}, \frac{d}{\ell} = 2\pi^2, L = gt^2 = 2d.$$

Here L denotes the full comparison span, not the pendulum length. Choosing $t = 2t_*$ yields five dimensionless recoveries:

$$\frac{L}{d} = 2, \frac{L}{gt_*^2} = 4, \frac{gt_*^2}{\ell} = \pi^2, \frac{d}{\ell} = 2\pi^2, \frac{L}{\ell} = 4\pi^2.$$

These are exact consequences of the stated measurement model. They reproduce the numerical closure in `tools_sto_quick.py` without treating g/ℓ or L/g as dimensionless before the clock carrier is restored. In the full-span mechanical chart, define $\epsilon_{curv} = gL = v^2$. The one-way fall supplies $gd = \epsilon_{curv}/2$. A physical cycle must specify its work and return path before these two legs are added as transferred energy. Appendix H2 gives the numerical construction.

The ratios establish a unit-neutral reference correspondence. They do not independently fix a dimensional g or spatial topology. Finite-amplitude and nonuniform-field corrections modify the measurement

operators. The geometric use of $2\pi^2$ as a three-sphere coefficient remains a separate correspondence requiring the source's curvature map.

3.3 Address geometry and quantum amplitudes

Three slots drawn from four symbols have exactly 64 words. Classifying by the number of distinct symbols gives

$$|H_1| = 4, |H_2| = \binom{4}{2}(2^3 - 2) = 36, |H_3| = 4 \cdot 3! = 24.$$

The 36 contexts correspond to six unordered pairs with six nonconstant slot patterns each. They are not 36 different edges of a tetrahedron. The 24 contexts specify a missing symbol and an ordering of the other three [S301, S302].

Proposition 2. The four normalized states

$$|t_0\rangle = |0\rangle, |t_j\rangle = \frac{|0\rangle}{\sqrt{3}} + \sqrt{\frac{2}{3}} e^{2\pi i(j-1)/3} |1\rangle, j = 1, 2, 3,$$

form a regular tetrahedron on the Bloch sphere. For distinct i, j, their squared overlap is $1/3$, and their Bloch vectors have inner product $-1/3$. The operators $\Pi_j = |t_j\rangle\langle t_j|/2$ sum to the identity.

Proof. Normalization is immediate. Overlap with t_0 has squared modulus $1/3$. For the remaining pairs, use $\cos(2\pi/3) = -1/2$. The Bloch overlap formula is $|\langle t_i \mid t_j\rangle|^2 = (1 + r_i \cdot r_j)/2$. The four Bloch vectors sum to zero, giving the resolution of identity. ▫

This is an exact point of contact between TTDL and quantum geometry: $\sqrt{2/3}$ is a preparation amplitude and $2/3$ its occupancy under the adopted Born rule. It realizes STO geometry inside quantum mechanics. It does not derive the Born rule or uniquely identify STO among all models capable of using this tetrahedral frame.

3.4 The source sectional curvature map

The sectional-curvature compendium supplies two maps that are retained as part of the STO construction [S054]. The first compares normalized three-sphere boundary capacity with curvature:

$$\frac{\Theta}{\Theta_{ref}} = \left(\frac{K_{ref}}{K}\right)^{3/2}, K = K_{ref}\left(\frac{\Theta_{ref}}{\Theta}\right)^{2/3}.$$

This is dimensionally well defined because both ratios are dimensionless. A physical sectional curvature has inverse-area units; the normalized curvature coordinate need not. The reference Anglar supplies the conversion from a spatial boundary measure to an areal recurrence rate.

The second map adopts a lifted full-turn holonomy on the pendulum–drop comparison cell. With cell area $d\ell = 2\pi^2\ell^2$ and assigned wrap 2π, its curvature coordinate is $K_{cell} = 1/(\pi\ell^2)$. Restoring elapsed period t in $\ell = gt^2/(4\pi^2)$ gives

$$K_{cell} = \frac{16\pi^3}{g^2 t^4}.$$

At $t=2t_*$, with $L_*=g_*t_*^2$, the normalized form is $K_{cell}L_*^2=\pi^3/\left(g/g_*\right)^2$. Thus the source's π^3/g^2 is preserved as a time-normalized relation, rather than read as an untyped SI equation. The chosen full-wrap lift is an STO cell premise. Its identification with measured Levi-Civita holonomy remains a physical correspondence question; the infinitesimal curvature-area formula alone does not select a finite full wrap.

These maps supply geometric structure and a dimensionless curvature loading. They do not by themselves select a unique acceleration response function. Appendix E2 traces the additional CRC acceleration prescription and the conditional response construction used in the galaxy comparison.

4 Thermal normalization and the energy references

4.1 A typed m-point construction

Let $T_*>0$ be a fixed thermal reference, chosen as 1 K in the current numerical chart. Let T_g be the selected gap-temperature coordinate. Define

$$\Theta_k=\frac{\theta_k}{T_*},\Theta_B=\frac{\theta_k}{T_g},\Theta=\sqrt{\Theta_k\Theta_B},k=\frac{\Theta_k}{\Theta},B=\frac{\Theta_B}{\Theta}.$$

Both factors under the square root now have the same dimensions. Consequently

$$k\,B=1,k=\sqrt{T_g/T_*},f=\frac{c^2}{\Theta},t_m=\frac{\Theta}{c^2},\lambda_m=\frac{\Theta}{c},m_m=\frac{h}{\Theta}.$$

Products such as $f\,t_m=1$ and $k\,B=1$ are exact reciprocal-coordinate identities. They do not imply that an arbitrary matrix assembled from the coordinates is unitary. A square matrix is unitary only if its columns are orthonormal in the relevant inner product; invertibility alone is insufficient.

Proposition 3. At the declared thermal reference, the m-point energy and the molar reference obey

$$E_m=m_mc^2=hf=k_BT_*k\ln 2,E_{mol}=RT_g\ln 2,$$

$$\frac{m_m}{E_{mol}/\left(N_Ac^2\right)}=B.$$

These identities follow by substitution and $R=N_Ak_B$. They explain the source's reciprocal mass ratios without assuming that a dimensionless ratio is an independently additive physical mass. Additivity belongs to consistently defined energies or masses; ratios add only when their denominators are the same. Binding and interaction energies must be included for a composite system.

For the angular-count operation use a physical reference $q_*=10800\,m^2s^{-1}$ in this chart and set $n_k=\sqrt{\Theta_k/q_*}$. The cancellation of the two factors of π in the source's angle-to-area-to-radius conversion is valid. The physical conversion is the declared q_*, not the dimensionless number π acquiring units. Appendix A gives the unit-covariant construction and the corrected rotation convention.

4.2 The catalyst and current direct CmB coordinate

The current catalyst uses the author-confirmed angular chart in Appendix A1. In that chart,

$$n_{\theta k}=\sqrt{\frac{\theta_k/T_*}{q_*}}=24.00393643510269\,,C_k=\frac{2}{3}n_{\theta k}^2=384.1259762536337\,.$$

The geometric capacity C_k is a dimensionless coefficient. Assigning $E_{mol}=C_k E_{mol,*}$ with the declared molar carrier $E_{mol,*}=1\,J/mol$ gives $T_g=E_{mol}/(R\ln 2)\simeq 66.652129725$ K. This construction uses the imported constants and chart assignments; water temperature, pressure and local gravity are not inputs. Their later use as comparison observables does not turn the raw catalyst into a water fit.

In numerical coordinates of this chart,

$$\overline{\Theta}_B=10800\,\frac{3}{2}\,\overline{R}\ln 2\,,n_{\theta B}=TTDL\sqrt{\overline{R}\ln 2}=2.940190382010316\,.$$

Here $\overline{R}$ is the gas constant divided by $1\,Jmol^{-1}K^{-1}$. This algebraic elimination proves the source's closure identity in the declared chart, while preserving physical typing under changes of units.

Let $\Theta_m=\sqrt{\Theta_k\Theta_B}$ and $n_m=\sqrt{\Theta_m/q_*}$. Distinguish the thermal coordinate $k=\Theta_k/\Theta_m$ from its square-root coordinate $k_n=n_{\theta k}/n_m=\sqrt{k}$. The current direct relation is

$$C_{mB}=\sqrt{\frac{k\,k_n}{\pi}}=2.72492984291961$$

for the raw catalyst. A different quoted value must identify its different catalyst or reference precision. A physical CMB temperature comparison also assigns a thermal carrier and specifies the spectrum-to-temperature observable. The previous build's C_k-1/C_{mB} subtraction is retained only as a historical profile; it is not part of the current direct construction and is no longer a theoretical obligation of this draft. Existing Bloch runs using that profile remain correctly labeled as such.

4.3 What the eight-method assessment contributes

The energy assessment in the working proof and `sto_energy_references.py` is more informative than a list of similar numbers. It identifies a network of reference transformations, distinguishes independent anchors from reconstructions, and exposes where a comparison still requires a mass, amount of substance, or length reference [S296]. The source has eight method numbers; method 4 contains both mechanical and water expressions.

Method	Native quantity or expression	Role in the reconciliation
1 TASL to ATCS	$(2/3)n_k^2$	Selects the proposed catalyst coefficient
2 Exact ATCS	$(2/3)24^2=384$	Supplies a geometric comparison anchor
3 Rotation	$2\pi O$ with explicit unit carriers	Defines the curvonic rotation chart and its inverse
4 Mechanical and water	gL in J/kg; $3RT/M$ in J/kg or J/g	Tests reference conversion and environmental calibration

Method	Native quantity or expression	Role in the reconciliation
5 Pressure and volume	PV in J	Requires an amount or mass before comparison to molar or specific energy
6 Photon scale	$N_A hc/\lambda$ in J/mol	Connects a declared length scale to a quantum energy
7 Information	$RT_g \ln 2$ in J/mol	Reconstructs the selected molar ledger
8 Earth-mass comparison	Supplied geometric coefficient	Needs an explicit SI mass map and independently fixed inputs

The common numerical neighborhood near 384 is a proposed reference-frame compatibility condition. It is not an equality between J, J/kg, and J/mol. For example, $3RT/M$ with $M = 18.01528$ g/mol returns J/g; expressing the same quantity in J/kg multiplies the number by 1000. Likewise, PV is not generally a system's total internal energy. A thermodynamic model must state which work or energy quantity is being compared.

The strongest use of this catalog is a withheld-anchor test: select one catalyst and freeze every reference conversion, then predict a different measured quantity without recalibrating it. Returning from $T_g = E_{mol}/(R\ln 2)$ to $RT_g \ln 2$ is a valid closure but supplies no independent evidence. The same applies to recovering N_A through $E_{mol}/(k_B T_g \ln 2) = R/k_B$ when $R = N_A k_B$ was already an input. This logical classification preserves the operational value of the eight methods while avoiding duplicated evidence.

4.4 The TASL Anglar as thermodynamic inverse temperature

The supplied thermodynamic-beta article points to an exact connection, beyond numerical proximity [N9, R21, R22]. At positive temperature and fixed other extensive coordinates, equilibrium thermodynamics gives the entropy slope

$$\beta_T = \frac{1}{k_B T}, \beta_{bit} = \frac{\partial\left[S/(k_B \ln 2)\right]}{\partial E} = \frac{\beta_T}{\ln 2}.$$

Substituting premise P5 gives the **thermal correspondence**

$$\beta_{bit} = \frac{\Theta(T)}{c^2 h}, \varepsilon_{bit} = k_B T \ln 2 = \frac{c^2 h}{\Theta(T)}.$$

Thus the TASL Anglar is the inverse-temperature coordinate expressed through the fixed carrier $c^2 h$. The natural bit is the base-two entropy convention; its energy scale is the reciprocal slope. This identifies an operational meaning for the TASL ladder within equilibrium statistical mechanics. It does not require a globally flat spacetime: the same relation applies to a local thermal state in its specified frame.

For a photon of frequency f, its energy-equivalent bit coordinate is

$$B_\gamma = \frac{hf}{k_B T \ln 2} = \frac{f\Theta(T)}{c^2}.$$

For the molar branch, $E_{mol}/T_g = R\ln 2 = 5.76314632164398\ J\,mol^{-1}K^{-1}$. Using the rounded source value of R gives 5.76314632167639. This is the molar entropy scale of one binary unit per entity. The

cancellation $E_{mol}/\left(k_B T_g \ln 2\right) = N_A$ is an exact bridge between the two carriers because $R = N_A k_B$ is imported. Together with Section 4.2, it gives the source's $n_{\theta B} = T\,T\,D\,L\sqrt{\overline{R}\ln 2}$ without introducing water, pressure or gravity as inputs.

The correspondence also supplies a concrete quantum thermal operator. For a specified self-adjoint Hamiltonian H with finite partition function,

$$\rho_T = \frac{e^{-\beta_T H}}{Z} = \frac{2^{-\Theta H/\left(c^2 h\right)}}{Z}, Z = Tr\, 2^{-\Theta H/\left(c^2 h\right)}.$$

This form carries the TASL coordinate directly into state probabilities. A constant energy shift changes Z and the numerator together, leaving ρ_T invariant. The entropy is $S/k_B = \beta_T \langle H \rangle + \ln Z$, so an energy-equivalent bit coordinate is not automatically the state's total entropy or accessible information. Actual heat and power require a process and its rate. Appendix H1 gives the byte conversion and a two-level check, while Section 5.2 applies the same relation to the Bloch channel.

4.5 HTF wavenumber and spectral transport

The updated HTF interpretation uses ordinary wavenumber $\tilde{\nu}_m = 1/\lambda_m$, with the raw m-point wavelength $\lambda_m \simeq 0.002542500068$ m [N22–N24]. This replaces the historical inch interpretation. Angular wavenumber $\kappa_m = 2\pi/\lambda_m$ remains distinct. The source construction derives its model propagation speed in Appendix K2; acoustic realization then uses the declared scale: $f_{ac} = v_s/\left(D\,\lambda_m\right)$ for a declared dimensionless ratio D. An octave assignment $f_j = 2^{m_j} f_{ac,j}$ then determines $\lambda_j = c/f_j$, $\Theta_j = c^2/f_j$ and $T_{E,j} = h f_j/\left(k_B \ln 2\right)$ consistently.

Appendix K reconstructs the six DRC spectral Anglar entries from the source note and octave assignments, with a maximum frequency discrepancy of approximately 0.102 cents relative to the printed Anglar values. This supplies the missing arithmetic throughline from the acoustic table to the controller's spectral coordinates. The octave assignments and acoustic scale remain declared inputs. This reconstruction establishes coordinate consistency, while physical acoustic-to-optical coupling requires the material response developed in K4–K6. Appendix A3 separately preserves the corrected gap-profile wavelength $\lambda_g = \lambda_k/T_g$; it is not the fundamental geometric-mean wavelength λ_m.

5 The finite quantum realization in AxiomARC

5.1 What is implemented

The reviewed modules implement an explicit map from DRC and hexagram addresses to normalized spinors, Bloch vectors, admissible boundary operations, and reproducible receipts. The 24-cell map, normalized in four dimensions, is passed through

$$\left(x_1, x_2, x_3, x_4\right) \mapsto \left(\alpha, \beta\right) = \left(x_1 + i\,x_2, x_3 + i\,x_4\right),$$

$$r = \left(2\,\mathrm{Re}\,\alpha^* \beta, 2\,\mathrm{Im}\,\alpha^* \beta, |\alpha|^2 - |\beta|^2\right).$$

The implemented incidence table has six Pauli fibers, each with four phase representatives. DRC values $1,2,4,8,7,5$ correspond respectively to $+X, +Y, +Z, -X, -Y, -Z$. The four representatives of a fiber differ by quarter-turn global phases and define the same density matrix. Address complementation,

which negates the four-vector in this map, therefore preserves the Bloch vector. This must not be confused with reversing the Bloch pole.

The H1 preparation addresses define the tetrahedral frame of Proposition 2. In the current convention, only `000000` is at $+Z$; `101010`, `010101`, and `111111` have $Z=-1/3$. In particular, the tetrahedral H1 vertices are not the six Pauli poles and are not pairwise orthogonal. Their equal pairwise fidelities are $1/3$.

The controller uses address, chirality, boundary, and phase information to select a traceless Hermitian generator. A representative implementation is

$$G=\frac{1}{2}\left(P\,v_{route}+\log q\right)\cdot\sigma\,,\;U(\varphi)=e^{-i\varphi G},$$

where q contains positive dimensionless m-point ratios, the logarithm is componentwise, and P is the declared axis action. This is a finite control law. A physical Hamiltonian requires an energy multiplier and a clock relation, for example $H=(\hbar/t_*)G$ and $\varphi=t/t_*$. The source's logarithmic generator is an implemented modeling choice, not a consequence of reciprocal unit identities alone.

Changing a fiber label while also changing the selected gate can change the final state. Changing only a global phase cannot. Consequently, the operational meaning of fiber-sensitive outputs is that the full control record distinguishes preparations or transformations. Gauge-dependent labels must not become distinct physical predictions without an additional physical coupling.

5.2 Thermal dynamics and the two state guides

For a specified preferred axis n, define

$$H_0=\frac{\Delta}{2}(I-n\cdot\sigma),\;p_{eq}=\frac{1}{1+e^{\Delta/(k_BT_b)}}.$$

Here $\Delta>0$ is an energy gap and T_b is the bath temperature. The implemented reference channel has

$$p_e(t)=p_{eq}+\left[p_e(0)-p_{eq}\right]e^{-\Gamma_1 t},\;\rho_{ge}(t)=\rho_{ge}(0)\,e^{-(\Gamma_1/2+\Gamma_\phi)t}.$$

These are standard completely positive, trace-preserving (CPTP) thermal and dephasing dynamics [R7]. The STO profile supplies selected reference coordinates; the rates and bath coupling must still be specified. The code explicitly preserves this distinction. The new thermal correspondence fixes the detailed-balance ratio in TASL coordinates:

$$\frac{\gamma_\uparrow}{\gamma_\downarrow}=2^{-\Delta\Theta(T_b)/(c^2h)},\;p_{eq}=\frac{1}{1+2^{\Delta\Theta(T_b)/(c^2h)}}.$$

This determines the relative populations once the energy gap and Anglar are chosen. It does not determine the absolute relaxation or dephasing rates. A claimed STO holding-power prediction must supply those rates through the same dynamics.

In the repeated-preparation protocol, the prepared-state guide is the prescribed target and the before-repreparation guide is the state after one free-evolution interval. Coincidence means that the chosen channel and interval leave that target unchanged within the display's resolution. Deviation measures channel-induced drift relative to the target. It can change in angle, radius, or both. A privileged axis arises

from H_0 and the coupling; an equator has no universal thermodynamic penalty independent of those choices.

For a reset interval δt and target excited population p_t, the energy returned to the qubit is

$$\Delta E_{reset} = \Delta\left(p_t - p_{eq}\right)\left(1 - e^{-\Gamma_1 \delta t}\right).$$

For an equatorial target, $p_t = 1/2$, and the limiting energy-supply rate is $\Delta\Gamma_1\left(1/2 - p_{eq}\right)$. Pure dephasing alone changes coherence but exchanges no H_0 energy. Purification can nevertheless require work. With a controller reservoir at T_c, the reversible free-energy bound is

$$W_{min} \geq F\left(\rho_{target}\right) - F\left(\rho_{pre}\right), F\left(\rho\right) = Tr\left(H_0 \rho\right) - T_c S\left(\rho\right).$$

This is a bound under the stated control and reservoir assumptions, not a measured apparatus cost [R8]. A thermal ledger must keep it distinct from free-bath heat and from any proposed photon-frequency multiplier. Appendix C gives the construction; O3 records its physical comparison.

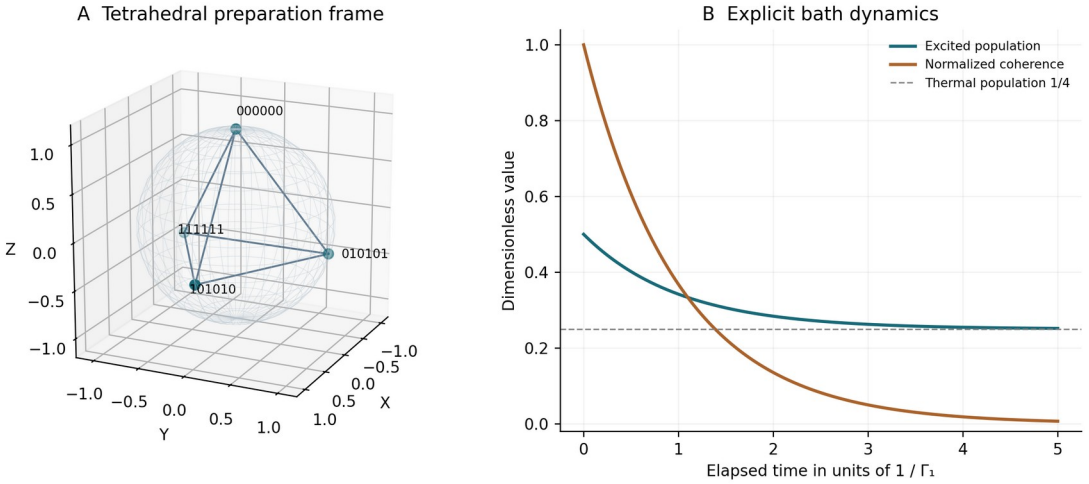

Finite realization of the bridge. A shows the actual tetrahedral preparation convention; all six tetrahedral edges have equal Bloch chord length. B shows an equatorial state under a declared bath model with equilibrium excited population 1/4 and pure-dephasing rate half the relaxation rate. The horizontal axis is dimensionless time. The bath parameters are chosen for illustration and are not fitted STO predictions.

5.3 Reproduced finite results and their scope

The accompanying script checks eleven groups of algebraic and numerical statements. It uses the supplied stack modules where specified and independently constructs the Lindblad superoperator for comparison. The checks were run with Python 3.12.14 and NumPy 2.3.5. They are separate from the earlier reported pytest suite and do not constitute a new run of that entire suite.

Check	Scope	Largest reported residual
Address partition	All 64 words	Exact 4, 36, 24 counts
Tetrahedral Bloch Gram matrix	Four preparations	6.11×10^{-16}
Hopf fibers	Six fibers with four representatives	4.47×10^{-17} in density matrices

Check	Scope	Largest reported residual
Hermitian-generator exponentials	72 axis, sign, chirality, and permutation cases	1.33×10^{-15} in $U^{\dagger}U - I$
Thermal channels versus Lindblad exponential	16 temperature and rate cases	2.22×10^{-16} in output matrices
Trace preservation	Same 16 cases	2.22×10^{-16}
Normalized Choi positivity	Same 16 cases	Minimum eigenvalue 0
Pure-dephasing energy check	Equatorial state, fixed H_0	Zero heat with purity reduced to 0.567668

The remaining groups check ATCS–TTDL capacity, raw calibration closure, implementation agreement with the corrected catalyst, unit invariance of normalized counts, and the TASL–Unruh matching relation derived below. Source and module hashes accompany the results.

These results establish a functioning finite quantum model with STO-directed control and accounting. They do not establish quantum hardware, a measured unitarity loss, an Einstein-equation solver, or a continuum field theory. Residuals of order 10^{-16} to 10^{-15} in a unitary check are numerical errors; their variation is not a measure of physical error-correction strength. Recovery requires a noise model, an encoding, and a recovery test.

Fresh execution of the supplied circuit paths

The 26 October audit [N31] executes the supplied source, rather than treating implementation as a future possibility. The selected source tests cover the Bloch controller, DRC metrology, certified AME artifact and metaplectic lift: 125 passed on the first run; the sole interruption was a missing SymPy dependency, and the remaining test passed after installation. No theory or source test was altered. The combined outcome is 126 passed, with the original run and single-test retry both retained.

Execution path	Fresh check	Result
Bloch controller	Six prime-DR choices at four ticks; execute and replay	24 receipts replay; maximum unitarity residual 7.86×10^{-16}
Certified AME(4,6)	All three 36 by 36 flattenings	Maximum singular-value deviation 1.91×10^{-14}
Metaplectic AME to MPS	Three phase masks and three product-basis inputs	Nine full-operator executions; maximum dense-to-MPS error 4.21×10^{-15}
Double-cover lift	Source cocycle, operator and phase-tracker tests	All eight selected lift tests pass

These are connected circuit paths in the supplied stack. The production AME tensor is a hash-attested numerical artifact with search provenance; its finite certificate does not by itself turn that artifact into an analytic STO derivation. The older dual-unitary construction is retained only as a contrasting fixture and is not substituted for the production tensor. The full 36-dimensional operator is used; a leading 4-dimensional QR proxy is excluded by the production interface.

Appendix M1 embeds the executed finite unitary in continuous spatial functions. Its numerical witness preserves norm within floating-point precision. Appendix M2 verifies conservation for an autonomous generator and accounts separately for the nonzero system-energy change under a driven gate. These checks close the finite implementation questions addressed here; physical identification tasks are consolidated in Section 10.

5.4 Translation phases and periodic operator classes

The attached articles identify two useful extensions of the finite model [N9]. Bloch's theorem concerns a Hamiltonian commuting with discrete translations; its phase labels are distinct from the qubit Bloch sphere. A comparable integer action appears in the theta-sector description of Yang–Mills theory. This connection already exists in gauge-theory literature: winding sectors carry phase characters of an integer group, while a Bloch band carries characters of lattice translations [R24–R26]. Their physical interpretations differ, since a gauge-sector parameter is not generally a freely selectable crystal momentum.

STO can use the common representation structure without postulating globally flat space. Repeated internal closure labels may carry an integer action over a curved base. The substantive construction is then to define its operator, prove its compatibility with the Hamiltonian and state which phase distinctions are observable. An exact scalar phase multiplying an entire spinor remains unobservable in its density matrix. Appendix H3 gives a finite cyclic realization and its integer-limit interpretation; it is a proposed extension, not a claim that the current code already simulates a Yang–Mills theta vacuum.

The lower periodicity diagram in the Bott article explicitly uses I Ching trigrams as a mnemonic for an eightfold classification. The relevant mathematical result concerns real Clifford algebras and graded modules; the complex case has period two [R23]. Binary notation is a useful indexing device, but an operator correspondence must preserve the algebra's multiplication, generator squares and grading. Appendix H4 specifies that test. It starts from the existing PC10 and G2 results in Appendix D4; it does not substitute chord values for prime-count symbols or reopen those finite proofs.

These connections refine the proposed common model. The address vocabulary supplies a finite state grammar, translation symmetry supplies phase characters, Clifford structure supplies spinor and grading data, and TASL supplies thermal weights. The correspondences can be combined only through explicitly compatible operators. Similar labels, repeated counts or the occurrence of π alone do not establish that compatibility.

5.5 Time manifold routing and finite quantum capacity

The Time Manifold operator card [N27] identifies the DR tags 819, 891 and 981 with the Hamiltonian families 9-1/9-8, 9-2/9-7 and 9-4/9-5, while 999 permits a universal junction subject to the remaining rules. Its contribution is to specify admissible transition support before selecting a dynamical generator. Appendix L3 constructs a weighted Laplacian on a reversible allowed sector and shows exactly which weighted quantity it conserves. The same self-adjoint operator can supply both unitary evolution and TASL-weighted thermal states. Directed chirality requires its own compatible generator rather than automatic symmetrization.

The source's finite chord budget becomes a quantitative entropy bound once channel occupancy, representation multiplicity and system size are bounded. Appendix L4 states that conditional theorem and the corresponding tensor-network cut bound. The two-period spine and four geometric spans are retained with explicit operator domains in L2. These additions turn the source's finite-ladder proposal into testable

constructions; they do not recategorize a software-imposed capacity limit as an independently measured universal limit.

6 A conditional gravitational closure

6.1 Two thermal identifications

The EMI construction proposes that TASL should supply the thermal coordinate in a local horizon argument [S292]. Two identifications must be distinguished.

For a static equilibrium metric with lapse $N=\sqrt{-g_{00}}$ in the chosen time-coordinate normalization, the Tolman relation is $T\,N=T_{\infty}$ [R5]. TASL reproduces it if

$$\Theta(x)=\Theta_{\infty}N(x),\Theta_{\infty}=\theta_k/T_{\infty}.$$

Within this static correspondence, $\beta_T(x)=N(x)\beta_{\infty}$. For energy E_{ξ} associated with the timelike Killing flow, a static observer measures $E_{loc}=E_{\xi}/N$. Therefore $\beta_T(x)E_{loc}=\beta_{\infty}E_{\xi}$: the TASL Gibbs factor agrees across those observers after lapse normalization. Likewise the proper Euclidean thermal interval is $\tau_E(x)=N(x)\hbar\beta_{\infty}$. This is a direct compatibility statement between the thermal operator in Section 4.4 and the static curved geometry. It uses Tolman equilibrium and the specified observer family, without identifying every temperature with acceleration.

For a locally accelerated observer, the Unruh temperature is $T_U=\hbar a/(2\pi c k_B)$ [R4]. Substitution into TASL instead requires

$$\Theta_a=\frac{\theta_k}{T_U}=\frac{4\pi^2c^3}{a\ln 2}.$$

Proposition 4. These two thermal descriptions are algebraically compatible when their Anglar coordinates satisfy the preceding relations. Using the same thermal field for both also requires $a\,N$ to be constant. This occurs for the usual Rindler congruence, where $N=a_{ref}\xi/c^2$ and $a=c^2/\xi$.

This result defines the conversion for this particular correspondence with the local-horizon theorem. The Unruh relation is a theoretical input to that comparison, not an experimentally settled axiom imposed on every STO branch. STO may instead derive a native response law and compare the same detector observable in its regime. No globally flat spacetime is required. In particular, the identification $\Theta\propto a/c$ appearing in one passage of EMI would make TASL temperature inversely proportional to acceleration. The consistent identification is inverse in a, with the displayed dimensional coefficient. This repair preserves TASL and the intended horizon route.

The selected gap-profile temperature and wavelength are fixed by the STO branch in Appendix A3. Equating two entropy-count expressions is not used to choose that temperature. The accelerated-observer identification above is an additional premise of the conditional horizon theorem, with its own observer and geometric assignment.

6.2 Horizon capacity and entropy density

Let N_t be a coarse-grained tile count, realized from ATCS capacity in the horizon construction. Introduce a physical area per tile $a_* > 0$ and an entropy increment per tile $s_* > 0$:

$$A = a_* N_t, \, dS = s_* dN_t, \, \eta = \frac{s_*}{a_*}.$$

If each independent tile has q equiprobable states, then $s_* = k_B \ln q$ at maximum entropy. A pure tile has zero von Neumann entropy, and correlated tiles do not generally have additive entropies. The horizon statement is therefore a statement about an ensemble or reduced state, not merely the size of an address set. ATCS–TTDL gives an exact count-to-content scaling; an entropy density additionally needs the physical area assignment and statistical state.

This identifies a precise place where the Bloch model can contribute. It provides local density matrices and tensor compositions from which a boundary entropy can be calculated. To claim a horizon area law, the construction must show that the *variation* of that entropy is proportional to the *physical* area variation in the relevant equilibrium family, with an orientation- and refinement-consistent coefficient. Appendix B now records the selected four-state capacity construction and a proposed finite response extension. It keeps the fixed-area capacity and variable-occupancy response as distinct constructions.

6.3 Conditional compatibility theorem

Theorem 1 — STO horizon compatibility. Suppose an STO realization has a smooth four-dimensional Lorentzian limit with the following properties:

1. Every point admits local causal horizons in all null directions, with expansion and shear vanishing at the reference cross-section.
2. The same local accelerated observer measures the heat flux and temperature; the TASL coordinate is $\Theta_a = 4\pi^2 c^3 / (a \ln 2)$.
3. Horizon entropy has local variation $dS = \eta \, dA$, where $\eta > 0$ is constant in the region considered.
4. Heat is the flux of a symmetric conserved stress tensor T_{ab}, and local equilibrium obeys $\delta Q = T \, dS$.

Then, to the leading local-equilibrium order,

$$G_{ab} + \Lambda g_{ab} = \frac{8\pi G_{eff}}{c^4} T_{ab}, \, G_{eff} = \frac{k_B c^3}{4\hbar\eta}.$$

Here Λ is an integration constant. If the stress tensor is a renormalized quantum expectation value in a regime of small stress fluctuations, the same conclusion gives the corresponding semiclassical closure, subject to the effective-action qualifications in Section 7.

Proof. Choose an affine parameter λ of length dimension, vanishing at the reference cross-section and negative on the past horizon. With dimensionless tangent k^a, the approximate boost vector can be normalized as $\chi^a = -(a/c^2)\lambda k^a$. Hence

$$\delta Q = -\frac{a}{c^2} \int \lambda T_{ab} k^a k^b \, d\lambda \, dA.$$

The equilibrium conditions and Raychaudhuri equation give $\vartheta = -\lambda R_{ab} k^a k^b$ at leading order, and therefore

$$\delta A = -\int \lambda R_{ab} k^a k^b d\lambda d A .$$

Inserting TASL with the acceleration coordinate into Clausius balance gives, for every null direction,

$$R_{ab} k^a k^b = \kappa T_{ab} k^a k^b , \kappa = \frac{2\pi k_B}{\hbar c \eta} .$$

The null-contraction identity implies $R_{ab} - \kappa T_{ab} = F g_{ab}$. Conservation and the contracted Bianchi identity give $\nabla_b F = 1/2 \nabla_b R$, so $F = R/2 - \Lambda$. Substitution yields the result and the stated G_{eff}. ▫

The proof completes the tensorial step proposed in EMI using the local-horizon method of Jacobson [S292, R3]. Its distinctive STO content is the capacity, thermal-coordinate, and finite-state realization assigned to the hypotheses. It does not claim that replacing their names changes the underlying horizon theorem.

The selected PC10 horizon register has $q = 4$ orthogonal states per tile [N10]. Its saturated capacity is $s_* = k_B \ln 4$, so the associated coupling, if this is also the geometric response coefficient, is

$$G_{eff} = \frac{c^3 a_*}{4\hbar \ln 4} = \frac{c^3 a_*}{8\hbar \ln 2} .$$

This replaces the previous binary-tile denominator. At fixed tile area the coupling is half the binary value. The selected saturated state alone does not establish the required fixed-system first-order response; Appendix B gives that calculation and a weighted-state construction. Matching measured G at this coefficient would require $a_* = 4 \ln 4 \, \ell_P^2$, with $\ell_P^2 = \hbar G / c^3$. Conversely, predicting a_* independently would predict the coupling. Choosing a_* through measured G is calibration, not an independent derivation of Newton's constant. Neither 384 nor the $3/2$ volume exponent alone fixes a dimensionful a_*.

The theorem requires no globally flat background. It does require a local Lorentzian tangent structure. It also does not require strictly positive null focusing in every state. A Ricci-flat region has zero null Ricci contraction, and a null radiation stream has zero contraction along its own direction. Quantum matter needs entropy-sensitive conditions such as the quantum null energy condition in its applicable regimes [R15], rather than an unconditional classical positivity assertion. These restrictions concern the domain of the focusing claim, not rejection of the STO geometric premises.

6.4 Reconciliation of the new horizon construction

The new horizon insertion [N15] makes the intended sequence explicit: TASL temperature, ATCS tile count, TTDL content scaling, entropy response, Raychaudhuri focusing and a conserved total stress. Theorem 1 completes that sequence with consistent local flux normalization. In particular, heat is the flux associated with the same boost observer that defines the temperature. Omitting the factor $-(a/c^2)\lambda$ from that flux leaves unequal affine-parameter weights on the two sides of Clausius balance and does not imply the pointwise Einstein relation.

The proposed Planck-area expression has a precise place in the construction:

$$\eta = \frac{k_B}{4\,\ell_P^2},\ \ell_P^2 = \frac{\hbar G}{c^3} \Rightarrow G_{eff} = G.$$

This is an exact calibration identity. For the selected four-state tile it is equivalent to $a_* = 4\ln 4\,\ell_P^2$, provided the capacity increment also realizes the physical area response. It does not fix the area from ATCS–TTDL alone because the displayed Planck scale already contains G. A native STO prediction would determine a_* and the applicable entropy slope before importing that coupling. Likewise the temperature can be derived natively if the state and its boost generator produce the required thermal response; merely defining $T = \theta_k / \Theta$ leaves Θ_a to be fixed. These are the concrete identification steps, not a requirement to adopt a globally flat background.

The count-to-volume law $V \propto C^{3/2}$ is retained with a volume carrier. It does not itself turn a two-dimensional count into a physical area. Nor does global nonflatness entail $R_{ab}k^a k^b > 0$ along every ray. The local theorem retains its equilibrium and focusing domain rather than replacing the original STO premise by that stronger condition. The new insertion therefore strengthens the explicit construction path while leaving the same physical area, state-response and observer-boost questions identified in Appendix B.

7 From finite quantum states to covariant fields

The finite Bloch realization and Theorem 1 share the proposed construction below: a common state sector, generator, thermal map and variational stress. Appendix M gives its explicit discrete and continuous-space realization. Section 10 identifies the physical maps needed to promote this construction to a field correspondence.

Proposed completion 1 — A local field family. Resolve the continuous spatial carrier of M1 with a sequence of causal cell complexes Γ_ϵ with decreasing physical cell diameter ϵ. Use STO rules to label admissible local states and transformations, while assigning physical edge lengths, lapse, and spatial volume to the cells. The K9 routing graph is an internal control structure; its edges must not be silently identified with arbitrary instantaneous connections across physical space. A relation between control adjacency and causal spatial adjacency must be specified.

On each spatial slice let M be the finite-element mass matrix and K the stiffness matrix determined by the metric and basis functions. In units $c = \hbar = 1$, a candidate scalar Hamiltonian is

$$H_\epsilon = \frac{1}{2}p^T M^{-1} p + \frac{1}{2}\phi^T K\,\phi + \frac{m^2}{2}\phi^T M\,\phi + V_\epsilon(\phi).$$

For a fixed spatial metric with unit lapse and zero shift, $M_{ij} = \int \sqrt{h}\,N_i N_j\,d^3x$ and $K_{ij} = \int \sqrt{h}\,h^{ab}\partial_a N_i \partial_b N_j\,d^3x$. This gives the edge weights a physical geometric definition. The matrices M and K here are not the m-point mass or a temperature. Nontrivial lapse, shift, or time-dependent slicing requires the corresponding weighted matrices and canonical treatment.

A finite oscillator truncation can encode these degrees of freedom in qubits. It cannot satisfy the exact canonical commutation relation in finite dimension, because the trace of a matrix commutator is zero. The

construction must therefore control the truncation error and take a suitable low-energy and refinement limit. Local qubit gates alone do not establish that limit. Appendix C sets out concrete checks.

The desired low-energy matter action is, for example,

$$S_m = \int d^4x \sqrt{-g}\left[-\frac{1}{2}g^{ab}\nabla_a\phi\nabla_b\phi - \frac{1}{2}\left(m^2+\xi R\right)\phi^2 - V(\phi)\right].$$

This is a candidate covariant completion, not an action already derived from ATCS. In this regime the stress tensor is defined from that same action by $T_{ab} = -\left(2/\sqrt{-g}\right)\delta S_m/\delta g^{ab}$. Local symmetry gives its on-shell conservation. For quantum fields, a state prescription and a renormalized stress tensor are needed [R1]. The admissibility rules must survive this limit without generating observable preferred-frame propagation inconsistent with the intended Lorentzian limit.

Proposed completion 2 — Geometric response. Demand that the low-energy geometry satisfies Theorem 1 with the matter tensor just defined. The corresponding effective gravitational action begins, in natural units, with $\left(16\pi G_{eff}\right)^{-1}\int\sqrt{-g}\left(R-2\Lambda\right)d^4x$, together with allowed higher-curvature terms. Curved-spacetime renormalization generally requires such terms. Their neglect must be justified by a scale separation, rather than calling the leading Einstein form exact at every scale [R2]. If the entropy density changes with curvature or occupancy, extra response terms and, potentially, nonequilibrium entropy production must be derived [R13].

Proposed completion 3 — Quantum geometry. A semiclassical metric sourced by $\langle T_{ab}\rangle$ is an intermediate description. A microscopic construction would require joint geometry–matter states, a physical inner product, constrained evolution, and a prescription for relational observables. Schematically, one could introduce geometry-labeled sectors with conditional matter generators and a geometry-transition operator. This is only a starting ansatz until constraint closure, a classical metric limit, and causal quantum dynamics are proved. A state-dependent classical metric update is not automatically a linear quantum evolution and needs a separate no-signaling analysis.

The benefit of the STO approach is that fundamental metric quantization need not be the first operation. The geometry may be a collective response. The corresponding obligation is to derive that response from specified microscopic states and dynamics. Avoiding an assumption can remove a formulation-specific obstruction; it cannot replace the observable predictions that made the original problem substantive.

7.1 A common real time and thermal transfer construction

The exact TASL–beta map permits a concrete completion of one part of the common-dynamics requirement. For a self-adjoint, bounded-below candidate H_ϵ in a finite cell model, use that same Hamiltonian to define

$$U(t) = e^{-iH_\epsilon t/\hbar}, K(\delta\tau) = e^{-H_\epsilon\delta\tau/\hbar}.$$

Choose $N\delta\tau = \tau_E = \hbar\beta_T$. Then

$$K(\delta\tau)^N = e^{-\beta_T H_\epsilon}, \Theta = \frac{2\pi}{\ln 2}c^2\tau_E.$$

This is an exact finite operator construction: one energy spectrum supplies unitary evolution and a Gibbs state with the STO thermal coordinate. It does not select that spectrum. A physical discrete step can be retained, in which case the allowed N and thermal boundary prescription must be stated; taking a

continuum limit is an additional choice. The positive imaginary-time transfer K is not a physical noisy gate, and its failure to be unitary is not a measured thermal-curvature impedance.

Thermal field theory imposes periodic bosonic and antiperiodic fermionic boundary conditions around the Euclidean interval τ_E [R27]. A fermionic field therefore recovers its sign after two such intervals. This supplies a precise comparison with STO's two-period construction, while retaining the distinction between imaginary thermal time, real clock recurrence and rotation of a spinor. In the gap branch,

$$t_B = \frac{\Theta_B}{c^2} = \frac{h}{k_B T_g \ln 2} = \frac{2\pi}{\ln 2}\tau_E\left(T_g\right).$$

The scale conversion is fixed. The factor displayed above is the operational coordinate conversion; it does not identify imaginary time with elapsed duration. The corresponding physical horizon identification is O2. H3 and B supply the phase and entropy constructions.

7.2 Metric response and observable travel time

The new notes propose an occupancy-driven metric update and compare arrival times along different paths [N10]. This is a useful place to connect the observer-inclusive ledger to a measured quantity. The update must preserve the Lorentzian signature and follow from the selected metric and field equations, or be explicitly declared as a discrete evolution postulate. A potential's metric derivative defines a stress contribution; it does not by itself determine a time-stepping law. If ϵ_{curv}/c^2 is dimensionless, multiplying it by a physical time step also requires a declared inverse-time carrier before it can scale a dimensionless metric increment.

A null path has zero proper interval in a curved metric as well as a flat one. The integral $\int\sqrt{-g_{\mu\nu}dx^{\mu}dx^{\nu}}$ therefore cannot be used as its flight distance or arrival time. Keeping the coordinate vector $(1,1,0,0)$ fixed while changing the metric can make that vector non-null; a resulting nonzero norm is not an elongation of a null proper length. An affine parameter and an observer's elapsed time are separate quantities.

For a static metric with no time-space cross terms, write

$$ds^2 = -N^2(x)c^2dt^2 + h_{ij}(x)dx^i dx^j.$$

The null condition gives the coordinate flight time along a ray,

$$t[\gamma] = \frac{1}{c}\int_{\gamma}\frac{\sqrt{h_{ij}dx^i dx^j}}{N}, \Delta\tau_{obs} = N_{obs}\left(t\left[\gamma_i\right] - t\left[\gamma_j\right]\right).$$

This construction realizes the intended path comparison while retaining zero null proper interval. A time-dependent STO metric instead requires solving the null propagation and observer-clock equations together. Equal Euclidean path lengths do not imply zero relativistic delay: the lapse and spatial metric still enter. A proposed additional STO delay must consequently be calculated from its specified metric response and compared with the same lens, source and observer model. The curvature integral in Appendix E3 remains a dimensionless redshift coordinate; converting it to seconds needs an explicit length and clock map.

7.3 Spatial closure and the geometric flow proposal

The Time Manifold chapter proposes spherical closure and a common Laplacian structure across routing, thermal transport and nuclear differences [N27]. Appendix L separates a bounded three-region with an S^2 boundary from a closed S^3 spatial manifold and gives a two-ball gluing construction. A closed simply connected three-manifold has S^3 topology; deriving those topological hypotheses from STO's physical closure criteria remains distinct from invoking the mathematical theorem. No global flat metric is assumed.

To link the finite routing operator to curvature, L5 proposes a metric reconstruction map and an explicit update-to-Ricci-flow limit. This identifies the missing mathematical map rather than introducing a new acceleration calibration or changing TASL. A scalar graph diffusion is already constructible; its identification with metric flow and the subsequent relation of that flow to Lorentzian time require additional dynamics. The Einstein-equation closure continues to depend on the same horizon entropy and covariantly conserved stress account established in Section 6. Thus the new source supports a more explicit route toward a common microscopic model without conflating Ricci flow with the Einstein field equation.

8 Mass emergence and conservation

The source's phrase "persistence of geodesic displacement" can be given a testable spectral meaning. Let the admissible transport operator define a positive quadratic form with normal modes. If its long-wavelength, Lorentz-compatible limit has a dispersion relation

$$\omega^2 = c^2 |k|^2 + \omega_0^2, m = \frac{\hbar \omega_0}{c^2},$$

then the persistent mode at zero spatial momentum has rest energy $m c^2$. This is a proposed construction linking the dual-geodesic idea to an observable mass. Its required steps are to define the physical transport operator, demonstrate the gap's stability, establish the dispersion relation, and distinguish a regulator gap from a gap stable under the limits claimed for that model, including infinite volume and, only where claimed, a continuum limit. A positive eigenvalue of a small routing matrix does not establish a mass gap in four-dimensional interacting Yang–Mills theory.

MFAT supplies a useful energy-to-information coordinate, $N_L = E / (k_B T \ln 2)$, under a specified erasure or occupancy convention. It does not make energy-free labels massive by definition. The m-point identity $m = h / \Theta$ establishes the mass coordinate corresponding to a chosen energy scale. Deriving a particle mass spectrum requires a dynamics that selects the scale.

The working outline also proposes a geometric flavor texture $Y_i = Y_0 \cos(\Delta\theta_i / \theta_0)$. It is an ansatz until the allowed angles, overall scale, flavor mixing, gauge representations, and renormalization prescription are fixed independently. Counting or summing scalar texture values cannot replace gauge-anomaly cancellation conditions. The current draft therefore does not claim to eliminate the Standard Model's Yukawa parameters [S297]. A productive test would freeze the angular assignment on part of the spectrum and predict withheld masses and mixing observables with propagated uncertainties.

The helical ledger has a similarly precise domain. For a conserved symmetric tensor and a vector ξ^a,

$$J^a = T^{ab}\xi_b, \nabla_a J^a = \frac{1}{2}T^{ab}\left(L_\xi g\right)_{ab}.$$

If $\xi = \partial_t + \Omega\,\partial_\phi$ is Killing, the associated charge is conserved and is represented by $E - \Omega J$ with consistent conventions. It is a linear combination of time-translation and rotation generators; it does not automatically add an independent Poincaré generator. If the vector is not Killing, the right-hand side is a balance term, not zero. Source [S021] can thus be formalized as a symmetry-aware accounting rule.

Within the observer-inclusive STO premise, changing the observation arrangement can change the physical coupling as well as the measured energy coordinate. The mathematical task is to represent that premise in a joint balance law. If a split into matter and observer–curvature sectors is useful, write $\nabla_a T^{ab}_{matter} = j^b$ and $\nabla_a T^{ab}_{observer+curvature} = -j^b$. The total tensor enters the horizon theorem. Neither sector is required to be an observer-independent material bath. Appendix M3 supplies a candidate total action; its Euler equations and the D3 identity determine the exchange current for a declared sector split. No independent fitted current is introduced. Physical selection of that action and the experiment distinguishing exchange from coordinate change are the O1 and O3 items.

8.1 The supplied occupancy tensor

The metrological ledger supplies an explicit symmetric occupancy tensor [E3]:

$$O_{\mu\nu} = \frac{4\pi r_\mu r_\nu + \pi\left(r_\mu d_\nu + d_\mu r_\nu\right)}{T_L} + \frac{M}{F}\frac{A_\mu A_\nu}{A_\alpha A^\alpha}.$$

Proposition. If r, d, A are covector fields, T_L, M, F are scalars, and contractions use a declared nondegenerate metric, this expression is a symmetric covariant rank-two tensor wherever its denominators are nonzero. Its trace is

$$g^{\mu\nu}O_{\mu\nu} = \frac{4\pi r^2 + 2\pi r\cdot d}{T_L} + \frac{M}{F}.$$

The first term has image contained in the span of r and d, while the mass term has rank one. Hence $rank\,O \le 3$ in four dimensions. Rescaling A by any nonzero scalar leaves the mass term unchanged. These statements follow directly from tensor products, contractions and linear algebra.

This construction supplies the tensor ansatz previously identified as missing. The remaining task is to specify the field meanings, normalization carriers and dynamics that make it a physical occupancy or stress tensor. Its rank bound excludes identifying it alone with a nondegenerate spacetime metric; it does not preclude its use as stress. Null values of A^2 require a separately defined sector. Setting the scalar F to one does not turn a rank-one dyad into the identity matrix.

A candidate potential sector can be constructed directly. In normalized variables, holding the covectors and scalar coefficients fixed under metric variation, define

$$L_0 = -\frac{2\pi r^2 + \pi r\cdot d}{T_L} - \frac{M}{2F}\ln\left(\frac{\left|A^2\right|}{A_0^2}\right).$$

Here A_0^2 is a fixed positive reference. Then $-2\partial L_0/\partial g^{\mu\nu}=O_{\mu\nu}$, and varying the invariant volume gives $T^{(0)}_{\mu\nu}=O_{\mu\nu}+g_{\mu\nu}L_0$. The occupancy dyads are thus the anisotropic terms of a possible variational stress. The new notes now supply this type of potential explicitly [N10]. Their printed spatial coefficients are twice those shown here; direct variation would give $2S_{\mu\nu}+M_{\mu\nu}$. We retain the supplied tensor and halve those two potential coefficients. Appendix D3 records the variation and covariant balance identity. The corrected sector requires its physical carrier and additional dynamics. In particular, unconstrained variation of A in the logarithmic term alone does not supply a nonzero stationary field at nonzero M/F.

Appendix M3 adds explicit kinetic and constraint terms to this potential sector. Varying the total action with respect to the metric defines stress. The explicit identity in D3 shows how field equations and observer couplings determine its balance law. Observer and curvature sectors can participate in that balance according to STO's stated ontology. Neither covariance nor symmetry alone establishes conservation. An explicit orientation or parity transformation is also required if the resulting coupling is to be called chiral.

For the fine-structure comparison, define $\epsilon_N=\epsilon/\epsilon_*$ and $s(\epsilon_N)=2\pi^2/\sqrt{\epsilon_N}-1$. The supplied reference 384.0113821238 yields $s=0.00729735256154$, whereas the ATCS value 384 yields 0.00731228107484. We report this as a strain correspondence at a declared reference. A normalized length coordinate is required when rewriting it using d and L_v. The scalar correspondence does not by itself derive the electromagnetic field equations; no derivation of imported constants is claimed here.

8.2 From thermal weights to a strain response

Compressibility and specific storage provide a useful constitutive construction for the occupancy proposal [N9, R29]. Define the isothermal compressibility $\kappa_T=-\langle V\rangle^{-1}(\partial\langle V\rangle/\partial p)_T$. In a classical isothermal–isobaric ensemble with microstate energies E_i and volumes V_i, the weights are proportional to $e^{-\beta_T(E_i+pV_i)}$. Direct differentiation gives

$$\kappa_T=\beta_T\frac{Var(V)}{\langle V\rangle}=\frac{\ln 2\Theta}{c^2h}\frac{Var(V)}{\langle V\rangle}.$$

This exact equilibrium relation connects TASL's thermal coordinate to a measurable response once a volume operator and ensemble are supplied. Appendix H5 derives it and states its quantum qualification. A positive finite compressibility gives a bulk modulus $K_{bulk}=1/\kappa_T$ and a small volumetric-strain free-energy density $1/2\,K_{bulk}\epsilon_v^2$ about a stable reference.

For STO, the proposed next step is to assign the existing occupancy states their energies, volumes and observer coupling, then calculate this response from the same partition function used in Section 7.1. This supplies a constructive route toward a constitutive coefficient rather than an unexplained scalar correction. The new notes propose water as a constitutive witness for that connection [N10]. This environmental calibration is separate from the raw theta-k catalyst, which contains no water input. The response must retain a declared material amount: a finite change in mean volume under pressure is not the fluctuation variance. At maximum density, the thermal expansion coefficient vanishes; this does not by itself minimize volume variance or select a 244-step quantization. Appendix I states the corresponding ensemble test. The metric variation and balance construction of Section 8.1 must connect this free energy to stress. The dimensionless geometric compression coefficient k_c is also distinct from a compressibility measured in inverse pressure.

8.3 A material readout for the shared stress account

The HTF briefing supplies an annular rotating-stress field with an added logarithmic compression term [N22]. Appendix K4 verifies radial equilibrium and the required boundary traction. It also calculates the elastic compatibility residual and proposes an explicit eigenstrain completion for review. These are distinct results: force balance is an exact consequence of the supplied field, while a physical eigenstrain and its coupling to the occupancy action remain constitutive choices.

The stress-optic relation then provides a possible measured response through birefringence and resonance shifts. K5 connects that material calculation to the total stress tensor used in the horizon argument, retaining the Cauchy-stress sign convention and null-vector normalization. A measured device response must separate ordinary elastic, thermal and optical effects from the proposed additional STO term. This yields a concrete route from the common stress account to a laboratory observable without treating octave arithmetic alone as a mechanism of energy transfer.

9 Evidence and discriminating tests

The evidence now spans exact finite calculations, reproduced galaxy diagnostics, fixed-response comparisons, archived target declarations and observational input audits. The results below identify what was actually tested. All finite G2 and operator results credited here originate in AxiomARC; they are not new structures invented during this reconciliation [E6].

Branch	Result retained	Scope of present evidence
AxiomARC operators	52 exact expressions; G2 chirality agreement for 108 K9 sequences; 12 selected source tests pass	Reproduced finite mathematics and software
October thermal and address audit	Exact TASL–beta closure; 6,384 assemblies; all 64 binary-pi addresses first seen at block 244	Algebra and deterministic finite enumeration; no detector or statistical-significance claim
Galaxy response	Fixed-response RMS 0.11908 dex; diagnostic fit RMS 0.11810 dex on the original baryonic profile	Same 171-galaxy sample; fixed and fitted pathways separated
Nuclear radius	Author-confirmed RMS neutron skin 0.311296 fm	Adopted occupancy-to-radius operator; uncertainty and transfer tests retained
Hydrogen ladder	$T_E = hf / \left(k_B \ln 2\right)$ reproduces the supplied spectral coordinates	Energy-equivalent temperature; ambient inference needs a response model
Yang–Mills targets	7.5 and 54 degrees; gaps near 0.215, 0.212 and 0.210 GeV	January 2025 document metadata and author attribution
Collider data	Associated AK5 arrays reproduce pT and angular results; corrected energy is distinct from eta	Historical energy labels resolved as eta; physical observable, provenance and statistical calibration remain
HTF spectral map	Six octave assignments reconstruct the spectral Anglar table	Coordinate closure; physical conversion and constitutive response remain proposed

Branch	Result retained	Scope of present evidence
Laboratory responses	Defined NMR coefficient-jump and rotating-resonator hypotheses	Prospective protocols with independent calibration and rejection conditions; no completed tests
Gravitational wave	H1 science-mode interval verified; Prime Locks reports specify correlations and proposed alerts	Processing provenance and causal forecast validation remain to be reproduced

The fixed-response galaxy comparison adopts the CRC relation $a_{STO} = c\,H_0/(2\pi)$. The source implementation sets the external reference to $H_0 = 67.4\,km\,s^{-1}\,M\,pc^{-1}$ [S028, S035, S208]. Within the supplied interpolation family, the flat-outer-curve condition fixes the exponent at one quarter, and matching the asymptotic acceleration coefficient fixes $g_* = a_{STO}/\pi^{3/2}$. Neither is optimized in this evaluation. This conditional construction must be distinguished from `ntestgal1.py`, which explicitly optimizes both entries. The author has confirmed this response dictionary; its weighted RMS becomes 0.16751 dex under a signed-gas profile with disk/bulge multipliers 0.5/0.7. Appendix E2 records both outcomes, competing fixed responses and the derivation's scope.

The nuclear addendum contains enough structure to reconstruct its otherwise unstated RMS averaging step. The author has now confirmed that operator, which is adopted in Appendix G. Its skin value differs from the PREX reference central value by about 0.40 of the quoted measurement standard deviation, before assigning model uncertainty [N2, R17]. This single agreement is retained as a conditional comparison, not a validation of the complete atomic model.

The original Ly-alpha report remains a five-object consistency exercise with a mean absolute difference of 2.04 percentage points calculated from its displayed pairs [S012]. Several paths reuse the comparison observable, and Haro 11 is matched by construction. The supernova script still tests an observer-frame width law only if its input width has not already been transformed to the rest frame [S205]. CRC and expanding-background models can share a $1+z$ width relation, so discrimination requires an additional observable specified before fitting.

The gravitational and collider inputs now have concrete source locations. The updated CERN arrays supply low-valued AK5 coordinates, valid source-entry offsets and distinct energy and eta fields [N20]. The audit now recounts the reported pT windows and their angular comparisons, while locating the historical energy-labelled results in eta [N21]. Appendix E4 states the successful replay and the remaining requirements for physical interpretation and calibrated significance. Appendix E5 gives prospective laboratory response tests, with the predicted response separated from the conventional device baseline.

The October audit checks the two supplied working modules and the new thermal and hydraulic identities [N7, N8]. Its binary-pi evaluation uses the first 240,000 fractional bits in nonoverlapping six-bit blocks. First coverage at block 244 is independently calculated rather than imposed by the source helper's 244-block slice. The internal assembly count is 6,384, with maximum per-address depth 507 at `101010`. Occurrence quotas and legal execution of every assembly are different observables; Appendix H6 records exactly what the script establishes.

10 Consolidated remaining validation and completion

This is the manuscript's single register of outstanding work. The completed algebra, confirmed reference maps and fresh finite circuit executions are not conditional tasks. Proposed completions M1–M3 are

supplied explicitly for review; their proven finite properties are distinguished from their physical interpretation. Publishing this conditional construction does not require resolving every question about quantum gravity.

O1 — Select the common physical field realization. Adopt or amend the continuous-space embedding, constrained occupancy action and autonomous global-energy construction in Appendix M. The construction already gives a resolved spatial carrier, bounded finite generator, thermal state and variational stress prescription. To identify it with the physical EFE–QFT bridge, specify the physical mode basis, coupling coefficients, lapse/observer dynamics and route-to-metric map. Evaluate the constraint equations, stability and causal propagation in the selected sector. Use the existing G2, PC10 and executed circuits as inputs. A spacetime-local field algebra, gauge constraints and low-energy scattering or dispersion comparison then test the claimed field correspondence; circuit unitarity alone is a narrower result. Global energy conservation is the STO premise, but equality of the discrete conserved account with a specified continuum charge is still a physical map. A generic curved metric need not possess a time-translation Killing field. Physical ultraviolet or vacuum-energy claims require controlled low-energy predictions and a vacuum response from the chosen dynamics, not an assumption of globally flat spacetime.

O2 — Fix the physical horizon response. The quaternary capacity state and weighted-state entropy response are calculated in B. Select the physical area operator, its carrier and the horizon/boost generator from O1. Compute the entropy-area slope and thermal response for that same state. Theorem 1 then gives the local Einstein closure under its stated hypotheses. Importing G through a Planck-area assignment establishes normalization consistency; predicting G requires an area scale fixed without that input. TASL profile temperatures remain their supplied values: A3's optional entropy-bound correspondence is not an imposed replacement temperature. The discrete tick and clock charts in A5 are fixed; relative-motion and gravitational-lapse comparisons must use those maps in the selected geometry.

O3 — Specify the observable identifications. The derivation $w = \ln 2/3$, its gap coordinate in A6, the strain ratios and the m-point relations are completed model consequences. For an electroweak claim, declare whether w is $\sin^2\theta_W$, a phase or another observable, and state its physical measurement convention and scale. The source's information partition is not rejected because this additional map is required. For HTF, retain the derived speed and octave chart, and compare the predicted material propagation and optical response with independent measurements under fixed boundary conditions. The stress-optic, 0.1 mm metrology, NMR and rotating-resonator proposals retain the explicit constitutive parameters and sensitivity protocols in E5, J and K. Those coefficients and response measurements supply the physical correspondence; matching coordinate numbers is not a substitute for them. A Bott or Bloch-theorem identification additionally needs the stated algebra-preserving or translation-covariant operator map; the existing finite G2 proof is not the unresolved item.

O4 — Complete empirical validation with the supplied records. For CERN, retain the successful associated-array replay and supply only a compact per-file extraction invocation, environment record and validated-run/source-entry certification, plus run/luminosity/event identifiers when cross-file deduplication is claimed. Freeze the observable-to-STO prediction, zero-record treatment and event-grouped angular/null statistic before evaluating significance. The original ROOT files need not be transferred again for this step. For GW, bind the historical exported series to calibrated strain and its processing receipt, then execute the declared causal statistic on held-out intervals with the leakage controls in E3. For galaxies, keep the confirmed fixed response and external reference inputs separate from diagnostic fits; report baryonic-profile and measurement uncertainty and test transfer. For the nuclear comparison, fix point-proton versus charge-radius conventions, model uncertainty and an isotope

transfer set. These are validation of existing numerical results, not requests to retune the models to their targets.

O5 — Bound stronger implementation claims. The three executed paths and 126 selected source tests establish the finite model documented in Section 5. Claims of physical error correction require an encoded noise-and-recovery benchmark that preserves unknown logical states; re-preparing a known state is not that benchmark. A full physical spin or metric identification, hardware performance claim, universal entanglement ceiling, or singularity-resolution claim is outside those finite certificates. Such extensions are optional separate results, not hidden prerequisites for reporting the present construction. Routing deadlock and cryptographic claims likewise remain outside the EFE–QFT scope.

O6 — Final author review and release. Confirm which M constructions become adopted branches, resolve any resulting carrier/coupling choices, and supply affiliations, corresponding-author contact, acknowledgments and permission to redistribute source archives. Review the P/C/M/O labels against the final claims and experimental scope. Journal or preprint submission requires a separate release decision. All material and code runs reported here remain review artifacts, not a submitted or experimentally certified reconciliation.

11 Discussion and conclusion

The updated STO construction starts with discrete geometric time, continuous curved space and closed global energy conservation. Time supplies the resolution bandwidth; finite address counts describe resolved configurations. ATCS and TTDL yield the shared geometric capacity, TASL fixes thermal conversion, and the LT rotation carrier makes the HTF dimensional calculation explicit. Equal allocation of binary information among three spatial degrees derives $\ln 2/3$ and the 66.5844417251 K gap coordinate without using water, pressure or gravity as calibration inputs.

The finite quantum part is executed. Bloch states, certified AME structure and metaplectic closure operate through the supplied AxiomARC modules, with numerical replay and dense-to-MPS agreement. Appendix M constructs an isometric embedding in continuous spatial functions and an energy-conserving autonomous update. A controller-inclusive ledger accounts for driven gates. The variational occupancy potential, constrained completion and selected horizon response give a concrete route to the conditional Einstein closure in Section 6.

The fixed galaxy and nuclear comparisons, bounded CERN recount, historical GW records and prospective material protocols remain tied to their stated observables and provenance. The contribution is a mathematically specified and computationally exercised common framework. Section 10 identifies the physical maps and tests needed to promote that framework to a validated field reconciliation. It preserves the distinction between exact consequences of STO’s premises and independent physical confirmation without treating the premises as refuted by a different starting convention.

Author contributions

Christopher Schiele is the primary author and developed the theory of SpaceTime Occupancy and the computational design of AxiomARC. Alex Malyuta contributed AxiomARC development, initial engineering, and theory testing against third-party SPARC and CERN data. Paul Schiele contributed AxiomARC testing in third-party Runpod and Vast.ai environments and design feedback. These roles and the author order are recorded from the supplied authorship statement [N14].

Appendix A Reference quantities and algebraic completion

A1 Unit-covariant angular counts

Start with physical θ_k, select T_*, and form $\Theta_k = \theta_k / T_*$. Select q_* with the same dimensions as Θ_k, then define $n_k^2 = \Theta_k / q_*$. If lengths are expressed in centimeters instead of meters, the numerical values of both Θ_k and q_* multiply by 10^4; the ratio is unchanged. Forming n_k from the changed numerator while retaining the bare number 10800 changes the reference rather than merely changing units.

The source's conversion can now be written as an angular chart followed by an area chart: $a = \pi \Theta_k / q_*$ and $n_k = \sqrt{a/\pi}$. Pi cancels exactly. This supports the intended operational grammar of diameter counts and radius reduction while exposing the calibration carrier. The same method applies to each energy catalyst. **Author-confirmed convention:** $T_* = 1$ K and $q_* = 10800\, m^2 s^{-1}$ define the current chart. This method was confirmed during reconciliation on 26 September 2026. Changes of units transform the quantity and carrier together; changes of physical reference define a new chart and are recorded separately.

A2 Rotation and the corrected curvonic convention

The corrected convention is $E_{curv} = 2\pi O$, with $2\pi O \simeq 383.997935$ in the rotation comparison chart. It is not $O = 384$ followed by another multiplication by 2π.

To express the source's intended dimensions without assigning dimensions to the mathematical number π, introduce an Anglar carrier A_* of dimensions $L^2 T^{-1}$, the STO rotation-period quantity $P_{LT} = X_{LT}$, always of dimensions LT, and a periodic rate ν of dimensions T^{-1}. Define

$$\epsilon_{curv} = 2\pi A_* \sqrt{X_{LT}/c}\, \nu^2, O_\epsilon = A_* \sqrt{X_{LT}/c}\, \nu^2.$$

Since $\sqrt{X_{LT}/c}$ has dimension time, ϵ_{curv} is a specific energy in $L^2 T^{-2}$. Choosing $A_* = 1\, m^2/s$, $X_{LT} = 86400\, m\, s$, and $\nu = 60\, s^{-1}$ reproduces the source number in J/kg. The inverse is $X_{LT} = c\left[\epsilon_{curv} / \left(2\pi A_* \nu^2\right)\right]^2$. The symbol rotation period in this paper denotes P_{LT}, never a bare duration. An elapsed duration is instead $t = P_{LT} / \ell_*$ for a declared length carrier ℓ_*. Thus the coefficient 86400 is not by itself a statement that P_{LT} has units seconds.

A total energy requires multiplication by a mass m_*; a molar energy requires a molar mass M_* in kg/mol. Equal numerical values in several ledgers are possible with declared reference carriers, but those carriers are part of the model. **Author-confirmed convention:** the typed realization above is adopted. It preserves $2\pi O \simeq 383.997935$ and its inverse. The confirmation settles the intended reference assignments; it does not turn the bare dimensionless number 2π into a physical quantity without its carrier.

A3 MFAT wavelength and entropy count correspondence

The selected STO profile fixes the gap-temperature coordinate $T_g = k_{gap}$. It is not selected by equating a bounded-system entropy capacity with an erasure-work count. For the corrected profile specified by the author, $T_g = 66.588452$ K [N26]. Define the thermal wavelength invariant and its gap-branch wavelength by

$$\lambda_k = \frac{c\,h}{k_B \ln 2} = 0.0207571626612\, m\,K\,, \lambda_g = \frac{\lambda_k}{T_g} = 3.11723159764 \times 10^{-4}\, m.$$

Thus $\lambda_g = 0.311723160$ mm, or $311.723160\,\mu$m. This is the wavelength denoted λ_B in the earlier m-point tables. Here T_g is the profile temperature, distinct from the dimensionless fundamental coordinate $k = \sqrt{T_g / T_*}$ in Section 4.1. The fundamental geometric-mean wavelength λ_m is also a different coordinate. Keeping these labels separate preserves the author's equation $\lambda = \lambda_k / k_{gap}$ without exchanging one branch for another.

The corresponding frequency, duration and Anglar are exact algebraic descendants of the selected profile:

$$f_g = \frac{c}{\lambda_g} = \frac{k_B T_g \ln 2}{h}, t_g = \frac{\lambda_g}{c} = \frac{1}{f_g}, \Theta_g = c\,\lambda_g = \frac{\theta_k}{T_g}.$$

Numerically, $f_g = 9.61726610969 \times 10^{11}$ Hz, $t_g = 1.03979653739 \times 10^{-12}$ s, and $\Theta_g = 9.34522522811 \times 10^4\, m^2/s$. The bit-energy coordinate therefore satisfies

$$\epsilon_g = h f_g = \frac{h c}{\lambda_g} = k_B T_g \ln 2\,, N_L = \frac{E}{\epsilon_g} = \frac{E\,\lambda_g}{h c}.$$

The latter is the MFAT energy-equivalent count under the specified bit-energy convention. Its interpretation as a realizable erasure count additionally uses the process assumptions of Landauer's principle; a coordinate identity alone does not assert reversible erasure or an equilibrium entropy measurement.

For a system in the Bekenstein bound's applicable regime, the entropy satisfies $S \le 2\pi k_B E R / (\hbar c)$ [R6]. The upper bound in bits and its relation to the same energy ledger are

$$N_B^{max} = \frac{2\pi E R}{\hbar c \ln 2} = \frac{4\pi^2 E R}{h c \ln 2}, \frac{N_B^{max}}{N_L} = \frac{4\pi^2}{\ln 2}\frac{R}{\lambda_g}.$$

This is the exact normalization dictionary between the two expressions. R denotes the system's enclosing radius; λ_g denotes the wavelength selected by the STO profile. When a comparison explicitly chooses $R = \lambda_g$, it gives

$$N_B^{max} = \frac{4\pi^2}{\ln 2} N_L \simeq 56.95531730\, N_L.$$

The briefing records this factor [N22]. Consequently, a normalized capacity coordinate $(\ln 2 / 4\pi^2) N_B^{max}$ equals N_L for that radius assignment. This rescaling is a comparison of coordinates; the unscaled physical

bound in bits remains N_B^{max}. Equal energy ledgers do not require equality of a maximum entropy bound and an erasure-work count, nor do they imply simultaneous physical saturation.

The source's one-period TASL comparison follows the same dictionary. If $\lambda = c\,\tau$ for the declared duration τ, then

$$T_{TASL}(\tau) = \frac{h}{k_B \ln 2\,\tau}.$$

For $\tau = 1$ s this is $6.92384418 \times 10^{-11}$ K. It is a separate point on the same TASL map, not a replacement for the selected 66.588452 K profile. No alternative temperature is imposed here by equating the two counts. The local accelerated-observer identification used in Section 6 is an additional hypothesis of that conditional horizon construction; it does not redefine the profile temperature or its wavelength.

A4 Identifiability rather than repeated closure

The raw theta-k catalyst contains no water, pressure or gravity input. Its geometric normalization is now author-confirmed in A1 and A2. Treat the eight energy methods as a directed dependency graph, preserving the distinction between that raw construction and later environmental comparison branches. Mark measured inputs, adopted reference carriers, and algebraic descendants. An independent comparison must cross from one branch to an observable not used to choose that branch's references. Propagate a covariance matrix through the map, for example $\Sigma_y = J\,\Sigma_x\,J^T$ at first order. Do not treat outputs sharing the same $c, h, k_B, R,$ water-temperature input, or volume reference as statistically independent confirmations. This is a direct method for turning the source's multi-catalyst analysis into a publishable calibration study.

A5 Established clock charts and the rotation carrier

Let $t_m = \Theta_m / c^2$ be the m-point duration, and let t_* be a declared duration carrier for a geometric comparison. The clock coordinate $q_t = t / t_*$ is dimensionless; the STO rotation period is $P_{LT} = \ell_* t$ and always has dimension LT. A chart factor is not a new physical clock standard.

Clock coordinate	Definition in the comparison chart	Role
M-point	$t_m = \Theta_m / c^2 \simeq 8.480867347 \times 10^{-12}$ s on the raw branch	Thermal Anglar duration
$1/\pi$	$\sqrt{\ell / g} / t_*$ when $\ell / g = t_*^2 / \pi^2$	Incremental square-root comparison
$1/\pi^2$	$\left(\sqrt{\ell / g} / t_*\right)^2$	Squared-clock coordinate; duration is t_* / π^2 only when separately designated as a step
1	$t / t_* = 1$	Unit closure chart
$\sqrt{2}$	$t / t_* = \sqrt{2}$	Declared rotational chart factor; its cube supplies the temporal factor in K2
2	$2\pi\sqrt{\ell / g} / t_* = 2$ in the incremental chart above	Full-period comparison

Clock coordinate	Definition in the comparison chart	Role
4	$\left(2\pi\sqrt{\ell/g}/t_*\right)^2=4$	Squared full-period coordinate; also available as an explicitly declared duration factor

For any selected period coefficient q_t, the pendulum relation is satisfied by $\ell/g=\left(q_t t_*/2\pi\right)^2$. Thus $q_t=\sqrt{2}$ fixes $\ell/g=t_*^2/\left(2\pi^2\right)$, whereas $q_t=2$ fixes $\ell/g=t_*^2/\pi^2$. They are valid related comparison charts; the same fixed ℓ/g is not assigned both values simultaneously. The fall comparison uses $t^2=2d/g$, giving $d/\ell=2\pi^2$ when its duration equals the full pendulum period. These identities recover $2,4,\pi^2,2\pi^2,4\pi^2$ in the stated covariance construction.

Discrete histories are indexed by j with $t_j=t_0+\sum_{i<j}\delta t_i$, where each $\delta t_i>0$ is assigned by the selected clock chart. Refining a numerical integrator need not change a physical tick. The m-point, proper-duration and Euclidean thermal maps are explicit in Sections 4 and 7.1. Global spinor phase returns after two rotational periods in the implemented double cover; the density operator can return after one.

A6 Three-way information partition and the gap coordinate

Adopt one binary information unit with dimensionless entropy $\ln 2$ and equal allocation across three spatial degrees. The unique equal share is $w=\ln 2/3$. This conclusion uses the information and isotropic-allocation premises; it does not import an observed mixing angle.

Use bars for numerical coordinates in the confirmed A1 reference chart, so that square roots and ratios of coordinates are not mistaken for undeclared dimension-changing operations. With $\overline{\theta}_k=6222840.815308866$, define

$$\overline{\Theta}_{part}=\frac{2\sqrt{\overline{\theta}_k}}{w},\ \overline{T}_{avg}=\frac{\overline{\theta}_k}{\overline{\Theta}_{part}}=\frac{w\sqrt{\overline{\theta}_k}}{2},$$

$$\overline{T}_{gap,part}=\frac{\overline{\theta}_k}{\overline{\Theta}_{part}/w}=\frac{w^2\sqrt{\overline{\theta}_k}}{2}.$$

The resulting coordinates are 21593.3555169618, 288.1831316314 K and 66.5844417251 K, respectively. The associated molar reference $RT_{gap,part}\ln 2$ is 383.7358804067 J/mol using $R=N_A k_B$. This branch uses no water, gravity or pressure data. It is distinct from the raw ATCS branch at 66.6521297249 K, the historical reciprocal-CmB corrected branch at approximately 66.588452 K, and the current direct CmB coordinate. Branches are compared without silently replacing their catalyst or reference carriers.

Under a unit change, transform the dimensional quantities and their reference carriers together, leaving barred coordinates fixed. Under a change of reference chart, recompute the chart map. Thus the equality above is an exact consequence of the declared normalization and partition, while its application to a physical mixing measurement has the separate status specified in Section 10.

Appendix B The selected horizon state and its response

B1 Quaternary capacity state

The new notes select a product of maximally entangled interior–exterior pairs with four orthogonal PC10 register states per tile [N10]. Preserve the prime-count semantics: the symbols $00, 10, 01, 11$ represent counts $1, 2, 3, 4$ in the declared codebook. They are not numerical chord lengths and the 00 placeholder does not represent a discarded zero count. Let

$$|\Psi_0\rangle = \bigotimes_{i=1}^{N_t} \left(\frac{1}{2} \sum_{m=1}^{4} |m\rangle_{in,i} |m\rangle_{out,i} \right), \rho_0 = \bigotimes_{i=1}^{N_t} \frac{I_4}{4}.$$

The exterior entropy is exactly $S_0 = N_t k_B \ln 4$. With equal physical scalar areas a_*, $A = N_t a_*$, giving capacity density $\eta_{cap} = k_B \ln 4 / a_*$. Adding an independent saturated tile gives the finite relation $\Delta S_0 = \eta_{cap} \Delta A$. This is a valid selected capacity construction and resolves the earlier absence of a specified boundary state.

The four-dimensional register is distinct from the four tetrahedral pure states of one qubit, whose pairwise squared overlaps are $1/3$. Four such nonorthogonal qubit states cannot constitute an orthonormal four-dimensional basis. A separate two-qubit register or another four-level realization makes the state above well-defined. The correspondence between that register and the existing Bloch preparation map must preserve this distinction.

The physical tiling also remains explicit. The previously verified 384-cell example is a subdivided cube boundary and its spherical projection. The notes describe a 24-cell-derived projection; the projection and area Jacobians for that alternative are to be supplied rather than inferred from the shared number 384. Equal label counts alone do not ensure equal physical tile areas.

B2 Fixed-system entropy variation

For a faithful density matrix define the reduced modular Hamiltonian $K_0 = -\ln \rho_0$. For the selected saturated state, $K_0 = N_t \ln 4 \, I$. A trace-preserving perturbation in the same Hilbert space consequently obeys

$$\delta S = k_B Tr\left(\delta \rho \, K_0 \right) = 0.$$

For one tile and traceless Hermitian X, the more informative expansion is

$$S\left(I_4/4 + \varepsilon X \right) = k_B \ln 4 - 2 k_B \varepsilon^2 Tr\left(X^2 \right) + O\left(\varepsilon^3 \right).$$

Thus varying the state of existing saturated tiles differs from adding saturated tiles. Neither operation is invalid, but they cannot be interchanged in the horizon first law. At finite nonzero β_T, identifying this scalar K_0 with $\beta_T H + \ln Z$ forces H to be scalar on its support. It cannot simultaneously supply a nontrivial energy response on that support.

The full finite bipartite modular operator in the faithful standard representation is $\Delta_{mod} = \rho_{out} \otimes \rho_{in}^{-1}$, up to the identification of the second factor. It is distinct from the reduced K_0. Its flow is trivial for the maximally mixed factors. Naming that flow does not supply a geometric boost generator; the state and its physical action must do so [R14].

B3 A weighted state with an exact finite response

The following extension is proposed for confirmation. Retain the same four prime-count labels, choose energy levels E_m, and replace the equal pair amplitudes by thermal ones:

$$p_m = \frac{e^{-\beta_T E_m}}{Z}, \left|\Psi_\beta\right\rangle = \sum_{m=1}^{4} \sqrt{p_m}\left|m\right\rangle_{in}\left|m\right\rangle_{out}.$$

The exterior state is $\rho_\beta = e^{-\beta_T H}/Z$ and $K_\beta = \beta_T H + \ln Z$. At fixed reference H and T, any normalized infinitesimal state variation satisfies

$$\delta S = k_B \beta_T \delta\langle H\rangle = \frac{\delta\langle H\rangle}{T}.$$

This is a first-order identity. Finite state changes require the full entropy expression; changes in H include work. The notes' $\tau_E = \hbar\beta_T$ is an imaginary-time thermal interval, distinct from the observer's real elapsed time. The horizon observer follows a timelike accelerated worldline, while the horizon generators are null.

An explicit occupation-to-area candidate preserves the prime counts without reducing their symbols. Set $\hat{N}\left|m\right\rangle = m\left|m\right\rangle$ and choose

$$H = \Delta\hat{N} + E_{ref} I, \hat{A} = A_{ref} I + a_* \hat{N}, \Delta > 0.$$

At fixed operators the same first law yields

$$\delta S = \frac{k_B \beta_T \Delta}{a_*} \delta\langle\hat{A}\rangle.$$

This gives an exact finite geometric response once the area assignment is adopted. Selecting $\beta_T \Delta = \ln 4$ reproduces η_{cap} and gives probabilities $(64, 16, 4, 1)/85$. It is an additional spectral matching condition, not a consequence of four labels. The entropy of this weighted state is below $k_B \ln 4$*;* its derivative coefficient can equal the capacity coefficient without its total entropy equaling the saturated entropy. This construction uses variable occupation area and is distinct from the fixed-area-per-register family in B1.

The numerical audit verifies the zero derivative in B2, its negative second-order coefficient, and the equality of the thermal and proposed area responses in B3. It supplies a mathematical completion candidate, not evidence that the current stack already implements this Hamiltonian or area operator.

B4 From the register to the horizon theorem

To complete the physical interpretation, derive the selected spectrum and area operator from the same STO dynamics, identify their generator with the appropriate local boost, and compute the null-area response and heat flux for the same observer. The physical area scale and orientation/refinement behavior must also be specified. With the quaternary response coefficient, $G_{eff} = c^3 a_*/(8\hbar\ln 2)$. Choosing a_* using measured G calibrates that scale; an independently selected a_* would turn the relation into a coupling prediction.

The state selection and finite entropy calculations are recorded. Their physical horizon identification is O2; an operational holographic encoding and recovery claim is O5. A finite bipartite state or MPS representation has its narrower, explicit domain [R9].

Appendix C Quantum dynamics and field completion protocol

C1 Deriving the thermodynamic state comparison

Choose H_0, T_b, Γ_1, and Γ_ϕ before selecting an address. Let the downward and upward transition rates be $\gamma_\downarrow = \Gamma_1(1 - p_{eq})$ and $\gamma_\uparrow = \Gamma_1 p_{eq}$. Their ratio is $e^{-\Delta/(k_B T_b)}$. Use jump operators $\sqrt{\gamma_\downarrow}|g\rangle\langle e|$, $\sqrt{\gamma_\uparrow}|e\rangle\langle g|$, and $\sqrt{\Gamma_\phi/2}\,\sigma_n$. The Lindblad equation then gives the population and coherence formulas in Section 5.

Calculate $\rho_{pre} = E_{\delta t}(\rho_t)$, $\Delta E_{reset} = Tr\left[H_0(\rho_t - \rho_{pre})\right]$, and $\Delta S = S(\rho_t) - S(\rho_{pre})$. The reset free-energy change is $\Delta E_{reset} - T_c \Delta S$. This derives the comparison of the two guides without assuming that visible angular deviation is an energy measurement. For two arbitrary Bloch states, fidelity depends on both directions and radii, so visual overlap alone is not a complete recovery metric.

To connect a threshold multiplier S_{STO} to this model, specify a microscopic interaction H_{int} or a rate function with dimensions and independent coefficients. A photon-frequency rule $f' = S_{STO} f$ gives per-photon energy change $hf(S_{STO} - 1)$; power additionally requires a photon flux. It does not, by itself, determine Γ_1, Γ_ϕ, or qubit holding work. The reviewed code correctly leaves that connection conditional.

Test: freeze the proposed rate law, fit no parameters to the validation sweep, and rotate the state and environment together as a covariance control. Compare pure dephasing, relaxation, and zero-coupling cases. A finite unitarity defect of one Kraus operator is representation-dependent and cannot be the energy observable. With a Hamiltonian supplied, energy and entropy changes are calculable without that identification.

C2 Constructing a field limit

1. Define physical cell adjacency separately from the internal DRC route. Record edge lengths, orientation, lapse, and a causal speed bound.
2. Construct M and K on at least three successively refined geometries. Verify positivity and the desired low-momentum spectrum. Use geometrically consistent weights, not uniform weights on arbitrary long routing edges.
3. Encode a truncated local oscillator algebra. Increase the local cutoff along with spatial refinement and bound the low-energy commutator and propagation errors.
4. Compare two-point functions, dispersion, and stress tensors against a known free field on the same curved background. Verify the appropriate continuum short-distance state condition and renormalization prescription.
5. Introduce interactions with stated counterterms. Show that observables stabilize under refinement and that physical conclusions do not depend on the address gauge.
6. Couple the same renormalized tensor to the horizon response and monitor the covariant conservation residual. Test the low-curvature limit before extrapolating to horizons with strong fluctuations.

This is a construction path available to STO; the refined family and its convergence proof are not present in the current finite Bloch demonstration. Fermions, gauge constraints, and chiral matter require additional algebraic structures beyond this scalar prototype.

The January Yang Mills construction

The supplied Yang–Mills text gives an intended modified Hamiltonian and includes a positive gap among its axioms [N1]. Positivity is therefore conditional in that presentation. The added connection terms require a gauge-consistent completion and coefficients with specified physical dimensions. A finite gap, a classical solution and a continuum quantum existence theorem are different claims [R19].

An STO construction can proceed from gauge links on the address complex, gauge-invariant plaquette interactions and explicitly defined STO fields. Establish a self-adjoint, bounded-below Hamiltonian, construct the physical state space, and report its spectrum with the energy carrier and truncation fixed. Test the gap under changes of volume and approximation. If the discrete structure is fundamental, derive its operational low-energy correspondence; if a continuum Yang–Mills result is claimed, additionally establish the required limit. The collider observable must be connected to the spectrum through an explicit measurement model.

C3 Recovery and holographic claims

Choose an encoding isometry $V : H_L \to H_P$ and a declared error set $\{E_a\}$. For exact correction, test

$$V^\dagger E_a^\dagger E_b V = c_{ab} I_L .$$

This is a concrete criterion for all states in the code space [R12]. For approximate recovery, report entanglement fidelity or a channel-distance bound under a fixed noise model. A state aligned with a noise axis may be robust without encoding arbitrary quantum information. A replay receipt verifies computational provenance, not recovery of an unknown quantum state. These distinctions turn the observed differences between addresses into a useful search for codes rather than a claim inferred from floating-point unitarity residuals.

C4 Control work, coordinate addition and the proposed 15.3 fW scale

The new addition links Bloch preparation to an energy ledger and proposes a holding cost [N15]. A Hamiltonian description already permits a unitary operation to require control work. With $H(t)$ including its chosen control terms,

$$\frac{d}{dt}\langle H \rangle = Tr(\rho \dot{H}) + Tr(H \dot{\rho}).$$

The first term is the prescribed-drive work rate in this convention. For closed unitary evolution generated by $H(t)$, the commutator contribution to the second term vanishes. A dissipative generator can add an exchange term. Thus unitarity and nonzero control work are compatible; no numerical unitarity defect is required to account for that work.

The residual $U^\dagger U - I$ is dimensionless and vanishes for the exact exponential of a Hermitian generator. The approximately 10^{-16} values reported by the demo are numerical consistency residuals. They have neither the units nor the independently measured response needed to serve as a thermal-curvature leakage rate. A deliberately nonunitary effective propagator requires a specified channel and time interval, and the

defect of one Kraus representation is not by itself a heat observable. A native STO dissipation law can instead enter through H_{int}, a completely positive channel or an explicitly calibrated rate in C1.

At a fixed reference carrier, nonnegative additive contributions B_i with $B_{n,i}=\sqrt{B_i}$ obey

$$B_{total}=\sum_i B_i, B_{n,total}=\sqrt{\sum_i B_{n,i}^2}.$$

This exact coordinate identity supports consistent accumulation of the ledger. It does not specify a force, relaxation time or dissipation coefficient. If the contributions are instead coherent amplitudes, interference cross terms require a separate amplitude composition rule. A geometric tension becomes a physical holding model only after its interaction and energy carrier are selected.

For an assumed process dissipating one quantum $\hbar\omega$ per event at rate γ, the correct energy and power bookkeeping is

$$P_{loss}(t)=\hbar\omega(t)\gamma(t), E_{loss}=\int P_{loss}(t)\,dt.$$

Occupancy, detailed balance and control efficiency modify this idealized event model. The integral proposed as power in N15 has units of energy. At $f=5.77$ GHz, one quantum is 3.82324248×10^{-24} J. Producing 15.3 fW in this one-quantum model requires $\gamma=4.00184\times10^{9}\ s^{-1}$. The frequency and bath temperature alone do not supply that rate or establish a lower bound.

In the explicit thermal-reset model of Section 5, a bath at 0.277 K instead gives $p_{eq}=0.269000817$ for the same gap. An equatorial target has $p_t=1/2$, so its continuous reset energy rate is

$$P_{reset}=hf\,\Gamma_1(1/2-p_{eq}).$$

The proposed 15.3 fW value then requires $\Gamma_1=1.73240\times10^{10}\ s^{-1}$, before controller losses and entropy management. These calculated rates expose the missing input rather than select it. The 15.3 fW scale is retained as a conditional test target, not a derived or measured universal minimum. The proposal $q_{ref}=k_B T_{gap}\ln 2$ is an energy carrier; it does not alone set either a gate-work amount or a dissipation rate. Pole/equator cost also depends on the Hamiltonian, bath and target: at finite temperature both pure poles need not have zero holding cost, and pure dephasing can alter fidelity without changing the energy population.

Appendix D Variational identities and finite certificates

D1 Physical scale and entropy response

The selected quaternary state supplies capacity $S=N k_B\ln 4$. Appendix B derives its tile-addition entropy and the zero first-order entropy variation of a fixed saturated tile, then constructs a weighted-state response with a declared area assignment. These are distinct completed calculations. Section 10 records their physical area and horizon identification as one consolidated item.

D2 Current and historical CmB profiles

The current theory uses the direct coordinate $C_{mB}=\sqrt{k\,k_n/\pi}$. The earlier reciprocal subtraction belongs to a historical Bloch calibration profile and is not an unresolved requirement of the current theory. The remaining presentation task is to identify the catalyst, thermal carrier and measured spectral definition for

each reported CmB comparison. The raw branch gives 2.72492984291961; values from other branches must retain their own provenance. This is a version and observable-definition question, not a request to derive an abandoned subtraction.

D3 Occupancy action and covariant balance

The notes now give an explicit scalar potential for the supplied occupancy tensor [N10]. Work with declared normalized covectors r_μ, d_μ, A_μ and scalar coefficients, retaining the physical stress carrier separately. On a non-null sector define $A^2 = g^{\mu\nu} A_\mu A_\nu$ and $A_0^2 > 0$. All these covectors and scalar coefficients are held fixed under the metric variation considered here.

The printed potential has spatial part $-\left(4\pi r^2 + 2\pi r \cdot d\right)/T_L$. Since $\partial\left(r \cdot d\right)/\partial g^{\mu\nu} = r_{(\mu} d_{\nu)}$, its anisotropic stress is $2S_{\mu\nu} + M_{\mu\nu}$. To preserve the specified $O_{\mu\nu} = S_{\mu\nu} + M_{\mu\nu}$, use

$$L_0 = -\frac{2\pi r^2 + \pi r \cdot d}{T_L} - \frac{M}{2F} \ln\left(\frac{\left|A^2\right|}{A_0^2}\right), I_0 = \int d^4x \sqrt{-g}\, L_0.$$

The absolute value permits a real logarithm on either fixed-sign non-null sector and does not define the null sector. Direct differentiation gives

$$-2\frac{\partial L_0}{\partial g^{\mu\nu}} = \frac{4\pi r_\mu r_\nu + \pi\left(r_\mu d_\nu + d_\mu r_\nu\right)}{T_L} + \frac{M}{F}\frac{A_\mu A_\nu}{A^2} = O_{\mu\nu}.$$

Including the volume variation gives $T^{(0)}_{\mu\nu} = O_{\mu\nu} + g_{\mu\nu} L_0$. This establishes a local variational origin of the supplied dyads, with the coefficient repair explicit. Additional metric-dependent carriers or constraints contribute their own variation. The audit checks both the printed and repaired potentials by independent directional finite differences.

For a complete diffeomorphism-invariant matter/occupancy action I, define its Euler derivatives $E_\phi = \left(\sqrt{-g}\right)^{-1} \delta I/\delta\phi$ for scalar fields and $E^\mu_I = \left(\sqrt{-g}\right)^{-1} \delta I/\delta V^I_\mu$ for covectors. The label I here enumerates fields, including r, d, A and an observer covector if present. With the usual variational stress, the exact identity is

$$\nabla_\mu T^\mu_\nu = \sum_\phi E_\phi \nabla_\nu \phi + \sum_I \left[E^\mu_I\left(\nabla_\nu V^I_\mu - \nabla_\mu V^I_\nu\right) - V^I_\nu \nabla_\mu E^\mu_I\right].$$

To derive it, vary the action under a compactly supported coordinate flow ξ^ν: $\delta g^{\mu\nu} = -2\nabla^{(\mu}\xi^{\nu)}$, $\delta\phi = \xi^\nu \nabla_\nu \phi$, and $\delta V_\mu = \xi^\nu \nabla_\nu V_\mu + V_\nu \nabla_\mu \xi^\nu$. Integrate the derivatives of ξ by parts and set its arbitrary coefficient to zero. On all field equations, the right-hand side vanishes. If observer or other fields are prescribed externally, their Euler terms remain exchange terms. Sector currents follow from the chosen couplings and cancel in the closed total account. This implements the observer-inclusive premise without requiring an observer-independent material reservoir.

The identity is a completed balance derivation. For the potential alone, $E^\mu_A = -\left(M/F\right)A^\mu/A^2$, so a nonzero unconstrained stationary field is unavailable at nonzero M/F. Appendix M3 supplies a constrained kinetic completion and includes its stress. The gauge-invariant flux choice is $C_\mu = \nabla_\mu \varphi - q\, A^{em}_\mu$ with the corresponding joint phase transformation. Its physical selection is recorded in O1.

A flux dyad $A_\mu A_\nu / A^2$ made directly from an electromagnetic potential is not gauge invariant under $A_\mu \mapsto A_\mu + \nabla_\mu \chi$. The phase-covector construction in M3 gives an explicit invariant alternative; it does not claim to derive charge from a scalar strain ratio.

The spatial coefficient matrix $(\pi / T_L)\begin{pmatrix} 4 & 1 \\ 1 & 0 \end{pmatrix}$ is indefinite on an unconstrained Euclidean vector space. It remains a valid stress ansatz. The bounded fixed-norm sector in M3 avoids treating it as an unconstrained positive energy form; the physical stability question is assigned to O1.

D4 Existing finite symmetry and operator semantics

The Prime Locks source makes the finite residue grammar explicit [E4]. Excluding multiples of two, three and five from decimal candidate slots yields three four-slot digital-root sequences, 2481, 5724 and 8157. Their distinct ordered subsequences comprise 15 pairs, 12 triples and 3 quadruples. This is an exact candidate grammar; it does not eliminate composite numbers with larger prime factors.

The PC10 encoding starts with prime-count classes: $1 \mapsto 00$, $2 \mapsto 10$, $3 \mapsto 01$ and $4 \mapsto 11$. The symbols then carry geometric values $1, \sqrt{2}, \sqrt{3}, 2$. The symbol 00 consequently represents one, not an empty count. In normalized coordinates the witnesses are the unit-circle area π, square area equal to diagonal at side $\sqrt{2}$, octahedral volume equal to long diagonal at edge $\sqrt{3}$, and triangular area equal to altitude at side 2.

The schema retains each expression's ordered symbols and its two operation signs. Exact substitution into all 52 registered expressions reproduces their outputs [E6]. The census is four Cartan, five null, fifteen TYPE_A, ten TYPE_B and eighteen TYPE_C expressions. The address-and-signature resolver accepts these 52 cases and rejects the remaining 204 of 256 possibilities. Identical operand supports may carry different operations: $(00 + 00) + 00$ evaluates to three, whereas $(00 \times 00) \times 00$ evaluates to one. The earlier chord-only XOR counterexample did not use these operators and is withdrawn.

Proof 7 is already implemented as a junction-base-keyed G2 correspondence [E6]. The supplied certificate reproduces twelve roots, squared-length ratio three, Weyl reflection closure, chirality agreement for all 108 registered K9 sequences, and the recorded partner-Delta-R grading by absolute root height. The chirality involution maps to root negation. The same certificate records that the Delta-R family three-cycle is not a Weyl action, because it changes root-length profiles. That limitation is part of the established result. The older triple-to-root construction and its pulled-back reflections are supplementary coordinate descriptions, not a prerequisite that was absent from the implementation.

The implemented D4 certificate gives normalized squared-distance multiplicities 8, 6, 8 and 1 at distances squared 1, 2, 3 and 4. The separate 576-entry chord inventory counts a protocol budget and is not the 276 unordered vertex pairs. The F4 registry bijects the 48 non-Cartan expressions with 24 long and 24 short roots, under its declared sign and ordering conventions; null expressions have nonzero short-root images. Twelve selected existing G2/D4/F4 test functions pass when invoked directly. The route-action-to-slot bridge retains its source status `DERIVED_CANDIDATE`; it is distinct from the exact expression evaluation and root certificates.

The valid integer closure formula remains $m(N) = 360 / gcd(N, 360)$; it gives 45 for $N = 105664 = 2^6 \cdot 13 \cdot 127$. These finite constructions can enter the paper with their explicit domains, encodings and actions.

These completed checks should not be reopened because a separate physical field limit remains conditional. The symbols encode prime-count classes before their geometric values are assigned. An arbitrary chord-only XOR reduction does not test the implemented algebra. Stronger E8 or spacetime claims should state the additional map and action being asserted, using the existing finite certificates as established input rather than replacing them with cardinality arguments.

D5 Lorentz symmetry and clocks

Appendix A5 fixes the established clock charts. Their ratios are not treated as unspecified. TTDL gives $\sqrt{3/2}$ in its tetrahedral comparison; identifying this value with a Lorentz factor selects $v = c/\sqrt{3}$. The local tetrad and relative-motion map is the corresponding physical comparison in Section 10. Two-way synchronization, spinor double-cover recurrence and fermionic thermal antiperiodicity have the separate explicit maps in A5 and Section 7.1.

D6 Global conservation and finite resolution

Global conservation is adopted in P7 and constructed at the discrete level in M2. Continuous space is retained in P0 and M1. Finite temporal bandwidth limits the resolved mode space; it does not assert a finite set of underlying spatial points. L4 proves the capacity bounds under its occupancy assumptions. The horizon equation's integration constant and a bounded finite spectrum have their stated mathematical roles. The distinct global field, ultraviolet and vacuum-response questions are collected in Section 10.

D7 Status of the reconciliation

The finite identities, source operator certificates, confirmed calibration maps, selected capacity state and repaired potential variation are established at their stated mathematical level. The explicit constrained action, continuous-space embedding and closed discrete dynamics in Appendix M are compatible proposed completions with proofs of their stated finite properties. Section 10 records the remaining physical identifications without reopening those completed results.

Appendix E Empirical audit and prospective experimental protocols

E1 Spectral escape

The source's five-galaxy table is retained below as a report of its values [S012]. It is not relabeled as a new dataset or an independently verified literature comparison.

Object	Source derived escape fraction	Source comparison value	Absolute difference
ESO 338-IG04	6.1%	5.0%	1.1 percentage points
LARS 1	21.4%	12.3%	9.1 percentage points
LARS 2	52.1%	52.1%	0
LARS 5	17.4%	17.4%	0
Haro 11	3.0%	3.0%	0

Repair protocol: attach object-level source citations and apertures; separate observed from dust-corrected H-alpha; propagate line-flux covariance and the Case-B assumption; distinguish a transformed diagnostic from an escape prediction. Freeze the map using one sample and test against an independently

selected sample. If the same line ratio algebraically defines both target and predictor, report the result as an identity check. The 2.04-percentage-point arithmetic average above is descriptive only, because the five comparisons are not established as independent and uniformly corrected.

E2 Galaxy derivation and fixed response comparison

Source chain. The sectional-curvature compendium supplies $K_{cell}=1/(\pi \ell^2)$ and its normalized π^3/g^2 form [S054]. CRC supplies the universal acceleration prescription $a_{STO}=c\,H_0/(2\pi)$ [S028, S035]. The source RAR implementation evaluates that prescription with the external cosmological reference $H_0=67.4\,km\,s^{-1}\,Mpc^{-1}$ [S208]. These are existing source relations, not parameters introduced by the review. The observational coordinate is $g_{obs}=V_{obs}^2/r$; a modeled prediction for it is a separate response map.

The source diagnostic `ntestgal1.py` uses

$$g_{pred}=g_b\left[1+\pi^3\left(g_*/g_b\right)^2\right]^{\beta}$$

and calls an optimizer on $(\log_{10} g_*, \beta)$. Its fitted result is reproduced as a diagnostic of that code path, not as evidence that STO requires two fitted theory constants. Of 175 rotmod files, 171 pass the minimum-five-point cut, leaving 3,375 measurements. D512-2, NGC6789, UGC00634 and UGC07232 are excluded. The fitted values are $\log_{10}\left[g_*/(1\,m\,s^{-2})\right]=-10.668612576$ and $\beta=0.225632829$. The original 78 main, 65 no-transition and 28 lower-bound classifications are recovered. Lower-bound values near 10^{-14} are optimization results, not measurements of an acceleration floor.

Author-confirmed response dictionary with no fitted response parameters. Within this interpolation family, the low-acceleration asymptote is

$$g_{pred}\sim \pi^{3\beta} g_*^{2\beta} g_b^{1-2\beta}.$$

Outside a finite baryonic mass, $g_b=G\,M_b/r^2$, so $v^2=r\,g_{pred}\propto r^{-1+4\beta}$. A nonzero asymptotically constant circular speed therefore fixes $\beta=1/4$. Requiring its coefficient to be the CRC scale fixes $g_*=a_{STO}/\pi^{3/2}$. Substitution gives

$$g_{pred}=g_b\left[1+\left(a_{STO}/g_b\right)^2\right]^{1/4},\quad v_\infty^4=G\,M_b\,a_{STO}.$$

This is a conditional derivation inside the selected interpolation family. The flat-curve asymptote and identification of its coefficient are stated openly; it is not represented as a derivation of the entire response law from sectional curvature alone. The source set contains a second interpolation in `sto_rar_a0.py`. The author's explicit confirmation of E2 now selects the quartic response written above, with a_{STO} as the asymptotic coefficient and $g_*=a_{STO}/\pi^{3/2}$ [N14].

With the recorded external H_0, $a_{STO}=1.0421978813\times10^{-10}\,m\,s^{-2}$ and $g_*=1.8716531819\times10^{-11}\,m\,s^{-2}$. No optimizer or per-galaxy adjustment is used for the following three fixed-response rows.

Response	Parameters fitted to these curves	Original profile RMS dex	Signed gas and 0.5/0.7 profile RMS dex
STO with asymptotic matching	0	0.119078	0.167506
STO with literal $g_* = a_{STO}$	0	0.336008	0.228093
RAR response with fixed a_{STO}	0	0.160780	0.105294
STO diagnostic fitted in each profile	2	0.118104	0.093618

RMS here is weighted log-acceleration RMS using propagated velocity errors only. The original profile squares all gas/disk/bulge velocities and uses unit stellar multipliers. The alternative preserves the signed gas contribution and uses disk/bulge multipliers 0.5/0.7, leaving 3,373 points in 171 galaxies. It is a declared sensitivity profile, not a new fit of those multipliers. The changing ranking shows why a baryonic reference and error model must be fixed before comparing theories.

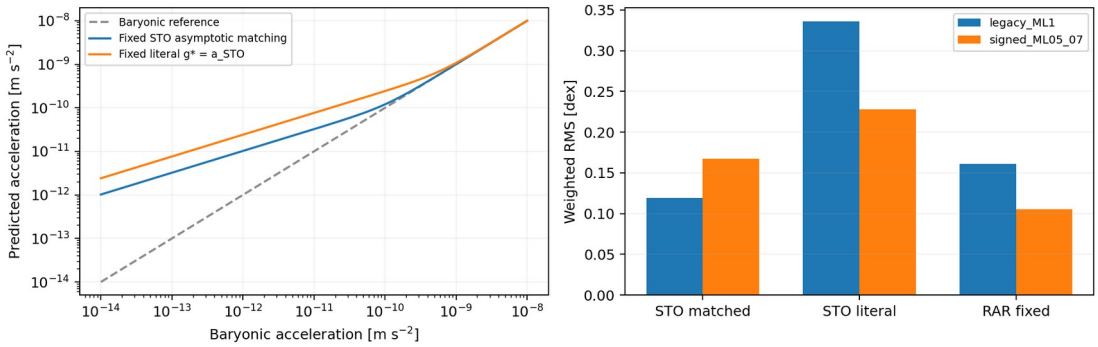

Fixed response curves and their sensitivity to the baryonic reference. All curves in the three fixed-response comparisons use the same external CRC acceleration scale.

The matched fixed STO score is only 0.000974 dex above the two-parameter diagnostic score on the original preprocessing. This is a substantive numerical result, but not a prospective validation on untouched galaxies. A fixed response cannot be credited with the diagnostic fit's galaxy-holdout score. The earlier five-fold grouped fit gave 0.120339 dex for fitted STO, 0.127954 for fitted RAR and 0.112963 for a fitted power law. Their parameter counts and asymptotic behavior differ [E1].

Selection recorded. The response dictionary is settled by the author's confirmation. The new notes also print the exponential RAR expression $g_b / \left[1 - \exp\left(-\sqrt{g_b / a_{STO}}\right)\right]$ immediately after the quartic derivation [N10]. These are different functions. The 0.119078 dex result belongs to the confirmed quartic response; the exponential comparison gives 0.160780 dex on the same original profile. We preserve that distinction and the recorded H_0, rather than transfer a score between formulas. Independently frozen baryonic treatment, uncertainty propagation, lensing and cosmological evolution remain the next physical comparisons.

E3 Transients and gravitational waves

The CRC pulse-width construction may use $\kappa(\ell) = a_{STO} f(\ell) / c^2$ and a dimensionless integral $K = \int \kappa(\ell)\, d\ell$. Here ℓ has length units. For a dimensionless path coordinate s, include $d\ell / ds$ in the

integrand. Defining $1+z=e^{K}$ and $W_{obs}/W_{0}=e^{K}$ establishes their common scaling. Choosing $K=\ln\left(1+z_{input}\right)$ verifies closure; a redshift prediction instead needs a curvature profile obtained independently of that target [S028, S035]. For the source pulse-width code, preserve the distinction between observer-frame duration and already corrected stretch [S205].

The supplied `Grav_finder` archive now fills the earlier source-availability gap [N5]. It contains two scripts, an H1-labeled CSV with 4,096 samples and a 100-row, 56-column Prime Lock comparison table. The H1 time span is GPS 1126259461.8999023 to 1126259462.8996582 with 4,096 Hz sampling. It brackets the GW150914 catalog time, GPS 1126259462.4 [R18]. The strain-column range is about $\left[-2.43,2.55\right]$ and its standard deviation is 0.4313. A normalization, whitening or other processing receipt is needed to connect these values to calibrated detector strain; the filename alone does not establish that connection.

The comparison table has no sample-time column. To printed precision its wave-frequency comparison is exactly $100\,PrimeGap/97$; hydrogen ionization and electron rest-energy columns are respectively $13.6\,PrimeGap/97$ and $0.511\,PrimeGap/97$. These are constructed reference comparisons. Their names do not make them independent detector measurements. The LIGO and Fermi Boolean columns are true for all 100 rows, and the CMS column is false for all rows; the table provides no event-likelihood definition for these flags.

Both scripts shorten the wavelet inputs to the first 100 H1 samples, ending at GPS 1126259461.9240725, about 0.476 s before the catalog event time. The alert entropy and threshold are calculated from the Prime Lock comparison column alone; strain supplies the attached time labels. Holding that column and the time labels fixed while changing strain therefore leaves this alert calculation unchanged, provided execution reaches it. This dependence is visible directly in the code and is not a measured prediction of a future event. The nearest-node and Ridge components use peaks obtained from the same record and do not supply an independent causal forecast test.

The input arithmetic and code dependencies were audited; the original PyWavelets pipeline was not rerun in this review. A separate evaluation of the source spline on the supplied series changed it by only 4.94×10^{-13} RMS, consistent with its extremely small smoothing tolerance on this normalized amplitude scale. No new wavelet detection significance is reported.

Construction path. Retain the actual 24-cell/G2 address semantics, then define a time-indexed prediction map from those states to a detector waveform or residual. Record the H1 processing and calibration, include L1 and off-source controls, and make the predictor causal in time. The same noise realization must not define both the prediction nodes and their validation labels. Pass the physical sampling interval to a frequency interpretation, account for wavelet edge effects, and score false alarms and detection efficiency over multiple held-out events. These steps test the proposed mechanism while retaining its discrete and geometric premises.

Prime Locks report reconciliation. The new historical documents identify the H1 filename, a complex-Morlet CWT approach, lag peaks, shared scales and an entropy-alert proposal [N11–N13]. They materially improve the record of what was investigated. Their calibration and processing provenance is the O4 item. The reported values retain their different meanings:

Reported quantity	Source description	Interpretation retained
Approximately $0.896 - 0.0426\,i$	Wavelet cross-correlation in the constants/gravity notes	Complex association, magnitude about 0.897; estimator and window must be recovered
$-0.1504 - 0.3201\,i$	Later wavelet decomposition in the same notes	Different reported analysis, magnitude about 0.354; not interchangeable with the first
Lags 1963, 2044, 2045, 2046, 2060	GW150914 and Prime Locks comparison	Index offsets until sampling and alignment are specified
Raw correlation around 1025–1065 and -1055	Lag peaks	Unnormalized cross-correlation values, not bounded correlation coefficients or significance
18 shared dominant scales	Complex-Morlet comparison	Scale indices; the printed example list gives 14 entries and needs the full record
0.9996, 1.0 and 0.976	Filament alignment, node matching and entropy timing	The filament comparator is explicitly synthetic; the others need independent labels and causal evaluation

If the reported indices are signed lags about an established zero on the unresampled 4096 Hz strain grid, 2044–2060 corresponds to 0.499023–0.502930 s. That conditional conversion does not establish a predictive lead, and it does not substantiate the separate 13-second claim. For a plotted array index j with zero-lag index j_0, the conversion is $(j - j_0)/f_s$. Interpolation, truncation, padding, the zero-lag origin and the cross-correlation sign convention must be recorded. A raw cross-correlation and a normalized complex coefficient are different statistics. Neither alone gives a false-alarm probability. Peaks of a strain derivative are also not identified astrophysical lensing events without a separate measurement model.

Science-mode provenance. The supplied H1_SCI excerpt describes availability segments. The official GWOSC history download independently contains the enclosing interval $[1126252291, 1126274322)$, which includes the full supplied H1 CSV. Intersecting it with the user's query start 1126259461 gives the supplied first interval and duration 14,861 s [N14, R31, R33]. The query-specific page was not retrievable during this review; the enclosing official history interval was checked instead. A science-mode segment is a timing and operational-status record, not calibrated strain samples, a whitening prescription or a complete event-quality selection. GWOSC publishes strain and its data-quality/injection information separately [R32]. Thus the new link closes a provenance step, while the mapping from those strain files to the normalized CSV remains to be supplied.

Proposed causal prediction statistic. Freeze a lead horizon $\ell > 0$, training events, prime-count encoding, feature windows and predictor before using a held-out event. For a detector strain target $y_{t+\ell}$ in a declared calibrated or invertibly processed representation, compare the same causal baseline with and without the STO features. Let $\hat{y}_0(t+\ell \mid F_t)$ be the baseline and $\hat{y}_1(t+\ell \mid F_t)$ the STO-augmented prediction, where F_t contains only observations available by the declared release time. Define

$$S_{pred} = 1 - \frac{\sum_{t \in T_{test}} w_t \left[y_{t+\ell} - \hat{y}_1(t+\ell \mid F_t) \right]^2}{\sum_{t \in T_{test}} w_t \left[y_{t+\ell} - \hat{y}_0(t+\ell \mid F_t) \right]^2}.$$

Weights and the nonzero-denominator rule are fixed in advance. Positive skill indicates lower held-out squared error than that baseline. A standard two-sided Morlet transform and forward-backward filtering use future samples unless delayed by their full support; they cannot be called real-time predictors without that latency. Fit normalization and whitening on training or past data only. Evaluate uncertainty by held-out events or blocks, include off-source data and surrogate sequences preserving relevant autocorrelation, and correct any search over lags, scales and models. Test H1 and L1 with the same protocol and physical timing treatment.

For an event-alert claim, also report detection efficiency, false alerts per valid observing hour and the lead time of each issued alert using independently supplied event times. A forecast made during an observed inspiral is different from one made before any signal arrives. The previously identified strain-independent entropy alert is a useful ablation control: replacing strain while preserving its timestamps must not leave a claimed strain-sensitive predictor unchanged. This protocol supplies a concrete statistic for confirmation and execution; no value of S_{pred} or prospective alert significance is claimed in this revision.

E4 Collider angles energies and bounded CERN replay

Reproduction achieved. Three updated bounded-replay NPZ exports [N20] contain 1,849,461 stored AK5 track-associated four-vector rows grouped into 40,193 source entries. They restore the low-valued coordinates and source-entry associations missing from the initial reductions. Independent recounting reproduces every available historical AK5 transverse-momentum window, dedicated angular row and transverse-momentum–angle row [N21]. This advances the evidence from checking aggregate arithmetic to replaying the relevant object arrays. It also identifies an upstream interpretation issue: all historical AK5 rows labelled energy, including their joint angular rows, reproduce from pseudorapidity rather than the corrected energy coordinate.

Source and schema. The original ROOT inventory totals 10,824,450,341 bytes across sources 002D3E25, 0080CAE1 and 00FA0A53 [N6]. The updated files retain their declared source basenames and SHA-256 values, four coordinate branch paths and the selection statement `NONE_FULL_UNMODIFIED_SHARD`. These source-file hashes and the assertion of full coverage remain exporter declarations until checked against the original ROOT bytes and entry ranges. The three NPZ byte hashes are independently recomputed in the local audit. The earlier reductions, result archives, run log and audit remain preserved [N16–N19].

Each new file stores four equally sized finite float32 arrays, `flat_pt`, `flat_eta`, `flat_phi` and `flat_e`, plus monotone integer `offsets`, consecutive `event_entry_indices` and JSON provenance. For source entry i, its rows occupy the half-open interval $[offsets_i, offsets_{i+1})$. Every offsets vector starts at zero and ends at the common flat-array length; its length is the number of entries plus one. The entry

indices are unique within each file. Consequently, a declared source hash, original entry index and within-entry row position can identify each exported record. The supplied exporter [N28] iterates entries from the start of the Events tree and appends all four coordinate arrays in common within-entry order. For a successful single-file pass its consecutive counter therefore identifies the source entry. It explicitly retains empty entries. Its three separately named outputs still require the actual per-file invocation record; the default main block stops after its global threshold and writes one file. Separate run/luminosity/event identifiers are useful for cross-file overlap checks but are not necessary to perform this local recount.

Source prefix	Source entries	Stored rows	All-zero rows
002D3E25	11,857	669,753	308,100
0080CAE1	19,774	653,919	293,347
00FA0A53	8,562	525,789	240,695
Total	40,193	1,849,461	842,142

The branch paths identify the AK5 jet extender's `mTracksAtVertexP4` coordinates. The CMS implementation [R40] defines this as the summed four-momentum of tracks associated with each jet at the vertex, using a massless hypothesis for the contributing tracks. It is neither an individual-track measurement nor the complete jet four-momentum. The supplied analyzer counts these records with unit weights. These are stored-row and source-entry counts, not yet cross-file-deduplicated, certified collision-event counts. The exporter writes float32 coordinates; the CMS association type is itself a float-coordinate Lorentz vector.

Energy and selection repairs. The new energy path ends in `fE`, whereas eta ends in `fEta`; the corresponding numerical arrays are distinct. The internal coordinate check $E \geq p_T \cosh \eta$ holds for all rows within a relative tolerance of 10^{-5}, allowing float32 rounding. This check supports consistency of the declared energy coordinate; it does not independently authenticate the ROOT extraction or assign its units. The old `track_leading_e = track_leading_eta` defect is therefore no longer a defect of the current NPZ schema [R34]. The new pT arrays also retain the four target windows and their sidebands. The earlier maximum-pT selection above 5 is no longer an obstacle to this AK5 recount.

Transverse-momentum counts. We use the historical 10% signal half-width around each target t, and sidebands within $t \pm 0.5t$ excluding that signal window. The sideband-to-signal width conversion gives $B = N_{off}/4$. The historical score is

$$z_{code} = \frac{S - B}{\sqrt{S}},$$

with zero returned by the historical implementation when $S = 0$ or $B = 0$. Direct counting of `flat_pt` reproduces all 12 representative signal counts, sideband counts and scores below. Including the duplicate vertex-labelled alias gives 24 matching historical CSV rows. The initial audit's reproduction of all 120 exported score formulas remains a separate, narrower arithmetic result; only the branches included in the updated files have now been recounted.

Source prefix	Target coordinate	Signal count S	Scaled background B	z_{code}
002D3E25	0.133	80	263.75	−20.5439

Source prefix	Target coordinate	Signal count S	Scaled background B	z_{code}
002D3E25	0.215	1,150	848.50	8.8908
002D3E25	0.349	2,320	2,157.25	3.3789
002D3E25	0.430	3,020	2,666.50	6.4326
0080CAE1	0.133	50	275.25	−31.8552
0080CAE1	0.215	1,222	924.75	8.5033
0080CAE1	0.349	2,412	2,297.75	2.3263
0080CAE1	0.430	3,138	2,814.75	5.7705
00FA0A53	0.133	60	202.75	−18.4289
00FA0A53	0.215	785	655.50	4.6221
00FA0A53	0.349	1,851	1,635.50	5.0089
00FA0A53	0.430	2,357	2,024.00	6.8591

The contrasts repeat across the three supplied sources: a deficit at 0.133 relative to this sideband estimator, and positive contrasts at 0.215, 0.349 and 0.430. Their reproducibility is now established for the exported coordinate arrays. The 0080 array length also agrees exactly with the 653,919 rows recorded in the historical run log. The `jet_pt_ak5` and `vertex_pt_ak5` labels point to the same source branch and remain one channel, not independent replications. A transverse-momentum feature requires an explicit response model before it can be interpreted as a predicted invariant mass or continuum Yang–Mills mass gap.

The new offsets permit source-entry counts as well as object counts. For example, the 0080 target at 0.215 contains 1,222 rows drawn from 1,181 source entries. The audit records this distinction for every signal and sideband. The denominator $\sqrt{S}$ omits sideband-estimation uncertainty. Even under an ideal independent Poisson on/off model, the plug-in variance of $S - N_{off}/4$ is $S + N_{off}/16 = S + B/4$, before within-entry correlations, detector response, background shape and search multiplicity. The table therefore retains z_{code} as a descriptive statistic. Recounting it does not by itself calibrate a Gaussian discovery significance.

Historical energy labels resolved. All 24 AK5 energy-window CSV rows reproduce exactly when the same windows are applied to `flat_eta`; none reproduces from `flat_e`. Likewise all 96 historical AK5 energy–angle rows reproduce from eta paired with phi, while none matches the corrected energy–phi calculation. These matches cover both jet and vertex aliases. The supplied original analyzer [N28] explains the failure mechanism: its first-match substring search for `fE` also accepts `fEta`. The supplied packager adds an exact suffix check and separates the fields. The current files therefore establish both the numerical interpretation of the archived rows and a matching source-code mechanism; exact environment and invocation records remain distinct provenance details. Those rows are reclassified as pseudorapidity diagnostics and excluded from energy or invariant-mass evidence.

For transparency, the corrected energy signal counts at the same numerical targets are:

Source prefix	$S_E(0.133)$	$S_E(0.215)$	$S_E(0.349)$	$S_E(0.430)$
002D3E25	0	1	4	4
0080CAE1	0	22	59	88
00FA0A53	0	1	4	3

These are a coordinate diagnostic with the historical window rule, not an assumption that energy and pT probe the same spectrum. For example, at 0.215 the 0080 energy count is 22 with $B=18$ and $z_{code}=0.852803$, whereas its pT count is 1,222. Full corrected counts, sidebands, source-entry support and joint angular summaries accompany the audit. A zero returned by the legacy score rule for an empty signal window must not be interpreted as a calibrated null result.

Angular and joint replay. Using the historical float32 radians-to-degrees conversion, 999 histogram bins spanning $[-180^\circ, 180^\circ]$, and five-degree target windows reproduces all 24 available dedicated AK5 angular rows, including aliases. No attractor or suppressor is flagged in these rows under the historical threshold. Restricting pT to a 5% half-width and using 36 angular bins reproduces all 96 available AK5 pT–angle rows. The two flagged 00FA rows at target 0.133 and angle 110.63° again have mean bin count 3 and score 2.091294; they are the same jet/vertex branch case. They are reproduced local flags, not two independent discoveries. The historical archives contain 108 dedicated angular rows and 268 joint rows across all channels, but the AK7, calorimeter, trigger and other unavailable branches have not been independently recounted here.

Two analysis choices now have a concrete repair path. First, 842,142 rows, about 45.5% of the exported collection, have all four coordinates equal to zero. We retain them to reproduce the historical result. The CMS collection initializes its summary four-vector to zero, and the track-summing routine also returns zero for an empty association [R40]. These rows cannot establish a preferred physical direction from their stored phi value. Association-count/status fields would distinguish empty from unavailable summaries; a separately declared nonzero-vector analysis is already possible with the current export. Their concentration at phi zero affects the global histogram mean and standard deviation used by the angular score. A prospective test must declare a validity mask and background model before interpreting that score. Second, the dedicated comparison uses absolute differences on a $[-180^\circ, 180^\circ]$ histogram, so the declared 216°, 270° and 324° targets lie outside the evaluated interval. The historic output therefore tests four of the seven listed angles. A complete periodic test should wrap both targets and angular differences, with its revised outcomes reported separately from this faithful replay.

Method and figure provenance. The 0080 log reports another mass-gap analysis with scores 0.84 at 0.215, −4.50 at 0.133, −0.68 at 0.349 and 0.52 at 0.430 [N18]. Those log values have not been newly regenerated by the present recount and must not be assigned to corrected energy solely because a number is similar. Their different counts and background estimates remain a reason to specify one frozen analysis. Repeated log blocks are not independent experiments. The prior figure audit also remains applicable: 13 PNG content hashes recur across all three archives, while an earlier source routine contains seeded random annotations, a hard-coded angular annotation and an absolute-score sum [E2, N19]. The supplied original program [N28] specifically assigns seeded random values between 3 and 5 in `generate_energy_quantization_figure()` whenever a selected window is nonempty. Its correlation figure also applies a nonlinear display transform and has a synthetic fallback. These publication displays remain outside empirical evidence; none is used as a calibrated significance or correlation measurement

here. Their limitations do not undo the array-level pT reproduction. The new audit reads only the supplied arrays and tables; it never imports the historical analyzer or invokes its synthetic-data fallback.

Prediction chronology and completion path. The January-source Yang–Mills text declares 7.5-degree and 54-degree targets and gap values 0.215, 0.212 and 0.210 GeV [N1]. Its recorded creation and modification dates support the author's chronology, with authenticated version history still useful for priority attribution. The separate 720–810 GeV proposal remains a hypothesis; the historical 750 GeV excess was not reproduced in the ATLAS 2016 data [R20].

The current bounded AK5 replay is complete for the specified historical pT and angular calculations. The request for readable, low-valued, associated coordinates and the original analyzer/exporter is met. A fresh recount against the resupplied files reproduces the same results [N29]. CERN record 6025 independently lists all three ROOT basenames, byte sizes and Adler-32 checksums [R39]. These metadata establish source-file identity in the public index; the full local ROOT bytes have not been independently checksum-verified here. The source dataset is VBF1Parked Run2012B AOD, selected for high-pT dijets, large dijet mass and angular separation, which must enter the detector/selection response model.

The packager checks its 5,000-entry target only after a full chunk, so the threshold is not an exact entry cap. Its default main block creates one export, whereas three named exports were supplied. Run/luminosity/event identifiers and the CERN record's validated-run selection are not exported. This documents the scope of the bounded recount. Section 10 specifies the compact metadata and statistical validation needed for the physical claim; no further unspecified CERN data package is requested.

E5 Laboratory protocols for prospective registration

The new addition supplies two laboratory proposals linked to EMI and the helical ledger [N15, S292, S021]. Their value is to make the claimed response testable without relying on cosmological or collider inference. They are protocols proposed for registration: no external registry record, locked analysis hash or completed experiment accompanies this submission. Before data collection, fix the physical regime, effect size, nuisance calibration, sample size, stopping rule and rejection statistic. A null result should be capable of excluding a specified STO response, not merely lack an unexplained feature.

E5.1 Deuteron relaxation under planar confinement

The proposed comparison is between isotropic deuterated water and independently verified planar ordering in a confined water sample. Graphene-oxide confinement is a suggested preparation method, not by itself proof of square-ice structure or a two-dimensional dynamical regime. Geometry, hydration, temperature, quadrupolar coupling and surface interactions must be measured.

For the applicable spin-1 quadrupolar relaxation model, write the transverse rate as

$$R_2 = C_Q\left[3\,J(0) + 5\,J(\omega_0) + 2\,J(2\omega_0)\right],$$

where C_Q includes the quadrupolar prefactor and J is the spectral density. This $3:5:2$ combination already occurs in spin-1 relaxation theory; the original multiple-rate experiment gives the equivalent $9:15:6$ expression with a correspondingly smaller prefactor [R35]. Its occurrence is a compatibility point. The new STO hypothesis is the specific change $3 \to 2$ in the zero-frequency coefficient under a defined confinement transition, while the other two coefficients retain their values [N15]. That change is not supplied as a consequence of the standard formula.

Introduce a response parameter w_0 and test

$$R_2 = C_Q\left[w_0 J(0) + 5J(\omega_0) + 2J(2\omega_0)\right], w_0^{isotropic} = 3, w_0^{planar} = 2.$$

At matched C_Q and spectral densities, the predicted change is $-C_Q J(0)$, and the rate ratio is

$$\frac{R_2^{planar}}{R_2^{isotropic}} = 1 - \frac{J(0)}{3J(0) + 5J(\omega_0) + 2J(2\omega_0)}.$$

It is 0.9 when the three spectral densities are equal, and approaches $2/3$ only when the zero-frequency term dominates. Thus a coefficient change cannot be tested by demanding a universal two-thirds rate ratio. Confinement can change J, C_Q and the form of the relaxation model itself. An anisotropic spectral-density tensor may be needed; the scalar formula's applicability must be established first.

A constructive test would use several independently measured relaxation modes and fields to constrain spectral response, reserve R_2 for validation, and estimate

$$\hat{w}_0 = \frac{R_2/C_Q - 5J(\omega_0) - 2J(2\omega_0)}{J(0)}, J(0) > 0.$$

The auxiliary-mode equations must be declared under both hypotheses; assuming they are unchanged is itself part of the proposed test model. Fit no spectral density to the reserved R_2 measurement. Compare a predeclared discrete-transition model against ordinary anisotropic relaxation and a continuous-response alternative, propagating calibration uncertainty. If confirmed planar samples with sufficient precision retain $w_0 = 3$ and exclude 2, that rejects this specified STO channel-jump hypothesis. A continuous transition rejects its discontinuity claim only after finite-size effects, phase coexistence and the measurement resolution have been bounded. A single changed relaxation rate cannot identify a changed channel weight.

E5.2 Rotating resonator and the helical response

For a system with helical symmetry generated by $\xi = \partial_t + \Omega\partial_\phi$, the charge $Q_\Omega = E - \Omega J$ is the corresponding energy–angular-momentum combination [S021]. Conservation under that symmetry does not by itself fix a measured frequency drift. The new proposal adds the response law

$$\delta f = f_0\left[\exp\left(\alpha_\Omega \frac{\Omega J}{E}\right) - 1\right],$$

where α_Ω is a dimensionless response coefficient, distinct from the electromagnetic fine-structure constant. Its value and the definitions of the measured mode energy E and angular momentum J must be supplied independently of the drift being tested. The condition $\delta\phi \le 10^{-3}$ rad is retained as a proposed phase-lock quality cut, with a specified measurement bandwidth and exclusion rule.

A useful conditional consequence follows for an ideal mode of frequency $\omega = 2\pi f_0$, azimuthal index m and occupancy N, if $E = N\hbar\omega$ and $J = N m\hbar$. Then

$$\delta f = \frac{\alpha_\Omega m \Omega}{2\pi} + \frac{\alpha_\Omega^2 m^2 \Omega^2}{4\pi\omega} + O(\Omega^3).$$

The leading term is linear in rotation and can be degenerate with an ordinary rotational optical response. It therefore cannot be isolated merely by observing a drift. Reverse Ω, compare counterpropagating modes, measure thermal and centrifugal changes, and calibrate Sagnac, refractive and mechanical terms on independent runs. The even-in-Ω residual is a possible additional target of this particular exponential completion, but ordinary even-in-rotation effects also require controls. For a dispersive material resonator the mode-energy and angular-momentum assignments require explicit justification before using this expansion.

Register the residual likelihood after the conventional device model, a nonzero predicted α_{Ω} or an independently bounded interval, and sensitivity sufficient to distinguish that prediction. Residuals compatible with zero can exclude the specified additional response at that sensitivity. They do not disprove Noether conservation, which may already be satisfied by the baseline. This separates the exact conserved ledger, the proposed STO constitutive law and its measurable discriminant.

Appendix F Source provenance and revision decisions

F1 Source hierarchy

The revised EMI and ATCS–TTDL documents, the two primary axiom texts, and the September working proof are the primary theory sources. The reconciliation PDF supplies the requested scope, but a claim in it is not treated as stronger evidence than its underlying derivation or code. The bridge deep dive supplies several explicit cautions and construction requirements already consistent with the present approach. The source archive and the current stack snapshot are separately identified; no external publication status is inferred for the private source files.

Source identifiers	Document or implementation	Use in this draft
S292	Axiom EMI STO Relativistic Thermodynamics and Mass Genesis, revised DOCX	Horizon argument, MFAT, laboratory protocols
S293	Axiom DE 04 Unifying ATCS and TTDL, revised DOCX	Capacity and volume relation
S294 and S295	Axiom DE 02 ATCS; Axiom DE 03 TTDL	Adopted geometric premises
S296	Dim Emergence Working Proof, 22 September source	Operational labels and eight-method energy assessment
S297	QFT Relativity Reconciliation Model PDF	Scope and proposed throughline
S301 and S302	sto-prime-bloch; STO Bloch Bridge Deep Dive	24-cell, tetrahedral states, dimensional and horizon requirements
S004 and S024	TASL1; STO3 Unifying Gravity and Thermodynamics	Thermal coordinates and physical hypotheses
S021	HTF3 Noether theorem and redshifting energy	Helical ledger and resonator tests
S039 and S041	Covariant Cancellation; Dual Geodesics and Curvature Gap	Clock normalization and admissible versus metric paths

Source identifiers	Document or implementation	Use in this draft
S049, S054, S068	Chiral Stress Tensor and sectional-curvature formalisms	Candidate constitutive completion
S089	Unified Metaplectic Architecture	Higher-dimensional symmetry program
S012	TASL5 Spectral Geometry of Ly-alpha Escape	Reported five-object comparison
S028, S029, S035	CRC1; Unified STO Framework; Supernova Pulse Width	Reported astrophysical claims and predictions
S199, S205, S208, S225	Galaxy fitting, transient width, RAR, and CERN scripts	Static audit of analysis pathways
Current stack snapshot	Bloch projection, Hopf bridge, calibration, controller, thermodynamics	Reproduced finite implementation results
E1–E6	Galaxy archive, collider exports, metrological ledger, Prime Locks and certified stack	Prior evidence reconciliation incorporated
N1–N4	January-source Yang–Mills DOCX and three STO Works addenda	Chronology, atomic and spectral constructions
N5 and N6	Grav finder archive and CERN Drive source inventory	Observational provenance and bounded reproduction status
N7 and N8	STO quick calculator and hexagram–pi analyzer	October arithmetic, reference ratios and finite address audit
N9 and R21–R30	Eight supplied encyclopedia PDFs and their primary or author sources	Thermal, phase, Clifford and hydraulic correspondences
N10	New STO notes	Selected quaternary horizon state, action, fluid and metric proposals
N11–N13	Three Prime Locks historical documents	Reported GW analyses and forecasting proposals
N14 and R31–R33	Author decisions and GWOSC records	Confirmations, authorship and science-mode provenance
N15	Manuscript additions	Horizon completion, metrology boundary, holding-power and laboratory proposals
N16–N18	Initial reductions, result ZIPs and run log	Preserved export history, reference counts and method sensitivity
N19 and R34–R35	Initial audit and coordinate/relaxation references	Historical export diagnosis and laboratory baseline
N20–N21	Bounded AK5 exports and independent recount	Associated pT/angular replay, corrected energy and historical eta identification

Source identifiers	Document or implementation	Use in this draft
N22–N26	HTF working proof, briefing, author clarifications and coordinate audit	Wavenumber replacement, spectral reconstruction, material response and corrected MFAT attribution
N27–N29	Time Manifold, CERN programs and audit	Closure constructions and provenance completion

The source bundle contains the complete extracted-source manifest with file names and SHA-256 hashes, the verification script and results, and the hashes of the eight stack modules directly recorded for reproduction. A source identifier names an archived input; it is not a journal citation. Original source files are not modified by this analysis.

F2 Confirmed methods and revision record

A1 and A2 are author-confirmed. The galaxy response in E2 and the number-weighted nuclear operator in G1 are confirmed. G2 and PC10 retain their finite certificates and prime-count symbol semantics; the earlier chord-only counterexample is withdrawn. The raw catalyst is not water-calibrated. The direct CmB coordinate supersedes the historical subtractive prescription as the current profile, while historical profile values remain labeled where used.

The supplied horizon notes select a quaternary capacity state and an occupancy potential. B and D3 retain their mathematical reconstructions. The bounded CERN arrays, original analyzer, exporter and public source inventory establish the available local replay and distinguish the energy and eta fields. The original ROOT data are not requested again. The Time Manifold, HTF, Prime Locks and January Yang–Mills sources are preserved with their existing provenance.

The 26 October clarification fixes the STO rotation-period type as LT, gives the HTF divisor deconstruction and the three-way information partition, and explicitly states continuous space, discrete geometric time and global energy conservation [N30]. A5–A6 and M construct those updates. N31 supplies fresh execution of the current stack and exact arithmetic checks. All outstanding author decisions, physical correspondences, empirical validations and submission details are now located only in Section 10.

Appendix G Atomic and spectral constructions

G1 Reconstructing the nuclear radius calculation

The 24-vertex addendum states a static dual radius ratio $\sqrt{2}$, a TTDL projection by $\sqrt{3/2}$, 82 core neutrons, 44 excess neutrons and proton reference radius $R_p = 5.50$ fm for lead-208 [N2]. Their projected outer-neutron factor is

$$f_{out} = \frac{\sqrt{2}}{\sqrt{3/2}} = \sqrt{4/3}.$$

The displayed outer radius is therefore 6.350853 fm. Subtracting R_p directly gives 0.850853 fm, so an outer-envelope radius cannot be the stated total-neutron RMS radius. A number-weighted mean-square construction fills the missing step:

$$R_n^2 = \frac{82\,R_p^2 + 44\left(f_{out}R_p\right)^2}{126},\ \Delta R_{np} = R_p\left[\sqrt{\frac{82+44\,f_{out}^2}{126}} - 1\right].$$

It gives $R_n = 5.811296$ fm and $\Delta R_{np} = 0.311296$ fm, recovering the addendum's 0.311 fm. With the unprojected factor $\sqrt{2}$, the same averaging gives 0.888544 fm, recovering its approximately 0.89 fm static comparison. Both matches arise from the stated counts and radius, with no parameter optimized in this reconstruction.

Author-confirmed operator. The author has confirmed this reconstruction [N14], so the number-weighted RMS expression is now adopted as the intended measurement operator. The equation was reconstructed during reconciliation and subsequently confirmed; it is not retroactively attributed as a printed equation in the original addendum. The averaging is exact if the populations have the stated mean-square radii. The model assumes the core-neutron RMS radius equals the chosen proton reference and assigns the excess-neutron mean-square radius by the geometric factor. A density-profile treatment and consistent point-proton versus charge-radius convention would test those assumptions. The 0.311296 fm result lies within the PREX combined result 0.283 ± 0.071 fm [R17]; model and radius-reference uncertainty have not been included.

For a nucleus with $N \geq Z$, this particular completion generalizes to

$$\Delta R_{np} = R_p\left[\sqrt{1 + \frac{N-Z}{3\,N}} - 1\right].$$

This is a candidate transfer test: fix the radius convention and geometric assignment before evaluating other isotopes. It is not a claim that the same two-population approximation applies without correction throughout the nuclear chart.

The orbital and binding-energy work also retains its stated scope. Its shell study scans gate amplitude $\varepsilon \in \{0.4, 0.5, 0.6\}$ against known closures and reports 0.5 as favorable. The companion energy-proxy code uses global coefficients 15.8, 18.3, 0.71 and 23.0, plus a radius scale 1.2. Therefore the absence of per-nuclide tuning should be preserved without relabeling the calculation as a constants-only prediction. A fixed global model can still make useful isotope-level predictions when evaluated without changing those inputs.

G2 Hydrogen spectral coordinates

The spectral addendum's central map reduces exactly to

$$\Theta = \frac{c^2}{f},\ T_E = \frac{\theta_k}{\Theta} = \frac{hf}{k_B \ln 2},\ m_E = \frac{h}{\Theta} = \frac{hf}{c^2}.$$

It consistently maps photon frequency to Anglar, energy-equivalent temperature and mass-equivalent coordinates [N3]. The following values use the addendum's supplied frequencies, not a new fit of line positions.

Line	Frequency Hz	Energy equivalent temperature K
Hyperfine	1.420406×10^{9}	0.098347
H alpha	4.570000×10^{14}	31641.968
H beta	6.170000×10^{14}	42720.119
Lyman alpha	2.470000×10^{15}	171018.951

For any two lines, $T_{E,i}/T_{E,j}=f_i/f_j$. Consequently these coordinates cannot all become a common ambient temperature merely by averaging them when their frequencies differ. An excitation, population or radiative-transfer operator connects the energy coordinate to environmental temperature. Distinct transitions can arise in one environment. The exact coordinate map is retained; ambient thermometry is a separate proposed application under O3.

The coefficient $w=\ln 2/3$ follows from the opening information premise and equal partition across three spatial degrees: $s_1+s_2+s_3=\ln 2$, with $s_1=s_2=s_3$, implies $s_i=w=0.231049060186648$. This is a derivation conditional on those premises, not a fitted numerical coincidence. Appendix A6 carries it through to the TASL gap coordinate without water, pressure or gravity as inputs. Its proposed interpretation as a weak-mixing observable is a distinct correspondence: declaring $w=\sin^2\theta_W$ specifies a map, whereas calling w an angle specifies another. The physical observable and comparison convention belong to the single validation register in Section 10; they do not invalidate the geometric derivation.

G3 What these additions contribute

The nuclear reconstruction demonstrates a source-inferable missing measurement operator: an envelope and an RMS radius are different observables, and the stated occupancy fractions connect them. The hydrogen reduction demonstrates a fully specified algebraic coordinate map and identifies the additional environmental operator required for thermometry. Both advance the reconciliation by making the observable map explicit. Neither requires a globally flat spacetime premise or a rejection of STO's geometric starting point.

Appendix H Thermal periodicity and hydraulic reconciliation

H1 Exact thermal and informational conversion

The identity in Section 4.4 follows by dividing $\Theta=c^2h/\left(k_BT\ln 2\right)$ by c^2h. It is independent of a water or acceleration reference. At fixed positive T, one binary entropy unit has the reversible heat scale $k_BT\ln 2$. Assigning that scale to a physical process requires its state change and thermodynamic conditions. For a canonical state, the exact expression is $S_{bits}=\left[\beta_T\langle H\rangle+\ln Z\right]/\ln 2$, which retains the partition-function term.

In the confirmed chart, let $\overline{E}_0=\left(2/3\right)\overline{\Theta}_k/10800$ and $\overline{T}_g=\overline{E}_0/\left(\overline{R}\ln 2\right)$. Eliminating the catalyst gives

$$\overline{\Theta}_B=\frac{\overline{\Theta}_k}{\overline{T}_g}=10800\,\frac{3}{2}\,\overline{R}\ln 2,\sqrt{\frac{\overline{\Theta}_B}{10800}}=\sqrt{\frac{3}{2}}\sqrt{\overline{R}\ln 2}.$$

The bars denote numerical coordinates relative to the carriers of A1–A2 and Section 4.2. They prevent an equality of chart coefficients from being mistaken for an SI dimensional equality between Anglar and molar entropy. The source's $n_{\theta B}=2.940190382010316$ follows exactly in that chart.

For decimal gigabytes, $1\,GB=8\times10^{9}$ bits. Define the conversion coefficient

$$C_{GB}=\frac{1}{(8\times10^{9})k_B\ln 2}=1.30617470559947\times10^{13}\,GB\,K/J.$$

The coldness in GB/J is C_{GB}/T. The submitted expression divides E_{mol} by $k_B\ln 2\,T_g(8\times10^{9})(R\ln 2)$; substituting $E_{mol}=RT_g\ln 2$ reduces it to C_{GB}. Consequently its approximately $13,061,747,055,940$ value is a conversion coefficient, not the coldness at the gap temperature. At $T_g=66.6521297248721$ K the result is 195.968937675529 GB/nJ. The fully consistent coefficient is $13,061.7470559947$ GB K/nJ. The difference from the literal submitted integer is explained by the rounded inputs.

Quantity	Recomputed value	Interpretation
C_k	384.125976253634	Dimensionless catalyst coefficient
T_g	66.6521297248721 K	Selected molar thermal coordinate
$R\ln 2$	$5.76314632164398\,J\,mol^{-1}K^{-1}$	Molar binary entropy scale
$\beta_T(T_g)$	$1.08668253301696\times10^{21}\,J^{-1}$	Inverse thermal energy
$\beta_{bit}(T_g)$	$1.56775150140423\times10^{21}$ bit/J	Entropy slope in bits
$n_{\theta B}$	2.940190382010316	Normalized TTDL–thermal identity

A useful finite check sets a two-level gap to $\Delta=k_BT\ln 2$. Then the excited-to-ground equilibrium probability ratio is $1/2$, the excited population is $1/3$, and the entropy is $-2/3\log_2(2/3)-1/3\log_2(1/3)=0.91829583405449$ bits. This verifies the thermal operator and illustrates why a one-bit energy scale need not mean a one-bit state entropy. The audit also checks invariance under a constant Hamiltonian shift.

DR spectral coordinates must retain their calibration profile. For example, the supplied 771.1 THz carrier gives $B_\gamma=801.021103264431$ in the raw catalyst profile. The source's tabulated 801.32 belongs to a different reference precision or profile; it is retained as source data rather than silently substituted for the raw calculation. The frequency, temperature profile and bit convention should travel together in a receipt.

H2 Head height and the full comparison span

Use the specific-energy carrier of A2 and set $\epsilon=C_k(1\,m^2/s^2)$ and $t_*=1$ s for this numerical illustration. Define

$$t=2t_*,\ g=\frac{\sqrt{\epsilon}}{2t_*},\ d=t_*\sqrt{\epsilon},\ L=2d,\ \ell=\frac{d}{2\pi^2}.$$

These definitions give $g = 9.79956601403\, m/s^2$, $d = 19.5991320281$ m, $L = 39.1982640561$ m and $\ell = 0.992903627723$ m. Substitution in the fall and small-amplitude pendulum formulas gives 2 s for each. It also gives $gL = 384.125976253634\, J/kg$ and $gd = 192.062988126817\, J/kg$. These are the full-span and single-fall references respectively, not the same energy counted twice.

The velocity at the end of the fall is $v = gt = \sqrt{\epsilon}$. Thus the proposed head quotient is $v^2/(2dg) = 1$. The parentheses matter: the intended denominator is $2dg$. All five ratios in Section 3.2 then follow. Replacing meters and seconds by another coherent system changes the numerical values of the quantities and their carriers together, leaving the ratios invariant. Reassigning the physical clock or energy carrier defines a new comparison experiment. This construction preserves the source's unit-agnostic aim while stating exactly how a reported acceleration is obtained.

H3 Phase sectors and the common thermal operator

To make the phase analogy constructive, begin with an internal state space H_{int} carrying the accepted address and operator data. Adjoin a cyclic closure register with orthonormal states $|n\rangle$, $n = 0, \ldots, N-1$, and a unitary shift $S|n\rangle = |n+1 \bmod N\rangle$. For $\chi_m = 2\pi m/N$,

$$|\chi_m\rangle = \frac{1}{\sqrt{N}} \sum_{n=0}^{N-1} e^{in\chi_m} |n\rangle, S|\chi_m\rangle = e^{-i\chi_m} |\chi_m\rangle.$$

The spectral theorem therefore decomposes any Hamiltonian commuting with S into phase sectors. One explicit proposed Hamiltonian is

$$H = H_{int} \otimes I - J\, I \otimes (S + S^\dagger), E_{j,m} = \varepsilon_j - 2J \cos \chi_m,$$

where J is a declared energy and ε_j an eigenvalue of H_{int}. Its probabilities are determined by the same TASL map:

$$p_{j,m} = Z^{-1} 2^{-\Theta E_{j,m}/(c^2 h)}.$$

This proves the existence of a finite model combining address states, a repeated-closure phase and thermal weights. It does not determine J, the internal spectrum, or whether the real AxiomARC routing action has the required symmetry. The supplied receipt and boundary schema should supply those operators in the next implementation comparison. In an infinite integer register, the Fourier states are generalized states; physical vectors use square-integrable wave packets. The cyclic construction keeps the finite audit normalized and explicit.

The theta-vacuum literature supplies an integer winding action for suitable gauge transformations, with the phase labeling a sector [R24–R26]. Identifying the construction above with that situation requires a gauge field, its constraints, a winding observable and a physical state space. The displayed cosine spectrum is exact for this chosen hopping model; it is not asserted as the exact strongly interacting Yang–Mills vacuum spectrum. Nor does a common integer action identify spatial translation with gauge redundancy. A curved base manifold can support an internal closure register without acquiring a global translation symmetry.

The thermal scale also has a precise periodic interpretation. From $\tau_E = \hbar \beta_T$ and TASL,

$$\Theta = \frac{2\pi c^2}{\ln 2}\tau_E, \frac{t_B}{\tau_E(T_g)} = \frac{2\pi}{\ln 2}.$$

Bosonic periodicity and fermionic antiperiodicity in a thermal path integral refer to this imaginary-time interval [R27]. Spinor sign under a spatial 2π rotation and STO real-clock closure are separate operations. Testing their proposed identification requires an explicit representation and clock observable, rather than equating their periods numerically. The audit verifies the common-Hamiltonian matrix identities; it does not claim a new thermal-field or hardware simulation.

H4 Bott periodicity and binary sequencing

For the convention $e_i^2 = -1$, the real Clifford algebras $Cl_{0,n}$ at $n = 0, \ldots, 7$ are respectively

$$\mathbb{R}, \mathbb{C}, H, H \oplus H, M_2(H), M_4(\mathbb{C}), M_8(\mathbb{R}), M_8(\mathbb{R}) \oplus M_8(\mathbb{R}).$$

The algebraic recurrence is $Cl_{0,n+8} \simeq Cl_{0,n} \otimes M_{16}(\mathbb{R})$; the matrix-size multiplier is 16 and the real algebra-dimension multiplier is 256. The complex recurrence is twofold. Graded modules connect these algebraic results to Bott periodicity [R23]. The supplied article's lower clock uses I Ching trigrams as labels for a mod-eight mnemonic [N9]. This shows an established use of binary notation in the presentation, without establishing that the PC10 encoding is the same representation.

The appropriate comparison begins with the actual source operators. Preserve the order prime-count class, binary symbol, geometric witness, registered expression. Seek a map Φ into endomorphisms of a declared real or complex state space, with generators obeying

$$\Phi(e_i)\Phi(e_j) + \Phi(e_j)\Phi(e_i) = 2\eta_{ij} I.$$

Record the signature η, the field, the grading, and the action on address states. Then verify closure, products, and the extension implementing the periodic recurrence. These are operator tests, not tests of whether an address set has 8 or 64 elements. The existing G2/D4/F4 certificates remain established inputs; the new question is how, if at all, the desired Clifford action is represented by that stack. There is no inference from mod-eight classification to eight physical time steps without an additional dynamical map.

H5 A constitutive calculation from occupancy fluctuations

For a finite classical occupancy model at fixed T and particle number, assign state i energy E_i, volume $V_i > 0$ and degeneracy g_i. Define

$$Z(T, p) = \sum_i g_i \exp\left[-\beta_T (E_i + p V_i)\right].$$

Assume these assigned energies, volumes and degeneracies have no additional pressure dependence. Differentiation gives $\partial_p \ln Z = -\beta_T \langle V \rangle$ and $\partial_p \langle V \rangle = -\beta_T Var(V)$. Thus Section 8.2 follows. The same relation is a standard isothermal–isobaric fluctuation identity [R30]; the STO contribution proposed here is the occupancy assignment and its TASL expression. If quantum H and V do not commute, the derivative uses the corresponding imaginary-time or Kubo covariance, not an unqualified ordinary variance.

The specific-storage analogy further distinguishes types. For an appropriate linear saturated medium, storage has the form $S_s = \rho g(\alpha_s + n\kappa_f)$, where α_s is a skeletal compressibility, n porosity and κ_f fluid compressibility [R29, N9]. Its dimension is inverse length. The letter beta used for compressibility in some hydraulic sources is distinct from β_T, whose dimension is inverse energy. Neither is the dimensionless compression coefficient k_c.

For a specified occupancy assignment, the construction proceeds by inserting its E_i, V_i, g_i and stress coupling into the partition function and differentiating. Tensor strain uses the free energy as a function of metric or strain. Appendix M supplies a candidate finite energy spectrum and variational stress; O1 and O3 record their physical assignment and comparison. This preserves the exact fluctuation identity without turning the hydraulic analogy into an unproved electromagnetic coupling.

H6 Reproducible finite audit

The two supplied modules are archived unchanged [N7, N8]. The new audit evaluates their declared inputs and selected functions; it does not rerun the separate full prime benchmark, the previous application test suite, or detector pipelines. It records source hashes and extraction scope.

Check	Result	Meaning
DRC assemblies	6,384 sequences in 64 addresses	Within-assembly transitions follow the source candidate rules
Assembly depths	Minimum 3; maximum 507 at `101010`	Number of source sequences associated with each address
Binary pi prefix	240,000 fractional bits; six-bit nonoverlapping blocks	Fixed deterministic input and block convention
First coverage	All 64 addresses first present at block 244	Measured on the untruncated prefix
Independent prefix check	First 1,464 bits agree between Machin and Gauss–Legendre calculations	Cross-check of the coverage input
Last occurrence quota	`101010` reaches 507 occurrences at block 34,402	An address occurrence quota, not proof of executed sequence coverage

The last five quota completions occur at blocks 19,747 (`010110`), 23,753 (`100110`), 24,636 (`011010`), 26,443 (`101001`) and 34,402 (`101010`). An address with more associated sequences has a larger imposed quota. The source counter does not select and execute every corresponding sequence, nor verify legal transitions between successive pi blocks. Therefore its printed exhaustion claim is interpreted here as quota completion.

To test an actual traversal claim, define a deterministic sequence-selection policy for each occurrence, track sequence identifiers, verify each cross-block boundary with the existing resolver, and compare coverage with declared control streams and block offsets. A frequency or exhaustion coincidence alone does not establish pi normality, a thermal law, or Bott periodicity. No null-distribution significance is assigned in this revision. The audit’s finite phase-register example is explicitly synthetic and kept separate from these source-code results.

Appendix I Constitutive and normalization checks for the new notes

I1 Volume fluctuations and the water witness

The notes use water's maximum-density range as a material witness for the geometric strain branch [N10]. This can define a separately declared constitutive calibration. The thermodynamic quantity in the fluctuation identity is the variance of the total volume of a fixed amount of material, not a difference between two mean volumes measured at different pressures. For specific volume $v = V / m$ with fixed mass m,

$$Var(v) = \frac{k_B T \kappa_T \langle v \rangle}{m}.$$

At fixed pressure, maximum density gives zero thermal expansion, $\alpha_p = \langle V \rangle^{-1} (\partial \langle V \rangle / \partial T)_p = 0$. In a temperature-independent classical isothermal–isobaric model,

$$\alpha_p = \frac{Cov(V, H)}{k_B T^2 \langle V \rangle}, H = E + pV.$$

It therefore constrains a volume–enthalpy covariance, rather than proving minimal $Var(V)$ or binary locking. A 244-step rule can be proposed as an STO microscopic assumption, but its implied distribution of V and H must then reproduce these response functions. The deterministic binary-pi coverage in H6 does not establish that material distribution.

With R in $J mol^{-1} K^{-1}$ and water molar mass 18.01528 g/mol, $3RT / M$ gives J/g. The upper source temperature 277.3509602013 K gives 384.0113821238 J/g, or 384011.3821238 J/kg. A normalized energy coordinate near 384 remains usable, provided its carrier is retained; it cannot also be read as that same water specific energy in J/kg. The square-root velocity carrier changes accordingly. Similarly, the illustrative linear-elastic density $(100\,atm)^2 / (2 \times 2.15\,GPa)$ is approximately $2.388 \times 10^4\, J/m^3$, not $23.8\, J/m^3$. This is a units check using the notes' illustrative modulus, not a new equation-of-state measurement or an extrapolation into negative-pressure water.

For the normalized flux dyad, $A_\mu \mapsto s A_\mu$ leaves $A_\mu A_\nu / A^2$ unchanged for nonzero s. A density response must consequently change its direction, the scalar coefficient, or other terms; a magnitude change alone cannot supply it. At fixed temperature TASL fixes Θ, so pressure-dependent compressibility can reside in the volume statistics without requiring Θ to change.

I2 Geometric and spectral definitions

The numerical ratio $180 / 64 = 2.8125$ is near the frequency-form Planck peak root, but is not equal to it. Maximizing the frequency spectral radiance yields the nonzero root of $3(1 - e^{-x}) = x$, namely $x = 2.8214393721$. The relative difference is about -0.3168%. Both numbers can be reported with their own definitions; the frequency and wavelength peaks must also be distinguished. Multiplying or dividing by $\ln 2$ changes an information convention, not this extremum equation.

The product $E^3 \times S^3 \times H^1$ has dimension seven as written. Calling it a five-dimensional capability manifold requires a stated constraint or quotient reducing the dimension by two. Likewise $2\pi^2 / 384 \simeq 0.0514042$, whereas $2\pi^2 / \sqrt{384} \simeq 1.0073123$. The latter is the ratio entering the stated

strain comparison. Preserving the square root is essential when transferring a normalized energy to a length coordinate.

These amendments preserve the selected STO premises and distinguish consequences from additional constitutive postulates. They do not change the prime-count codebook, the confirmed galaxy dictionary, or the nuclear RMS operator. The source notes and finite audit accompany the manuscript so that each correction can be checked against its original expression.

Appendix J Reconciliation of the new manuscript additions

J1 Thought experiments and their mathematical roles

The observational prologue [N15] can clarify why the STO operators were sought. Its role is strongest when the motivating observation, exact relation and proposed physical identification remain visible together.

Thought experiment	Construction retained	Observable or additional identification
Repeated diameter spans in one turn	Dimensionless closure ratio and the normalized count map	Physical clock and Anglar carrier; A1 and Section 3.2
Common pendulum and fall interval	$d / L = 2\pi^2$ for the specified idealized common-period comparison	Operational length/time realization; H2
Thermal control and reservoir	$T = \theta_k / \Theta$ and the exact inverse-temperature coordinate	Reservoir response, transport and coupling; Sections 4.4 and 2.1
Constrained rotational route	Helical energy–angular-momentum ledger	Symmetry, mode definition and constitutive drift; E5.2
Shared view and finite resolving power	Distinguish existing records from acquiring a new measured record	Detector resolution, signal propagation and thermodynamic protocol

Recognizing an already available record and acquiring new information are different operations. Neither Landauer's bound nor a geometric analogy assigns every observation a fixed heat cost, and the shared-view example does not establish instantaneous communication. Likewise a small object's greater imaging difficulty concerns angular size, contrast, aperture and the detector; it does not alone replace metric distance by information-rendering work. Those additional identifications can be formulated as STO hypotheses with declared instruments and response maps. They are not used as premises of the horizon proof.

J2 Resolution boundary and a possible transport completion

The new boundary gives a dimensionless control variable χ_D and a crossover duration t_*, but does not determine the transport equation. One possible construction, offered for author review rather than attributed as an existing theorem, is

$$\partial_t u = \nabla \cdot \left[D_{eff}\left(\chi_D, R\right) \nabla u \right] + q \, , D_{eff} > 0 \, ,$$

where u is a specified transported density, q its source and R the declared frame variables. An independently selected positive coefficient or tensor could interpolate between the material and frame regimes. A local material diffusivity must first define χ_D, or the implicit dependence must be solved

explicitly, to avoid using the proposed coefficient to select its own regime. A step at one is a new response assumption; a smooth crossover is a different model. The geometry must determine or externally calibrate the coefficient, transition width and coupling before either predicts data.

The gallon reference remains optional metrology until an independent equation connects its volume to this transport response. The conditions $\ell_D = \Delta L_*$ and $Q = \rho c_p V \Delta T$ alone contain free duration and temperature inputs and do not establish a unique V or Q. The factor-of-1,000 water-specific-energy issue already identified in I1 remains applicable. Neither the numerical curvonic count 384 nor the adoption of a coarse-graining length supplies the missing energy unit.

J3 Editorial and evidential decisions for this revision

Addition	Treatment in the manuscript	Next confirmation or test
Native STO horizon route	Full conditional theorem retained; heat flux includes the boost weight	Independent physical area/entropy slope and state-to-boost map
Planck-scale entropy coefficient	Exact matching identity with the imported G made explicit	Derive tile area independently if a prediction of G is claimed
0.1 mm metrology boundary	Scoped macroscopic resolution proposal P8	Specify domain, clock, carrier and transport law
Bloch holding energy	Work, heat and numerical unitarity residual separated; C4	Select or measure the interaction/rate; 15.3 fW remains conditional
NMR and helical resonator tests	Quantitative candidate responses and controls in E5	Complete prospective registration and independent nuisance calibration
CERN bounded replay	AK5 pT/angular counts reproduced; old energy labels identified as eta	Extraction provenance, defined physical observable and calibrated event-grouped inference

The proposed abstract is reconciled with the confirmed results rather than substituted verbatim. Its 0.297 fm nuclear value is replaced by the confirmed 0.311296 fm operator result. At the recorded external H_0, $a_{STO} = 1.0421978813 \times 10^{-10}\ m\,s^{-2}$; the rounded 1.2×10^{-10} value is not assigned to that calculation. The raw direct CmB coordinate remains the value in Section 4.2, with its energy profile stated. Imported N_A is not described as independently derived, and the normal-strain comparison is not promoted to a proof of electromagnetism. A five-dimensional interpretation of $E^3 \times S^3 \times H^1$ still requires the rank-reducing construction in I2. The bounded CERN recount establishes reproducibility of the available coordinate results; it does not supply a calibrated greater-than-five-sigma mass-gap claim.

These decisions preserve the geometric premises, existing implementation proofs and confirmed response operators. The newly specified laboratory laws extend the theory’s testable content. The current CERN update adds successful bounded pT/angular replay and resolves the historical energy-label ambiguity. The full empirical inference remains subject to the specified observable and calibration tests. Original additions and exports, their hashes, both audit generations, the updated checklist and a manuscript difference file accompany this revision.

Appendix K HTF wavenumber spectral mapping and material readout

The updated working proof and reconciliation briefing connect the HTF acoustic construction to the DRC spectral Anglar table and a proposed stress-sensitive optical experiment [N22, N23]. We retain those contributions to the common quantum and gravitational account. The author's clarification replaces the historical inch interpretation with reciprocal wavelength [N24]. Original source files remain unchanged in the evidence archive; their older unit labels are not adopted as measurement conversions here.

K1 Wavelength and wavenumber references

For the raw theta-k catalyst of Section 4.2, the declared reference carriers give

$$\lambda_m = \frac{\Theta_m}{c} = 0.00254250006782\,m, \tilde{\nu}_m = \frac{1}{\lambda_m} = 393.313657158\,m^{-1}.$$

This ordinary wavenumber is $3.93313657158\,c\,m^{-1}$ or $39.3313657158\,d\,m^{-1}$. The angular wavenumber is instead $\kappa_m = 2\pi/\lambda_m = 2471.26259177\,rad/m$. These are inverse-length quantities. Neither is a length in inches, and their numerical values change with the declared length unit while their physical values remain the same.

The electromagnetic frequency and period are $f_m = c/\lambda_m$ and $t_m = \lambda_m/c$. An acoustic realization requires its own propagation speed and spatial scale. Write

$$\lambda_{ac} = D\,\lambda_m, f_{ac} = \frac{v_s}{D\,\lambda_m} = \frac{v_s}{c\,D} f_m,$$

where $D > 0$ is a dimensionless scale ratio. This explicitly connects the m-point reference to an acoustic wavelength without treating sound and light as having the same propagation speed. The corrected-profile wavelength in A3 is $\lambda_g = \lambda_B$, not λ_m; a calculation must retain its chosen profile and branch through the conversion.

K2 The geometric acoustic branch and declared tuning

The source clarification [N30] deconstructs the divisor before assigning the acoustic velocity. Let $q = 0.2685424928$ denote the printed normalized coefficient and define

$$k_c = \frac{10+\pi^2}{20}, D(q) = \frac{(1/q)^2(\sqrt{2})^3}{k_c}.$$

At the displayed precision $D(q) = 39.4784175945088$, while $4\pi^2 = 39.4784176043574$. The exact geometric coefficient is

$$q_* = \sqrt{\frac{(\sqrt{2})^3}{4\pi^2 k_c}} = 0.268542492766504, D(q_*) = 4\pi^2.$$

The velocity uses the entire product $D(q)2\pi$ in the denominator:

$$\bar{v}_{HTF} = \frac{86400}{D(q)2\pi} = 348.316571965448.$$

The exact-divisor value is $86400/\left(8\pi^3\right)=348.316571878555$. Their difference is the rounding of q, not an additional empirical correction. The factor $\left(\sqrt{2}\right)^3$ carries the temporal power specified in the rotational comparison. Write $D=D(q)\,D_*$ with $\left[D_*\right]=L^{-2}T^3$ and $A=2\pi\,A_*$ with $\left[A_*\right]=L^2T^{-1}$. Then

$$v_{HTF}=\frac{P_{LT}}{D\,A},\left[v_{HTF}\right]=\frac{LT}{\left(L^{-2}T^3\right)\left(L^2T^{-1}\right)}=LT^{-1}.$$

This is the intended dimensional construction: the two carriers in the denominator together have dimension T^2. The pure number $4\pi^2$ has no physical dimension independently of that construction. With the source carriers the resulting speed has coefficient 348.3165719654 in m/s. The equivalent closure $\left[L^2T^{-1}\right]\left[L^{-1}\right]/\left[T^{-2}\right]=LT$ preserves the rotation-period type. Numerically,

$$\frac{1}{1/\left(4\pi^2\right)}\frac{21600}{\pi^2}=86400.$$

Replacing $1/\left(4\pi^2\right)$ by 0.0253302959 gives 86400.0000361; the displayed rounding explains that residual. The shared period factors used here are recorded in A5, including the distinction between $\sqrt{\ell/g}$ and $2\pi\sqrt{\ell/g}$.

With acoustic length $L_{ac}=k_c\ell_*$, $\ell_*=1$ m, and the declared open-ended standing-wave convention, the exact-divisor branch gives

$$f_0=\frac{v_{HTF}}{2k_c\ell_*}=175.301211261\,Hz,f_{F\sharp4}=2f_0=350.602422522\,Hz,$$

$$f_{A4}=f_{F\sharp4}2^{3/12}=416.938895400\,Hz.$$

Its first-overtone wavelength is $k_c\ell_*$ and its ratio to the raw m-point wavelength is $D_{ac}\simeq390.74934$. The table's 417 Hz reference and the briefing's 350.633 Hz dither are distinct declared settings. The exact construction determines the model's speed and tuning; the physical material comparison is assigned to Section 10.

K3 Octave transport into the spectral Anglar table

For an acoustic note $f_{ac,j}$ and declared octave index m_j, define

$$f_j=2^{m_j}f_{ac,j},\lambda_j=\frac{c}{f_j},\Theta_j=\frac{c^2}{f_j},T_{E,j}=\frac{\theta_k}{\Theta_j}=\frac{hf_j}{k_B\ln2}.$$

An octave doubles frequency, photon energy and the energy-equivalent temperature coordinate while halving wavelength, duration and Anglar. It preserves $\Theta_jT_{E,j}=\theta_k$. Thus HTF supplies the declared note and octave inputs, while TASL supplies the consistent spectral coordinate map. $T_{E,j}$ is a bit-energy temperature coordinate; it is not automatically the material temperature or a blackbody spectral-peak temperature.

The six representative note assignments reproduce the source's spectral Anglar entries as follows. Both Anglar columns are numerical coordinates in m^2/s.

DR and color	Acoustic Hz	Octave index	Derived Anglar	Source Anglar
1 Violet	350.65	41	116.556833	116.55
2 Blue	294.86	41	138.610370	138.61
4 Green	262.69	41	155.585114	155.58
5 Yellow	468.07	40	174.634793	174.64
7 Orange	441.80	40	185.018803	185.02
8 Red	417.00	40	196.022320	196.02

Comparing the octave frequencies with $c^2/\Theta_{source,j}$ gives a maximum absolute difference of approximately 0.102 cents [N25]. Some displayed Anglar entries are truncated rather than rounded, so the equality is not exact at the printed precision. This is a reconstruction of the declared table, not an independent observation of acoustic-to-optical energy transfer or a proof that the octave choices are unique. The orange multiplication is corrected to $441.8 \times 2^{40} = 485.764237151437$ THz; the source's 489.062772034765 THz does not follow from its stated inputs.

For a fixed gap reference, the associated energy-equivalent bit coordinate is

$$B_j = \frac{h f_j}{k_B T_g \ln 2} = \frac{f_j}{f_g} = \frac{\Theta_g}{\Theta_j}.$$

This makes the DRC spectral carrier and its temperature reference explicit. It does not identify an energy ratio with the Shannon entropy of an unspecified probability distribution.

The source's display angles and crystallographic spacings require separate typing. For example, the first-order Bragg ratio at a visible wavelength of 400 nm and plane spacing 0.391 nm is $\lambda/(2d) = 511.509$, not 0.511509. That pair admits no real first-order Bragg angle. The latter ratio would instead use 391 nm spacing or 0.4 nm wavelength. Consequently, the declared angle labels remain address metadata until a compatible optical or diffraction measurement model is supplied; they are not used here to validate visible diffraction from atomic plane spacings.

K4 Stress equilibrium and a proposed compatible completion

Use b_c for the geometric container parameter, avoiding confusion with thermodynamic inverse temperature and the m-point bit coordinate. Its compression map is

$$k_c(b_c) = \frac{1}{2} + \frac{\pi^2}{2 b_c}, 1 - k_c(b_c) = \frac{1}{2} - \frac{\pi^2}{2 b_c}.$$

At $b_c = 10$, the source assigns a positive compression magnitude $\epsilon_c = (10 - \pi^2)/20$ and $p_0 = K_{bulk}\epsilon_c$. Reading this geometric ratio as a physical material strain is an adopted constitutive proposal. The alternative expression $\pi^2/2 - \pi^2/(2 b_c)$ in the briefing is not equal to $1 - k_c(b_c)$.

For an annulus with radii r_i, r_o, density ρ, angular speed Ω and Poisson ratio ν, put

$$a_\nu = \frac{3-2\nu}{8(1-\nu)}, b_\nu = \frac{1+2\nu}{3-2\nu}, C_r = r_o^2 r_i^2.$$

With tension-positive Cauchy stress, the proposed fields are

$$\sigma_{rr} = a_\nu \rho \Omega^2 \left(r_o^2 + r_i^2 - r^2 - \frac{C_r}{r^2} \right) - p_0 \ln(r/r_i),$$

$$\sigma_{\phi\phi} = a_\nu \rho \Omega^2 \left(r_o^2 + r_i^2 - b_\nu r^2 + \frac{C_r}{r^2} \right) - p_0 \left[1 + \ln(r/r_i) \right], \sigma_{zz} = \nu(\sigma_{rr} + \sigma_{\phi\phi}).$$

Exact consequence. Since $a_\nu(b_\nu - 3) = -1$, direct differentiation gives

$$\frac{d\sigma_{rr}}{dr} + \frac{\sigma_{rr} - \sigma_{\phi\phi}}{r} + \rho \Omega^2 r = 0.$$

The inner radial traction is zero; the outer radial traction is $-p_0 \ln(r_o/r_i)$. When $r_o/r_i = 2$, the latter is $-p_0 \ln 2$. The logarithm follows from the integration and chosen radius ratio; a Shannon entropy interpretation additionally requires a statistical state. The added pressure field persists at $\Omega = 0$ and requires a source or boundary loading. A microtoroid is not automatically described by the annular geometry used in this calculation.

Force balance does not alone establish compatibility with a displacement. For isotropic linear plane strain with Young modulus Y, the elastic strains from these stresses obey

$$\epsilon_{rr}^e = \frac{1+\nu}{Y}\left[(1-\nu)\sigma_{rr} - \nu\sigma_{\phi\phi} \right], \epsilon_{\phi\phi}^e = \frac{1+\nu}{Y}\left[(1-\nu)\sigma_{\phi\phi} - \nu\sigma_{rr} \right],$$

$$\epsilon_{rr}^e - \frac{d\left(r\epsilon_{\phi\phi}^e\right)}{dr} = q_\epsilon, q_\epsilon = \frac{2p_0(1-\nu^2)}{Y}.$$

Proposed completion for review. An eigenstrain

$$\epsilon_{rr}^* = \epsilon_{\phi\phi}^* = q_\epsilon \ln(r/r_i), \epsilon_{zz}^* = 0$$

cancels that compatibility residual, giving the displacement

$$u_r = r\left[\epsilon_{\phi\phi}^e + q_\epsilon \ln(r/r_i) \right].$$

This construction supplies one mathematically compatible completion, not a unique or author-confirmed physical eigenstrain. Its origin, boundary work and coupling to the occupancy action remain to be selected. The calculation narrows the material-response question without substituting an unexplained stress field for a constitutive law.

K5 Optical readout and connection to the common stress tensor

For the source's stress-optic coefficients C_1, C_2 and unperturbed refractive index n_0, the leading radial and longitudinal index difference is

$$\Delta n_{bi} = -\frac{1}{2} n_0^3 \left(C_1 - C_2\right)\left(\sigma_{rr} - \sigma_{zz}\right).$$

A nondispersive first-order resonance comparison gives $\delta f / f = -\delta L / L - \delta n_{eff} / n_{eff}$. Applying it requires the mode-weighted strain, material coefficients and actual geometry. Moving-boundary and photoelastic contributions must both be included where relevant. A measured index shift would first establish the response of the device; identification of an additional STO response requires its independently specified contribution to that same model.

The EFE link uses the total stress tensor already required by Section 6. In a local rest frame with negligible energy flux, $T_{ab} k^a k^b = \left(\omega^2 / c^2\right)\left(u_E + p_n\right)$ for $k^a = \left(\omega / c\right)\left(1, n\right)$ and $\left|n\right| = 1$. Pressure-positive spatial stress in that ledger is the negative of tension-positive Cauchy stress. The ω^2 here tracks the normalization of k^a; it is not by itself a prediction that changing a probe frequency changes gravitational curvature. A ray in a dielectric also requires its propagation model before it is identified with a vacuum null ray.

The briefing's acoustic perturbation $\delta\sigma_0 \cos\left(\omega_{ac} t\right)$ supplies a prospective optical dither. Linear addition of two such signals does not produce sum and difference sidebands. If a specified coupling multiplies them, the identity

$$\cos\left(\omega_1 t\right)\cos\left(\omega_2 t\right) = 1/2 \cos\left[\left(\omega_1 + \omega_2\right) t\right] + 1/2 \cos\left[\left(\omega_1 - \omega_2\right) t\right]$$

fixes the sideband frequencies and coefficients for that product. Its strength and any asymmetry require the proposed mixing law, not only the trigonometric identity.

K6 Evidence boundary

The HTF audit verifies coordinate arithmetic, spectral reconstruction, stress balance and the proposed compatibility construction [N25, N31]. It reports no new acoustic, optical or gravitational experiment. The contribution is an explicit path from the common occupancy and stress model to a material observable. Physical calibration and prospective tests are consolidated in O3. Additional fluid-regularity, cryptographic and electroweak claims remain archived with their own scope.

Appendix L Time manifold closure and admissible dynamics

The Time Manifold chapter [N27] supplies a common organizing proposal: a physical history consists of admissible geometric transitions, with recurrence, thermal capacity and curvature accounted for on the same state structure. We retain that proposal as an STO premise and construct its finite mathematical realization below. This appendix distinguishes the chapter's topology, routing, measurement and field claims so that each can enter the EFE–QFT argument with a specified domain. The original chapter is preserved unchanged; the constructions marked M are proposed reconciliations for author review.

L1 Typed closure premises

P — Joint representability. Let X be the declared finite set of admissible address and routing records. Introduce maps i_K, i_{24} and i_E from X into a K9 route representation, a decorated 24-cell representation and a selected E8 representation. Compatibility means that these maps preserve specified labels and intertwine the declared actions. This gives a typed meaning to the source's K9–24-cell–E8 intersection: the three objects are different mathematical spaces, and their common content is a compatible representation of X. The existing G2, D4, F4 and PC10 certificates in D4 remain inputs; this appendix does not replace symbols by chord lengths or rerun a chord-only reduction.

P — Recurrence and capacity. The chapter proposes a twofold recurrence operator J with $J^2 = I$ and a finite allocation of geometric channels. We distinguish a finite channel vocabulary, a bounded occupancy per channel and a finite number of physical cells. A global bound on all three is a stronger STO premise than a finite local alphabet. The chapter's universal finite-universe reading may be adopted in that stronger form, but is not inferred solely from the dimension of a Lie algebra. E8 has rank 8, 240 roots and an adjoint Lie algebra of dimension 248 [R38]. Selecting an E8 representation and bounding its multiplicity are additional model data; 248 is not an automatic upper bound on every representation or composite system.

P — Thermal and geometric closure. Retain $T\Theta = \theta_k$ with T a temperature, Θ an Anglar and θ_k carrying dimensions $L^2 T^{-1} K$, as in Section 2. This is a coordinate invariant, not by itself a numerical maximum entropy or curvature. If the source intends an occupancy ceiling, specify the dimensionless occupancy and the inequality it obeys. The source's globally non-flat premise is retained. The stronger requirement $R_{ab} \neq 0$ everywhere is recorded as an additional restriction: Ricci-flat and Riemann-flat are different conditions. A routing tag called curvature-flat or neutral denotes a routing balance unless a spacetime curvature reconstruction is supplied.

M — Operational equivalence. A discarded coordinate is redundant only if it leaves all allowed outcome distributions and subsequent transitions unchanged. Equality of one projected length is insufficient. Define two records to be equivalent when every admissible experiment has the same probability distribution on them; form a quotient only after proving that admissible dynamics respects that equivalence. This connects the source's realized ladder to P1 without assuming that a finite list of measurement outcomes already determines the complete state space.

L2 Chord inventory projection and twofold recurrence

For the unit-circumradius 24-cell, use vertices obtained by permuting $(\pm 1, \pm 1, 0, 0)/\sqrt{2}$. Independent enumeration gives 276 unordered distinct vertex pairs. Their squared-distance multiplicities at 1,2,3,4 are 96,72,96,12. Directed distinct pairs number 552 with multiplicities 192,144,192,24. Including the 24 self-pairs gives 576 ordered pairs, now including a zero-distance class. Thus 96 undirected edges, all geometric chords and a 576-entry protocol inventory are different counts. The chapter's weighted allocation (96,144,288,48) can be retained as a declared protocol inventory, as already distinguished in D4; identifying it with ordinary vertex pairs requires explicit decoration or multiplicity rules. Its asserted 384 symmetry classes likewise require the declared equivalence relation, not just the ATCS value 384.

C — Restricted projection ladder. A concrete realization of the source's four span values is $v = (1,1,1,1)$ and the nested coordinate projectors P_j onto its first j axes. Then $\| v \| = 2$ and $\| P_j v \| = \sqrt{j}$ for $j = 1,2,3,4$. These four values follow exactly for the selected projectors. Allowing arbitrary subspaces gives intermediate norms, so quantization resides in the admissible measurement

contexts as well as the vector. This example supplies a witness for the projection rule; it does not assert that these P_j are already the stack's complete measurement instrument.

M — Quantum readout. On the selected finite Hilbert space choose orthogonal projectors Π_j summing to I and a calibrated observable $A=\sum_j a_j \Pi_j$, with a_j proportional to the allowed geometric readouts. The retained Born rule gives $p_j=Tr(\rho \Pi_j)$; conditional preparation gives $\rho_j=\Pi_j \rho \Pi_j / p_j$ when $p_j>0$. This makes the source projection proposal compatible with the implemented Bloch branch. Deterministic outcomes require a state supported in one outcome subspace or a further measurement mechanism. The chord list alone does not select probabilities or resolve all measurement dynamics.

C — Involution sectors. For a Hermitian involution J, $\Pi_{\pm}=(I \pm J)/2$ are orthogonal projectors. Every function of J has the form $f(J)=f(1)\Pi_+ + f(-1)\Pi_-$. Consequently, evolutions that are functions of one fixed J commute and cannot represent every Bloch rotation. The reconciled two-period spine is a grading or a declared generator in a larger algebra of ladder-preserving operations. If several generators are used, their products must be checked separately; two involutions can generate transformations of longer or unbounded order. Neither real-time spinor recurrence nor the twofold label alone establishes Bott periodicity; H4 retains the required Clifford-algebra test.

L3 From routing permissions to a common generator

The source operator card specifies the routing correspondence

DR tag	Permitted Hamiltonian family	Source interpretation
819	9-1 and 9-8	Perimeter
891	9-2 and 9-7	Barycentric
981	9-4 and 9-5	Excited
999	All three families subject to the other rules	Universal junction

The values are retained as the declared routing contract. The canonical row table, ordering, zero-padding and difference convention determine the exact tag calculation. In particular, a difference of two three-digit integers cannot be partitioned into three three-digit blocks without an additional nine-position construction. The source row and concatenation conventions define the domain; a displayed integer alone does not define that encoding. The unique all-999 pair and invariance under particular relabelings are finite certificate claims for that specified domain. A classification into four labels is not, without a group and its action, a proof of four group orbits.

M — Weighted reversible sector. On a sector of mutually admissible transitions choose symmetric weights $w_{xy}=w_{yx}\geq 0$, zero on forbidden edges, and positive cell weights μ_x. For a scalar field f define

$$(\Delta_\Gamma f)_x=\mu_x^{-1}\sum_y w_{xy}(f_y-f_x), \langle f,g\rangle_\mu=\sum_x \mu_x f_x^* g_x.$$

C — Conservation and dissipation. With fixed weights and a closed graph,

$$\sum_x \mu_x(\Delta_\Gamma f)_x=0, \langle f,-\Delta_\Gamma f\rangle_\mu=\frac{1}{2}\sum_{x,y} w_{xy}|f_y-f_x|^2\geq 0.$$

Both statements follow by pairing the x,y and y,x terms. Hence $\partial_s f = \Delta_\Gamma f$ conserves the weighted sum and decreases the Dirichlet energy. On each connected component the kernel consists of constant fields. This is an exact route-to-diffusion construction once the weights are chosen. It is not a new claim that the stack's routing tag alone supplies those weights. Directed chiral transitions require a stationary measure and a directed generator, or a reversible enlarged state model; symmetrization must not silently authorize forbidden reverse moves.

The corresponding positive operator can also enter the quantum and thermal branches. With a declared energy coefficient $E_\star$ and a self-adjoint diagonal potential V, let $H = E_\star\left(-\Delta_\Gamma\right) + V$, taking the graph quantities dimensionless or assigning $E_\star$ the compensating units. Then $U(t) = \exp\left(-iHt/\hbar\right)$ and $\exp\left(-\beta_T H\right)$ use the same route-dependent spectrum, as in Section 7.1. This construction gives the chapter a direct role in reconciliation: permissions determine operator support, a constitutive choice determines weights and energies, and TASL determines the thermal coordinate. A scalar graph diffusion, a quantum Hamiltonian and a spacetime curvature flow remain distinct operators linked by specified maps.

In the smooth spatial case the corresponding scalar operator is

$$\Delta_h f = \frac{1}{\sqrt{\det h}}\,\partial_i\left(\sqrt{\det h}\,h^{ij}\,\partial_j f\right).$$

This corrects the source's malformed displayed denominator. A Lorentzian field operator instead uses the Lorentzian metric and is not a positive diffusion generator. The local-average interpretation is exact for a normalized graph operator; on a smooth manifold it requires the appropriate small-neighborhood limit or harmonic measure.

L4 Finite capacity and the field correspondence

C — Finite allocation theorem under explicit bounds. Suppose q channel types carry nonnegative integer occupancies n_i with $\sum_i n_i = b$, where q and b are fixed. The number of allocations is

$$D_{alloc} = \binom{b+q-1}{q-1}.$$

This follows by the stars-and-bars bijection. If each allocation carries a selected internal space of finite dimension d_{int}, the Hilbert-space dimension is at most $d_{int}D_{alloc}$. Its entropy is bounded by $k_B \ln\left(d_{int}D_{alloc}\right)$. Finite many cells with finite local dimensions also have a finite product bound. A finite alphabet alone does not impose these occupancy, multiplicity or cell-count bounds. This theorem supplies a precise version of the chapter's finite-capacity claim without silently replacing its protocol inventory with ordinary chord counts.

If W is the occupancy or energy quantity intended to be conserved, a closed quantum dynamics must satisfy $[H, W] = 0$. A finite set of channels alone does not prove that commutator vanishes. In a stochastic description the corresponding generator must preserve the chosen account. These tests connect the source's curvature-information conservation premise to the explicit balance law in D3.

The fixed-resolution STO option does not require a physically infinite Hilbert space: a finite microscopic model can be compared with QFT through low-energy observables, with errors bounded over a declared energy, length and time range. The alternative refinement construction in Section 7 remains available.

Finite matrices remove divergences in that finite calculation, but matching effective couplings and recovering causal propagation remain physical tasks. No infinite-dimensional ultraviolet limit is imposed as a premise of STO.

For a tensor-network realization, the Schmidt rank across a cut is at most the product of the bond dimensions crossed, so $S_A \le k_B \sum_e \ln D_e$. This is an exact representation bound. An area-law prediction additionally requires a relation between the crossed bonds and physical area, with a fixed local bond bound. A fixed finite quantum system also saturates its entropy; saturation alone does not distinguish STO. The discriminating prediction must specify a smaller ceiling, onset scale or response law before examining the comparison data.

L5 Spherical topology and the proposed metric flow

The source assigns physical meaning to spherical temporal closure. We retain this as a candidate global topology selection, with the mathematical objects separated:

$$\partial B^3 = S^2, \partial S^3 = \varnothing, \partial B^4 = S^3.$$

M — Two-patch construction. Take two closed three-balls and identify their S^2 boundaries by the standard identification. Their double is S^3. This realizes a spherical closed ledger from two bounded patches. It does not assert that a two-period clock itself performs that gluing. More generally, a closed, connected, simply connected three-manifold is homeomorphic to S^3 by the Poincaré theorem [R36]. Here closed means compact without boundary. STO must select those hypotheses, or adopt spherical closure directly; a scalar ratio $d/L = 2\pi^2$ by itself is not a topological classification. A round S^3 of radius r has volume $2\pi^2 r^3$, providing a normalized volume comparison without equating that volume with an arbitrary diameter-to-arc ratio.

Finite thermal capacity does not alone imply compactness or positive Ricci curvature, and nonzero Ricci curvature does not alone imply a round metric. The topology theorem also does not specify a Lorentzian spacetime evolution. A candidate effective spacetime can have spatial S^3 slices with a separately defined lapse, shift and time evolution. The source's exclusion of alternative global topologies is thus retained as a physical selection premise whose consequences can be developed, rather than attributed to the numerical ratio alone.

M — Metric reconstruction and flow test. Let a reconstruction map R turn an admissible graph state and its edge data into a spatial metric h. If F_ϵ is a microscopic update, the proposed Ricci correspondence requires a controlled relation of the form

$$\frac{R(F_\epsilon x) - R(x)}{\delta s} = -2\,Ric(h) + L_V h + o(1),$$

with the reconstruction, convergence norm, flow parameter s and gauge vector V specified. This is the concrete task connecting the Δ^R route rule to the source's geometric-flow claim. Ricci flow is a Riemannian metric evolution; identifying its parameter with physical Lorentzian time requires an additional dynamical argument [R37].

The chapter's alternative formula $\Delta_R g_{ab} = \nabla^2 g_{ab} - \nabla_a \nabla_b \log\Theta$ is a separate flow ansatz. For the Levi-Civita connection $\nabla g = 0$, so the covariant rough Laplacian of g vanishes. A componentwise Laplacian in a chosen gauge is a different operator and must be written as such. The logarithm should also use a

dimensionless ratio $\Theta / \Theta_{\star}$. We therefore retain the expression as a proposed flow ansatz to be completed through R, rather than claim that it already equals $-2\,Ric$. The horizon-to-Einstein construction in Section 6 continues to use its stated entropy and stress inputs and does not depend on an unproved Ricci-flow equivalence.

L6 Nuclear finite differences as a shared observable

The chapter adds an exact connection useful to the nuclear branch. At fixed proton number Z, define $S_{2n}(N,Z) = B(N,Z) - B(N-2,Z)$. Then

$$S_{2n}(N+2,Z) - S_{2n}(N,Z) = B(N+2,Z) - 2B(N,Z) + B(N-2,Z).$$

The equality follows by substitution. Thus the change in two-neutron separation energy is an unnormalized second difference of binding energy. If a normalized lattice Laplacian with spacing 2 is used, divide the right side by 4. S_{2n} itself is a first difference; it is not automatically a second derivative of a spacetime metric. Mapping B or R_c to a metric component needs a scale, sign convention and response relation. With signature $(-,+,+,+)$, a radius proportional to $\sqrt{g_{tt}}$ must be replaced by a specified positive quantity, such as $\sqrt{-g_{tt}}$ in an applicable timelike chart, and a length carrier.

This gives a comparison independent of refitting the confirmed RMS operator in G1: compute B and S_{2n} from one frozen nuclear model, evaluate the same finite differences in an independently specified mass dataset, and test whether predicted shell changes occur at the declared N. The identity alone does not derive magic numbers. The rotation-period rescaling in the source is also exact: with $t = T_{rp}\sigma/(2\pi)$, $d^2/dt^2 = (2\pi/T_{rp})^2 d^2/d\sigma^2$. It rescales a fixed cycle operator; it does not alone establish equivalence of all physical reference frames.

L7 Tests and disposition of the source claims

The earlier audit [N29] enumerates 24-cell distances, verifies the restricted projection ladder, checks an involution's spectral sectors and an illustrative weighted graph, and verifies nuclear finite-difference and period-rescaling identities. The fresh N31 audit additionally executes the actual source circuits described in Section 5.3. These distinct evidence sets are retained with their sources and scopes.

The closure restrictions are P; the proven finite identities are C; the metric, quantum-instrument and capacity constructions are M. Their physical identification is recorded in Section 10. Acoustic interpretation follows K and N30, with no reinstatement of inch locks. Concurrent routing, cryptographic resistance and ecological saturation are not used as premises for the EFE–QFT conclusion.

Appendix M Continuous space and a closed discrete realization

M1 Continuous spatial carrier with discrete temporal resolution

This proposed completion implements P0 without replacing space by a finite point set. Let Σ be a continuous compact spatial manifold with a chosen measure, and let $\{\varphi_1, \ldots, \varphi_N\}$ be orthonormal spatial functions at a declared resolution. Define the isometry

$$J : \mathbb{C}^N \to L^2(\Sigma),\ J\,z = \sum_{a=1}^{N} z_a \varphi_a,\ J^{\dagger} J = I_N.$$

A circuit state is the coefficient vector z_j at discrete clock occurrence j. Its continuous spatial realization is $\psi_j = J z_j$. For an executed circuit unitary U_j, define

$$z_{j+1} = U_j z_j, \psi_{j+1} = J U_j J^\dagger \psi_j.$$

On $ran\, J$, norm is preserved exactly because $J^\dagger J = I$ and $U_j^\dagger U_j = I$. On all of $L^2(\Sigma)$, the extension $\widetilde{U}_j = J U_j J^\dagger + (I - J J^\dagger)$ is unitary and leaves unresolved modes unchanged. This extension is a mathematical choice, not a claim that every physical unresolved mode is frozen. A varying resolved subspace uses an explicitly declared quantum instrument or an enlarged unitary dilation; projection alone is not unitary.

A spatially continuous carrier therefore admits finite, discrete-time control without contradiction. To implement temporal bandwidth, select a spectral projector P_B onto the generator modes distinguishable by the clock/readout. For a uniform tick δt, the phases of U determine frequencies only modulo $2\pi / \delta t$. Restricting the eigenphase branch to $(-\pi, \pi]$ is one explicit bandwidth convention. Discreteness alone does not uniquely choose that band or eliminate unresolved modes.

The audit embeds the actual 36-dimensional production AME operator in 36 continuous Fourier functions on a circle. Exact finite Fourier quadrature gives a Gram error 2.08×10^{-15} and norm-change residual zero at displayed precision [N31]. This is a constructive compatibility witness for continuous space and the implemented finite gate. A circle witness is not asserted to be the physical three-dimensional geometry. The construction applies to orthonormal modes on a continuous curved three-manifold once the physical basis in O1 is selected.

M2 Conserved total energy and driven subsystem accounting

For a self-adjoint total generator H_{tot} on a resolved closed sector and the clock intervals of A5, set

$$U_j = \exp[-i H_{tot} \delta t_j / \hbar], \rho_{j+1} = U_j \rho_j U_j^\dagger.$$

Then $U_j^\dagger H_{tot} U_j = H_{tot}$, so

$$E_{j+1} = Tr(\rho_{j+1} H_{tot}) = Tr(\rho_j H_{tot}) = E_j.$$

This exact discrete conservation theorem realizes P7. It allows continuous space through M1 and does not require a globally flat metric. The same finite Hamiltonian yields $\rho_\beta = e^{-\beta_T H_{tot}} / Z$ with β_T supplied by TASL. Autonomous evolution and the thermal state thus share an energy spectrum and clock carrier.

Conversely, a finite unitary $U = W\, diag(e^{i\phi_a}) W^\dagger$ admits $H_U = -(\hbar / \delta t) W\, diag(\phi_a) W^\dagger$. It conserves H_U, but the logarithm's branch and its physical energy interpretation are additional choices. A common conserved H across distinct gates requires $[U_j, H] = 0$ for every gate; separate gate logarithms do not prove that condition. The audit's production-AME witness gives an autonomous-energy residual 7.22×10^{-16} in normalized units.

For a driven subsystem with selected energy H_S, the gate work is instead

$$W_j = Tr[H_S(U_j \rho_j U_j^\dagger - \rho_j)].$$

A global account assigns $\Delta E_C = -W_j$ to the controller, together with any interaction-energy change. This scalar assignment is an explicit ledger; a microscopic implementation additionally includes the controller in H_{tot}. More generally, for $H_{tot} = H_S + H_C + H_R + H_{int}$, autonomous evolution gives

$$\Delta E_S + \Delta E_C + \Delta E_R + \Delta E_{int} = 0.$$

The audit uses the same AME gate with $H_S = diag(0, \ldots, 35)$ and obtains $\Delta E_S = -0.1821114559$. The compensating controller ledger is $+0.1821114559$. This deliberately nonzero example prevents unitarity from being misreported as conservation of every chosen subsystem energy. Thermal channels and re-preparation use the same inclusive account; their subsystem entropy need not be constant.

M3 A constrained occupancy completion

The supplied potential in D3 has an exact stress variation but needs a defined field sector. A compatible proposed completion retains the dyadic source instead of replacing it. Introduce a unit timelike observer field u^a and spatial projector $h^{ab} = g^{ab} + u^a u^b$. Restrict covectors $V_a^I = (r_a, d_a, C_a)$ to the spatial sector, with constraints $u^a V_a^I = 0$ and $h^{ab} V_a^I V_b^I = v_I^2 > 0$. The non-null flux vector C_a replaces A_a in the potential. When electromagnetic gauge covariance is desired, use $C_a = \nabla_a \varphi - q A_a^{em}$ with the corresponding joint phase transformation. This is a proposed sector choice, not a claim that every source flux is spatial.

Use spacetime coordinates with a common length carrier and normalized $u^a u_a = -1$. Choose positive κ_I and dimensionless propagation coefficients $b_I = s_I / c \in (0, 1]$, retaining the action carrier explicitly. Define

$$L_{dyn} = \frac{1}{2} \sum_I \kappa_I h^{ab} \left[\left(u^c \nabla_c V_a^I \right) \left(u^d \nabla_d V_b^I \right) - b_I^2 h^{cd} \left(\nabla_c V_a^I \right) \left(\nabla_d V_b^I \right) \right].$$

A concrete observer and constraint choice is

$$L_{observer} = -\frac{\kappa_u}{2} g^{ab} g_{cd} \left(\nabla_a u^c \right) \left(\nabla_b u^d \right), \kappa_u > 0,$$

$$L_{constraints} = \lambda_u \left(u^a u_a + 1 \right) + \sum_I \left[\lambda_I \left(h^{ab} V_a^I V_b^I - v_I^2 \right) + \eta_I u^a V_a^I \right].$$

The proposed total occupancy action is therefore

$$I_{occ} = \int_M \sqrt{-g} \left(L_0 + L_{dyn} + L_{constraints} + L_{observer} \right) d^4 x.$$

Vary all fields and multipliers, not just the metric. Its variational stress includes all four sectors, and D3's identity supplies total on-shell balance. The logarithm of $|C^2|$ is regular on the fixed-norm sector; the multipliers supply the reaction terms absent from the potential-only equation. The observer action above is an explicit proposed choice within the geometric premise, not a previously established STO axiom. The horizon construction then uses the total stress rather than omitting the observer contribution.

In a fixed observer frame with fixed positive coefficients, the temporal kinetic and spatial gradient contributions to the Hamiltonian have positive signs. The norms constrain $r \cdot d$ to a bounded interval by Cauchy–Schwarz, so the potential is bounded on that compact directional sector. A finite-mode

quantization gives a finite self-adjoint matrix after a declared finite local-state truncation and therefore a well-defined unitary update and finite Gibbs state. This proves existence of a consistent regulated candidate; it is not a proof of full continuum stability or of a particular physical coefficient. Treating the observer as dynamical also requires its own equations rather than omitting its stress.

The completion supplies the missing structural choices explicitly: constrained fields, kinetic terms, an inclusive action and a finite quantum realization. Its field coefficients and physical identifications, and adoption or revision of the displayed observer action, are the single O1 review item. The source's original potential and the coefficient repair remain visible in D3. No additional fitted numerical value is inserted to force a comparison with water or a particle measurement.

References

R1. S. Hollands and R. M. Wald, "Quantum fields in curved spacetime," *Physics Reports* 574, 1–35 (2015). DOI; arXiv:1401.2026.

R2. J. F. Donoghue, "General relativity as an effective field theory: The leading quantum corrections," *Physical Review D* 50, 3874–3888 (1994). DOI; arXiv:gr-qc/9405057.

R3. T. Jacobson, "Thermodynamics of spacetime: The Einstein equation of state," *Physical Review Letters* 75, 1260 –1263 (1995). DOI; arXiv:gr-qc/9504004.

R4. W. G. Unruh, "Notes on black-hole evaporation," *Physical Review D* 14, 870–892 (1976). DOI.

R5. R. C. Tolman and P. Ehrenfest, "Temperature equilibrium in a static gravitational field," *Physical Review* 36, 1791–1798 (1930). DOI.

R6. J. D. Bekenstein, "Universal upper bound on the entropy-to-energy ratio for bounded systems," *Physical Review D* 23, 287–298 (1981). DOI.

R7. G. Lindblad, "On the generators of quantum dynamical semigroups," *Communications in Mathematical Physics* 48, 119–130 (1976). DOI.

R8. D. Reeb and M. M. Wolf, "An improved Landauer principle with finite-size corrections," *New Journal of Physics* 16, 103011 (2014). DOI; arXiv:1306.4352.

R9. F. Pastawski, B. Yoshida, D. Harlow, and J. Preskill, "Holographic quantum error-correcting codes: Toy models for the bulk/boundary correspondence," *Journal of High Energy Physics* 2015(6), 149. DOI; arXiv:1503.06237.

R10. F. Lelli, S. S. McGaugh, and J. M. Schombert, "SPARC: Mass models for 175 disk galaxies with Spitzer photometry and accurate rotation curves," *Astronomical Journal* 152, 157 (2016). DOI; arXiv:1606.09251.

R11. S. S. McGaugh, F. Lelli, and J. M. Schombert, "Radial acceleration relation in rotationally supported galaxies," *Physical Review Letters* 117, 201101 (2016). DOI; arXiv:1609.05917.

R12. E. Knill and R. Laflamme, "A theory of quantum error-correcting codes" (1996 preprint). arXiv:quant-ph/9604034.

R13. C. Eling, R. Guedens, and T. Jacobson, "Non-equilibrium thermodynamics of spacetime," *Physical Review Letters* 96, 121301 (2006). DOI; arXiv:gr-qc/0602001.

R14. T. Jacobson, "Entanglement equilibrium and the Einstein equation," *Physical Review Letters* 116, 201101 (2016). DOI; arXiv:1505.04753.

R15. R. Bousso, Z. Fisher, J. Koeller, S. Leichenauer, and A. C. Wall, "Proof of the quantum null energy condition," *Physical Review D* 93, 024017 (2016). DOI; arXiv:1509.02542.

R16. J. S. Bell, “On the Einstein Podolsky Rosen paradox,” *Physics Physique Fizika* 1, 195–200 (1964). DOI.

R17. D. Adhikari et al. (PREX Collaboration), “Accurate determination of the neutron skin thickness of lead-208 through parity-violation in electron scattering,” *Physical Review Letters* 126, 172502 (2021). Primary paper. Used for the 0.283 ± 0.071 fm comparison.

R18. Gravitational Wave Open Science Center, *Public API Documentation* and *Technical details for Advanced LIGO and Virgo event data releases*. API; technical details. Accessed 27 September 2026. Used for the GW150914 catalog time and the role of sampling, calibration and data-quality records.

R19. A. Jaffe and E. Witten, *Quantum Yang–Mills Theory*, Clay Mathematics Institute problem statement. Primary statement. Used only to distinguish the claimed continuum result from a finite or modified theory.

R20. ATLAS Collaboration, *High-mass di-photon resonances: the first 2016 ATLAS results*, 5 August 2016. Official result.

R21. P. Fraundorf, “Heat capacity in bits,” *American Journal of Physics* 71, 1142–1151 (2003). Author preprint. Entropy slope and natural thermal information units.

R22. P. Fraundorf, “Friendly units for coldness” (2006). arXiv:physics/0606227. Byte and energy units for inverse temperature.

R23. M. F. Atiyah, R. Bott and A. Shapiro, “Clifford modules,” *Topology* 3, Supplement 1, 3–38 (1964). DOI; full text. Sections 4–6, including the algebra and module tables.

R24. D. Tong, *Lectures on Gauge Theory*, chapter 2, printed pp. 49–51, “Another Analogy: Bloch Waves.” Author notes. Accessed 4 October 2026. Integer phase actions and their distinct gauge and translation interpretations.

R25. C. G. Callan, R. F. Dashen and D. J. Gross, “The structure of the gauge theory vacuum,” *Physics Letters B* 63, 334–340 (1976). DOI. Original theta-vacuum reference identified in the supplied source; the comparison here follows R24.

R26. R. Jackiw and C. Rebbi, “Vacuum Periodicity in a Yang–Mills Quantum Theory,” *Physical Review Letters* 37, 172–175 (1976). DOI. Original reference identified in the supplied source; the comparison here follows R24.

R27. M. Laine and A. Vuorinen, *Basics of Thermal Field Theory*, Lecture Notes in Physics 925 (2016), chapter 4. Updated author text; DOI. Euclidean thermal interval and bosonic and fermionic boundary conditions.

R28. D. Tong, *Lectures on Fluid Mechanics*, printed pp. 18–20, Bernoulli theorem. Author notes. Accessed 4 October 2026.

R29. D. G. Jorgensen, *Relationships between basic soils-engineering equations and basic ground-water flow equations*, USGS Water-Supply Paper 2064 (1980). DOI. The official abstract supports the material-storage comparison; the supplied storage article supplies the displayed notation.

R30. T. Gingrich, *Chemistry 444 Problem Set 6*, Northwestern University (2025), problem 3. Author course material. Isothermal–isobaric compressibility fluctuation relation, independently derived in H5.

R31. Gravitational Wave Open Science Center, *Timeline documentation* and *Science Mode History*. Timeline; history query. Accessed 6 October 2026. Segment records describe detector status and availability.

R32. Gravitational Wave Open Science Center, *Technical details for Advanced LIGO and Virgo event data releases*. Technical documentation. Accessed 6 October 2026. Strain time series and data-quality/injection records are distinct data products.

R33. Gravitational Wave Open Science Center, *H1 science-mode history segment list*, GPS 770000000–1271462418. Official JSON. Retrieved 6 October 2026. Includes the interval [1126252291,1126274322); only the relevant interval is used here.

R34. ROOT Collaboration, *ROOT::Math::PtEtaPhiM4D Class Template Reference* and *PtEtaPhiE4D Class Template Reference*, ROOT v6.36. Mass-coordinate reference; energy-coordinate reference. Accessed 8 October 2026. Coordinate definitions distinguish pseudorapidity from energy; the CMS collection implementation is now documented in R40.

R35. O. Millet, D. R. Muhandiram, N. R. Skrynnikov and L. E. Kay, "Deuterium Spin Probes of Side-Chain Dynamics in Proteins. 1. Measurement of Five Relaxation Rates per Deuteron in 13C-Labeled and Fractionally 2H-Enriched Proteins in Solution," *Journal of the American Chemical Society* 124, 6439–6448 (2002). DOI; author-hosted paper. Equation 1c and the independent relaxation-mode measurements support the baseline comparison; this is not evidence for the proposed confined-water coefficient jump.

R36. J. Morgan and G. Tian, *Ricci Flow and the Poincaré Conjecture*, Clay Mathematics Monographs 3 (2007). Publisher description; author monograph. The topological conclusion requires a closed simply connected three-manifold.

R37. G. Perelman, "The entropy formula for the Ricci flow and its geometric applications" (2002), arXiv:math/0211159. Riemannian geometric flow; physical-time identification is a separate STO proposal.

R38. American Institute of Mathematics, *What is E8?* and *A picture of the E8 root system*. Definition; root-system description. Accessed 23 October 2026. Distinguishes the eight-dimensional root space, 240 roots and 248-dimensional Lie algebra.

R39. CMS Collaboration (2017), *VBF1Parked primary dataset in AOD format from Run of 2012*, /VBF1Parked/Run2012B-22Jan2013-v1/AOD. Record 6025, DOI 10.7483/OPENDATA.CMS.69GK.Z9UD. Official index metadata identify the three source filenames. The record requires validated-run selection and documents the trigger-selected dataset.

R40. CMS Collaboration, CMSSW_5_3_X, `JetTracksAssociation.cc`, `JetExtendedAssociation.cc`, and `JetExtender.cc`. Track sum implementation; association producer. Retrieved source snapshots and hashes are retained in revision8. These define the summed, massless-track four-vector and zero initialization used to interpret the exported collection.

Additional archived source references

E1. `Rotmod_LTG.zip`, 175 rotmod files, and author script `ntestgal1.py`. Prior reproduction outputs and new fixed-response audit are included in the evidence package.

E2. `sto ennergy cms.zip`, analysis script `cms_sto_analysis11.py`, 14 CSV exports and figures. The prior aggregate and figure audit is retained; N6 adds the intended original data inventory.

E3. *Metrological Ledger of the Dimensional Emergence and Rotational Spacetime Framework*, 20 September 2026, equations 19–24, especially the supplied occupancy tensor on page 4.

E4. `Primelocks.zip`, Prime Genetics, Prime Harmonics, DMC and Prime Lock chapters, compendium, geometric notes and implementation modules.

E5. `Yang Mills Paper_250711_120710.txt` from E4. This later filename is no longer used to date the origin of the work; N1 supplies the January document metadata.

E6. AxiomARC 14-proof implementation matrix, Goal 3 unified compendium and unchanged source/test files from `OMporium_AxiomARC_Beta_3_Complete(1).zip`. The G2 module matches compendium hash prefix 75bc1d02d234. The exact audit and source hashes accompany the paper.

N1. `Sto_works/RP4_Yang_Mills_Paper_Rev3.docx`. Internal metadata: created 6 January 2025 at 21:46 UTC; modified 13 January 2025 at 00:01 UTC; creator Chris Schiele. SHA-256 e1621556e6bbf0eee12646c390e808bc4ce4857c582f3a4eb41af0e07cfb47ac. Metadata and author attribution support the January provenance; independently certified priority is not asserted.

N2. `Sto_works/Addendum 1 - 24-Vertex Modeling v2.docx`. Sections 1–5 and orbital overlays. Nuclear RMS operator reconstructed in Appendix G1; companion model code comes from the earlier STO nuclear-binding archive.

N3. `Sto_works/Addendum 2 - TASL_Hydrogen_Spectrum_Water_Ladder.pdf`. Exact frequency-coordinate map, supplied line examples and proposed environmental application.

N4. `Sto_works/Addendum 3 - TASL_TTDL_Validation_Appendix.pdf`. Thermal anchors, TTDL gate identity and weak-angle number correspondence.

N5. `Grav_finder.zip`: `grav_finder.py`, `grav_finder_v2.py`, H1-labeled strain CSV and Prime Lock comparison CSV. Input hashes, arithmetic audit and source-dependency findings are recorded in the reproduction package.

N6. Author-supplied CERN source folder, inspected 27 September 2026. Three ROOT basenames and byte sizes are recorded in Appendix E4 and the inventory. This citation establishes the supplied location, not independent authentication of its CMS provenance or event content.

N7. `tools_sto_quick.py`, supplied October 2026. Raw TASL catalyst, m-point coordinates and geometric-clock ratios. Original source and SHA-256 in `revision3/sources/` and its manifest.

N8. `tools_hex_pi_analyzer.py`, supplied October 2026. DRC assembly grammar, spectral table, binary-pi generator and quota counters. Selected functions and arithmetic are audited without modifying the source.

N9. Eight author-supplied Wikipedia PDF snapshots: *Thermodynamic beta*, *Bloch's theorem*, *Theta vacuum*, *Bott periodicity theorem*, *Hydraulic head*, *Specific weight*, *Compressibility*, and *Specific storage*. Used to identify the proposed correspondences and the exact lower I Ching mnemonic; primary and author references R21–R30 support the mathematical and physical comparisons. Snapshot files and hashes are retained in the review package.

N10. `sto_notes.md`, supplied with the October review-decision update. The microscopic horizon construction, fluid response, occupancy potential and path-delay proposals are reconciled in B, D3, Sections 7.2–8.2 and I. Original text and hash are preserved.

N11. `01-RE_Discovery-of-Prime-Locks.docx`. Historical Prime Locks development and proposed GW/particle comparisons. Preserved as supplied with internal document metadata and SHA-256.

N12. `02-PL1-Evolution-of-Prime-Locks-Theory.docx`. Sections headed "Experimental Results," "Wavelet Analysis Confirms Shared Harmonic Structures" and "Predictive Relationships with GW150914." Preserved as a reported-analysis source, not a new detector replay.

N13. `03-RE_Prime-Locks-Fundemental-Constants-Gravity.docx`, *Research Notes on Prime Lock and Fundamental Constants and Gravitational Wave Alignment*. Contains the H1 filename, two complex correlation reports, the explicitly synthetic filament comparison, adaptive node proposals and entropy-alert descriptions. Reported figures are distinguished from independent event measurements in E3.

N14. Christopher Schiele, review-decision and authorship update received for this revision, 6 October 2026 UTC. Confirms E2 and G1; supplies N10–N13 and the query-specific H1_SCI link; reports pending CERN reduction with Alex Malyuta; specifies the author roles. The supplied partial JSON excerpt is retained separately from the verified enclosing interval in R33.

N15. `manuscript_addition.md`, received for the 8 October 2026 reconciliation. Contains four proposed insertions plus abstract and observational prologue. Original preserved unchanged under `revision5/sources/`; Sections 2.1 and 6.4, C4, E5 and J record the reconciled treatment.

N16. Three `CMS_Reduced_STO_Events_*.npz` files with basenames 002D3E25-A775-E211-A564-0026189438FC, 0080CAE1-4C75-E211-98F1-003048FFCC1E and 00FA0A53-5D75-E211-985B-00304867BFB0. Each contains 2,880 rows and declared original-file metadata. Local hashes and safe schema checks are recorded in the new audit; original ROOT hashes are not independently recomputed.

N17. `root_002D3E25-A775-E211-A564-0026189438FC.zip`, `Root_0080CAE1-4C75-E211-98F1-003048FFCC1E.zip` and `Root_00FA0A53-5D75-E211-985B-00304867BFB0.zip`. Supplied result archives: 39 CSVs and 218 PNGs. The archive membership, checksums, duplicate-image groups and exact score recalculations are included in `revision5/results/`.

N18. `root_003048FFCC1E_results.md`, supplied run log. Names the 0080 ROOT source and reports multiple analysis methods; repeated log blocks are not treated as independent samples. The log is preserved, not regenerated from the reduced arrays.

N19. *October 8 CERN and manuscript-addition audit*, supplied with this manuscript as an audit script, JSON/CSV results, source manifest and replay checklist in `revision5/`. Reproduces local file/schema checks and exported arithmetic without importing or running the historical ROOT analysis or its synthetic fallback.

N20. Three `CMS_STO_Bounded_Replay_*.npz` replacements, supplied for the 8 October 2026 bounded-replay revision, with the same three ROOT basenames as N16. They contain 1,849,461 flat AK5 four-vector rows, offsets, 40,193 source-entry indices and JSON provenance declaring the unmodified shard selection. Original ROOT hashes remain declared; NPZ hashes are independently recorded.

N21. *Bounded CERN replay audit*, `revision6/audit_bounded_replay.py` and its JSON/CSV outputs in the reproduction package. Recounts the available AK5 pT, phi and joint rows; compares corrected energy and eta with historical energy-labelled results; records source-entry support and schema checks. Uses NumPy without pickle loading, ROOT execution or synthetic fallback. `CERN_REPLAY_CHECKLIST.md` distinguishes completed repairs from the remaining source and statistical work.

N22. `sto_reconciliation_briefing.md`, author-supplied reconciliation briefing. HTF acoustic and spectral assignments, annular stress fields, optical-readout proposals and the $4\pi^2/\ln 2$ entropy-count factor. Preserved unchanged in `revision7/sources/` with its hash.

N23. `Working proof_261013_190218(1).txt`, author-supplied working proof. Acoustic notes, octave assignments, spectral Anglar table and supporting derivations. Preserved unchanged in `revision7/sources/` with its hash. Later author clarification N24 governs the superseded inch interpretation.

N24. Christopher Schiele, HTF manuscript-reconciliation instruction, supplied before this revision. Replaces the inch references with ordinary wavenumber $1/\lambda$, where λ is the derived fundamental m-point wavelength near 0.002543 m, and requests inclusion of the aspects relevant to EFE–QFT reconciliation. The instruction is archived in `revision7/sources/author_HTF_clarification.txt`.

N25. *HTF and MFAT coordinate audit*, `revision7/audit_htf_mfat.py`, numerical outputs and revision notes. Recomputes the temperature–wavelength closure, entropy-count ratio, acoustic and spectral conversions, stress equilibrium and the proposed compatibility completion. No new physical experiment or detector-data replay is represented by this audit.

N26. Christopher Schiele, Appendix A3 correction, 20 October 2026 local review date. Specifies $T_g = 66.588452$ and $\lambda = \lambda_k / T_g$, with $\lambda_k = c\,h/\left(k_B \ln 2\right)$, and states that the previously imported matching temperature is not the STO profile temperature. Original clarification archived in `revision7/sources/author_A3_clarification.txt`.

N27. Christopher Schiele, *28 STO5 - The Time Manifold.docx*, Chapter 62 and Appendices 62.A–C, supplied 23 October 2026. Closure, routing, finite allocation and Laplacian proposals, reconciled in Appendix L. Original DOCX and extraction are preserved in revision8. N24 governs superseded inch references.

N28. `cms_sto_analysis11.py` and `cern_data_packager.py`, supplied 23 October 2026 with the three bounded exports and result archives. Originals and hashes are retained in revision8; E4 records the extraction and legacy-analysis findings.

N29. *Time Manifold and CERN provenance reconciliation audit*, revision8. Source manifests, finite mathematical witnesses, bounded CERN recount, public-index metadata and manuscript changes. The graph is illustrative; no new whole-stack certificate, experiment or discovery significance is asserted.

N30. Christopher Schiele, author clarification supplied 26 October 2026: LT rotation-period carrier; HTF divisor deconstruction; information partition $\ln 2/3$; clock charts; continuous space, discrete geometric time, ubiquitous curvature and global energy conservation. Preserved as the revision specification in `revision9/`.

N31. Fresh AxiomARC source execution and reconciliation audit, 26 October 2026. Source archive, hashes, original pytest log and single-test dependency retry, numerical JSON, and reproducible `audit_current.py` are retained in `revision9/`. The production AME artifact hash is `033faa29331a2a6a72eba42760faf381cf36afbbd17e1ee565497ff2a71ed062`.